Numerical and experimental methods for viscoelastic circular contacts in dry and lubricated conditions

Politecnico di Bari

Department of Mechanics, Mathematics and Management

Mechanical and Management Engineering
Ph.D. Program

SSD: ING-IND/13 - Applied Mechanics

Final dissertation

Numerical and Experimental Methods for Viscoelastic Circular Contacts in Dry and Lubricated Conditions

by
Michele Santeramo

Supervisors:
Prof. Giuseppe Carbone
Prof. Carmine Putignano
Prof. Leonardo Soria

Coordinator of the Ph.D. Program:
Prof. Giuseppe P. Demelio

Course XXXVI, 01/11/2020 - 01/11/2023

Sommario

La presente tesi ha come obiettivo lo sviluppo di una metodologia Boundary Element per studiare problemi di contatto circolare 2D in condizioni steady-state. In particolare, l'approccio si basa sulla definizione di un'appropriata funzione di Green viscoelastica steady-state, che tenga conto della natura del dominio di contatto circolare, tipica, per esempio, di una coppia rotoidale. In particolar modo, la presente formulazione permette di studiare problemi viscoelastici in cui il materiale sia caratterizzato da uno spettro continuo di tempi di rilassamento. Il problema del contatto può essere facilmente formulato sotto forma di prodotto di convoluzione spaziale tra gli stress e gli spostamenti, aprendo alla risoluzione di svariati problemi di contatto in ambito ingegneristico; questi possono essere caratterizzati da contatti multipli, come ad esempio si riscontra nei cuscinetti viscoelastici a rulli. Peraltro, per formulare correttamente il problema, la definizione del tensore di Green spaziale è fondamentale. In particolare, i componenti di tale tensore, ossia gli spostamenti radiali e tangenziali associati a forze unitarie concentrate radiali e tangenziali, sono determinati con il metodo dei potenziali complessi. A differenza dell'approccio usuale che impiega la funzione di stress di Airy, il metodo dei potenziali complessi consente, attraverso la definizione di opportuni potenziali complessi, di definire un *modus operandi* che non richieda la risoluzione di nuove equazioni differenziali ad ogni cambiamento del sistema di riferimento.

Una volta derivata la funzione di Green viscoelastica, si studia il problema del contatto conforme di un perno rigido a contatto con uno spazio deformabile avente un foro cilindrico. In un primo momento, la metodologia è stata validata con la soluzione analitica di A. Persson per un caso puramente elastico; in seguito, è stato analizzato il caso di uno spazio viscoelastico lineare: come ci si aspetta in un problema di contatto viscoelastico, in corrispondenza del leading edge, la distribuzione di pressione mostra un picco, mentre maggiori deformazioni si riscontrano in corrispondenza del trailing edge, a causa del diverso rilassamento nelle due regioni. Infatti, in corrispondenza del trailing edge, il materiale è stato appena deformato e si sta rilassando. Inoltre, questo processo dipende dalla velocità, poiché il materiale, quando sollecitato a velocità molto basse e molto alte, ossia quando si trova rispettivamente nelle zone rubbery e glassy, si comporta come un solido elastico e la dissipazione di energia è trascurabile. Quest'ultima è importante a velocità intermedie, a causa del comportamento isteretico del materiale.

In più, grazie alla ben nota efficienza computazionale dei metodi Boundary Element, la presente metodologia viene impiegata come alternativa valida e numericamente più efficiente agli approcci agli elementi finiti per analizzare il problema del contatto multiplo in un cuscinetto a corpi volventi, in cui le piste di rotolamento sono viscoelastiche lineari e gli elementi volventi sono assunti come rigidi. Da un punto di vista applicativo, la valutazione del problema del contatto è fondamentale. Infatti, si dimostra che la distribuzione del carico tra i corpi volventi si discosta significativamente rispetto al

caso puramente elastico, con alcuni rulli che non partecipano più al contatto con le piste per determinati range di velocità. Ciò ha conseguenze non solo sulla durata dei corpi volventi, ma può avere un impatto sulla dinamica del rotore del sistema supportato dal cuscinetto. Infine, per corroborare il modello, le previsioni numeriche per un cuscinetto a rullini con anello esterno in Politetrafluoroetilene (PTFE) sono confrontate, con un buon accordo, con i risultati sperimentali. Ciò è ulteriormente supportato da un successivo confronto tra dati numerici e sperimentali, nel caso in cui l'anello esterno del cuscinetto è realizzato in Poliammide 6 (PA6).

È importante osservare che le possibili implicazioni della metodologia Boundary Element non si limitano alla meccanica del contatto secco, ma la formulazione integrale risulta essere molto utile nei problemi di lubrificazione che coinvolgono superfici conformi. In modo particolare, si considera il caso di un cuscinetto portante polimerico e viene evidenziato quanto sia importante definire un'appropriata funzione di Green che tenga conto della conformità del problema. Infatti, utilizzando la classica funzione di Green per il caso half-plane si osservano deviazioni significative: questo aspetto è cruciale durante le fasi progettuali del sistema.

Dunque, si evidenzia come la complessa reologia del materiale viscoelastico sia fortemente accoppiata alle perdite viscose del lubrificante, influenzando così la capacità di carico del sistema. In particolare, le distribuzioni di pressione e di spessore del film sono determinate per diverse configurazioni di contatto, sottolineando come la lubrificazione viscoelastica sia governata da tre parametri, ossia il numero di Hersey e le velocità adimensionali dei tribopartner.

Abstract

The present thesis is focused on the development of a Boundary Element formulation to assess two-dimensional steady-state circular contact problems. In particular, the methodology paves over an *ad-hoc* defined steady-state viscoelastic Green's function, which takes into account the circular hallmark of the contact domain, typical, for example, of a mechanical pin joint. Crucially, it is able to manage any real viscoelastic material, characterized by a continuum spectrum of relaxation times. The contact problem can be easily formulated in the form of a spatial convolution product between surface stresses and displacement, which blazes the trail to solving contact problems of a countless number of engineering-relevant systems, where multiple contacts occur, such as viscoelastic rolling element bearing. Incidentally, to correctly formulate the contact problem, the definition of the spatial Green's tensor is crucial. Specifically, the entries of such tensor, namely the radial and tangential displacements associated to concentrated radial and tangential unit forces, are determined via a complex variable method. Conversely to the usual method employing the Airy's stress function, the complex variable method allows, through the definition of appropriate complex potentials, a *modus operandi* which does not entail the solution to fresh differential equations whenever the coordinates are changed.

Once the viscoelastic Green's function is derived, the conformal contact problem of a rigid pin in contact with a deformable space with a cylindrical hole is investigated. At first, the methodology is validated against the analytical solution provided by A. Persson for a purely elastic case; then, the case of a linearly viscoelastic space is analyzed: as expected in a viscoelastic contact system, at the leading edge, the pressure distribution peaks, whilst the displacements are larger at the trailing edge, due to the different relaxation in the two regions. Indeed, at the trailing edge, the material has been just deformed and is still relaxing. Moreover, this process is speed-dependent as, at very low and very high speeds the material enters the rubbery and glassy regions respectively, where it behaves as a solid elastic body, and the energy dissipation is negligible. The latter is significant at intermediate speed, where proper viscoelasticity effects arise.

Notably, thanks to the well-known computational efficiency of Boundary Element methods, the present methodology is employed as a valid and numerical more efficient alternative to Finite Element approaches to assess the multiple contact problem in a rolling element bearing, where the raceways are linearly viscoelastic, and the rolling elements are assumed to be rigid. From an applicative point of view, the assessment of the contact problem is crucial. In fact, it is shown that the distribution of the load among the rolling elements deviates significantly with respect to the purely elastic case, with some rollers eventually losing the contact with the raceways for some speed values. This has consequences not only on the rolling element durability but may impact the rotor dynamics of the system supported by the bearing. Finally, to corroborate the

model, numerical predictions for a rolling element bearing with the outer ring made of Polytetrafluoroethylene (PTFE) are compared, with good agreement, to experimental outcomes. This is further supported by a successive comparison between numerics and experiments, for the outer ring of the bearing is made of Polyamide 6 (PA6).

Crucially, it should be observed that possible implications of the Boundary Element methodology are not limited to dry contact mechanics, but the integral formulation could be very useful in lubrication problems involving conformal surfaces. Specifically, the case of a polymer journal bearing is studied and the importance of the definition of an appropriate Green's function to take into account of the conformity of the problem is highlighted. In fact, making use of the classical half-plane Green's function significant deviations are observed in the case of such conforming contact conditions: this aspect is then critical in design processes.

Furthermore, it is overt that the complex rheology of the viscoelastic material is strongly coupled with the lubricant viscous losses, thus affecting the bearing capacity of the system. Hence, the pressure and film thickness distributions for different contact configurations are determined, highlighting that viscoelastic lubrication is governed by three parameters, i.e., the Hersey number and the dimensionless velocities of the interacting pair.

Contents

List of Figures

Introduction

In the last two decades, an increasing number of researchers have been dedicating considerable efforts to improve our comprehension of the mechanical and tribological behavior of hard- and soft-viscoelastic materials. Indeed, viscoelasticity is a fascinating object of study, as it is marked by the well-known theoretical complexity originated by the complex rheology of such materials. At the same time, this interest is not purely speculative. Viscoelastic systems are ubiquitous in nature: biological tissues are a simple and immediate example of soft viscoelastic materials. At different scales, ranging from cellular structures [1, 2] to complex systems, like human skin [3, 4] or cartilage [5], these tissues are, in fact, from a biomechanical point of view, hyperelastic and exhibit a time-dependent stress-strain constitutive behavior. On the other hand, in industry, several reasons, related to reduced costs, lighter weights, more flexible structures, are inducing a change in mechanical design and, specifically, a continuous shift from hard metals to polymers. Thus, in addition to components traditionally made of rubber-based composites, like belts [6], rollers, and tires, numerous more systems are now redesigned with polymer plastics: a particularly significant case of study is related to polymer journal and rolling element bearings, which are increasingly employed in mechanical systems [7].

Consequently, theoretical and applicative interest has triggered enormous attention to the field. A crucial aspect in this research trend deals, in particular, with the viscoelastic rheology that characterizes polymeric materials: viscoelasticity is associated with time-dependent stresses and strains, and, most crucially, leads to hysteresis and energy dissipation. Hysteretic losses need to be carefully considered, especially in contact mechanics problems, as they add up to the interfacial friction contribution, giving place to the so-called viscoelastic friction. Hence, the countless number of papers focused on viscoelastic contact mechanics. These date back to the 1960s from the pioneering analytical study proposed by Hunter [8] for a cylinder in contact with a viscoelastic slab and the following experimental campaign carried out by Grosch [9]. Later, twenty years ago, another analytical ground-breaking contribution has been proposed by B.N.J. Persson in Ref. [10]: the contact mechanics theory has proposed, *inter alia*, an approach to account for the contribution given by the roughness to viscoelastic dissipation. Furthermore, in the last decades, numerical methodologies have been developed to tackle the viscoelastic contact problems [11–16]: most of these are Boundary Element (BE) formulations, where just the boundary domain is discretized [17–21]. This entails high computational efficiency and has allowed to carry out very detailed numerical investigations in the field: these studies have assessed steady-state [22] and reciprocating [23] contact mechanics in smooth and rough conditions [24–27], normal indentation, and even lubrication problems, where the so-called visco-elastohydrodynamic regime has been found [23, 28, 29].

Despite these significant advancements in dry and lubricated viscoelastic contact mechanics, however, the attention has been so far limited to non-conformal geometries:

this means that contacting surfaces do not conform to each other, because of the very different curvature of the contacting bodies. The classical two-dimensional example is a cylinder in contact with a half-plane. This contact configuration is doubtlessly important, but it is not universal, as conformal contacts are quite common in applications: for example, the pin joint is a clear conformal contact condition. Interestingly, such a conformal configuration has implications also in the case of multiple contacts, e.g., rolling element bearings: indeed, although each roller may be considered in a non-conformal contact with the rings, the presence of multiple rolling elements indenting the ring introduces interaction effects related to the finiteness of the radii of the rings and the circular geometry of the system, thus leading to a sort of conformal-like effect. Furthermore, conformal problems are common in biomechanics: the hip joint [30] and all the prostheses [31] are possible examples. For artificial hip joints, the effect of surface roughness on the real area of contact has been studied numerically using a combined finite element and boundary element approach [32, 33]. Consequently, the theme of conformal contact mechanics cannot be ignored. A pioneering contribution has been proposed by A. Persson in his Ph.D. thesis [34], where, for purely elastic solids, highly conformal geometries have been investigated. This approach has been further developed in Ref. [35, 36], where the authors considered elastically similar and dissimilar contacting bodies. Other contributions to the field can be found in Ref. [37, 38], where frictional interfaces have been taken into account, and in Ref. [39, 40], where the authors proposed a FFT-based conformal linear elastic contact model for 2D problems with two concentric cylindrical interfaces. However, no solution is available in the case of viscoelastic rheology for the contacting bodies. In this case, the problem could be tackled by employing Finite Element Methods (FEM) [11–13, 41], but this would lead to high computational costs, which would be, in practice, unfeasible when multiple scales are accounted for the analysis. This work aims at filling this gap about viscoelastic circular contact mechanics, for both conformal and non-conformal geometries, by introducing an *ad hoc* developed BE methodology.

The thesis is outlined as follows. Chapter 1 presents a brief introduction to linear viscoelasticity, providing the reader with the fundamental knowledge this work paves over. Chapter 2 contains the mathematical formulation, which the numerical approach relies on, for both conforming and non-conforming circular contacts. As highlighted later, the critical point of the present approach is the proper definition of the Green's functions, which intrinsically take into account the circular hallmark of the contact domain. Specifically, the complex potentials theory for plane elasticity problems (see Refs. [42, 43]) is employed to derive the expressions of the spatial Green's functions that properly describe the contact problems encountered in this thesis. Furthermore, the isothermal steady-state viscoelastic Green's function will be, for the first time, presented for circular contact problems. Then, the Boundary Element (BE) methodology will be validated, for the elastic conformal contact, with the analytical solution presented by A.Persson [34]. The analysis is then extended to the viscoelasticity case, and a wide breadth is given in the assessment of the viscoelastic contribution to friction. The strength of the present methodology is shown in the assessment of the load distribution and the hysteretic losses for a polymer rolling element bearing, with linearly viscoelastic raceways and rigid rolling elements, showing the significant role of viscoelasticity in the steady-state operation of the bearing: in fact, it will be shown that, for the case of a single relaxation time material, some of the rolling elements in the load zone, for a certain range of velocities, do not transmit the contact. This, as extensively explained later, is related to the memory effect typical of polymeric material.

Crucially, the methodology has been corroborated experimentally, where a rolling element bearing with the outer ring made of Polytetrafluoroethylene (PTFE) and, later, Polyamide 6 (PA6) has been tested at different loading and temperature conditions. The agreement between the numerical predictions and the experimental outcomes is good, confirming the goodness of the approach. Finally, in Chapter 3, a BE approach is introduced to assess the steady-state operations of a polymer journal bearing, where it will be shown how viscoelasticity clearly affects the system response. In particular, three different configurations will be investigated: hard-on-soft (HS), where the journal is rigid and the bearing is linearly viscoelastic, soft-on-hard (SH), where the journal is linearly viscoelastic and the bearing is rigid, and soft-on-soft (SS), where both the interacting pairs are linearly viscoelastic. Hence, Appendix A briefly recalls the complex potentials theory and the expressions of the spatial Green's functions that will be employed to assess the contact problems analyzed.

Chapter 1

Introduction to linear viscoelasticity theory

As mentioned in the Indroduction, the comprehension of the mechanical and tribological behavior of soft materials is attracting interdisciplinary efforts from researchers worldwide: as a matter of fact, soft systems are ubiquitous in nature [1–5], and their ever-encroaching role in industry is overt. Indeed, a continuously increasing shift from hard metals to polymers is observed: for example, polymeric materials are now commonly employed as power transmission components because of their advantageous features in terms of lighter weights, resistance to environmental conditions, and reduced costs in manufacturing. Among these components, made of polymers and polymer composites, let us recall gears [44], belts [6], bearings [45], and tires [13,46]. In addition, a major role in industry has being currently played by high-temperature polymer coatings [47]: in industrial, automotive, pharmaceutical, and electronics parts, they are widely employed to ensure anti-wear performance and durability of the coated parts. On the other hand, the use of polymer coatings is not restricted to high-temperature applications, but, on the contrary, has an interesting perspective also at very low temperatures, where self-lubricating polymers can provide crucial results [48, 49]. Therefore, a comprehensive understanding of viscoelasticity is needed. A fundamental contribution has been supplied by Hunter [8], Grosch [9], B.N.J. Persson [10, 14] and Christensen [50, 51], who furnished a consistent and wide-breadth description of the linear theory of the viscoelastic behavior of materials. In particular, the need for such a theory is driven by the fact that polymer materials exhibit mechanical responses, which are out of reach of the theories of elasticity and viscosity, as they have a capacity to both store and dissipate energy. It is well-known that the former theory does not take into account energy dissipation, whereas a Newtonian viscous fluid does not imply a capacity to store energy. Interestingly, studying the response of a viscoelastic material to a suddenly applied uniform distribution of surface tractions, it can be seen that it undergoes an instantaneous deformation followed by a flow process that may not be limited in magnitude as time grows, therefore exhibiting both an instantaneous effect and creep hallmarks. Thus, viscoelastic materials are marked by time-dependent behavior, and, crucially, their mechanical response is not only determined by the current state of stress but also by the complete stress history: this characteristic is known as *memory effect*.

Hence, we can now introduce the isothermal viscoelastic constitutive relationships. Consider the undeformed configuration of a general deformable solid and a fixed reference

frame attached to it. Then, with respect to this configuration, we can specify the displacement vector as $\mathbf{u}(t') = \mathbf{x}(t') - \mathbf{X}$, with $\mathbf{x}$ and $\mathbf{X}$ denoting the coordinates of the undeformed and deformed configuration respectively, t' is the time variable, $-\infty < t' < t$, where t specifies the current time. Thus, the theory of viscoelasticity is referred to as infinitesimal if the displacements are small with respect to the characteristic dimension of the body and if the deformation is infinitesimal, i.e. $\epsilon = \sup_{t'} |\partial u_i(t')/\partial X_j| \ll 1$ at all times t' [51]. The indices i and j follow the usual Cartesian tensor notation. Furthermore, it is important to recall that the term *deformation*, when applied to a continuous body, refers to changes in the relative distances of the points of this body. This definition clearly distinguishes *pure* deformation and rigid-body motion, the latter being characterized by no variations in the mutual distances of the points of the continuum body. Under these conditions, we can introduce the strain tensor $\varepsilon_{ij} = (\partial u_i(t')/\partial x_j + \partial u_j(t')/\partial x_i)/2$, where the differentiation is carried out with respect to the deformed configuration, since in the infinitesimal theory it is immaterial to discern between undeformed and deformed configuration coordinates.

A proper definition of stress is of tantamount importance. In particular, the force acting on the infinitely small surface element dS has the form $\mathbf{F} = \boldsymbol{\sigma} dS$, where $\boldsymbol{\sigma}$ is the traction per unit area or the stress vector. The traction represents the force acting between the parts of the continuous body adjacent to either side of the surface element dS. To distinguish between these two elements of the body, the unit vector $\mathbf{n}$, normal to the area dS, is defined: the traction $\mathbf{F}$, acting on the area in question, is understood as the force which the part lying on the positive side of a surface element exerts on the part lying on the negative side [43], e.g., when detaching a finite volume V from the body, the positive direction of the normal unit vector is chosen as the one that it is outward with regards to V. It is evident that the stress vector depends on the spatial coordinate of the general surface element considered, and, crucially, on its orientation, i.e. on the direction of the normal unit vector $\mathbf{n}$. Clearly, in dynamics, stress is also a function of time. As well established [43, 52, 53], the application of the balance of linear momentum to a small tetrahedron leads to the definition of the stress tensor σ_{ij}: it is a second-order tensor defined through the transformation which relates the components of the stress vector to the orientation of the surface element, namely $\sigma_i = \sigma_{ij} n_j$. Furthermore, under the assumption that the angular momentum of a small-volume element is balanced, the stress tensor σ_{ij} is shown to be symmetric, i.e. $\sigma_{ij} = \sigma_{ji}$.

Now, the hypothesis that the current value of the stress tensor depends upon the complete past history of the components of the strain tensor is formulated through the following expression [51]:

$$\sigma_{ij}(t) = \overset{\infty}{\underset{s=0}{\psi_{ij}}}(\varepsilon_{kl}(t-\tau), \varepsilon_{kl}(t)) \tag{1.1}$$

where ψ_{ij} is a linear tensor valued functional which transforms each strain history $\varepsilon_{ij}(t)$ into a corresponding stress history $\sigma_{ij}(t)$, with $-\infty < t < \infty$. Notice the dependence of the linear functional ψ_{ij} upon the instantaneous elasticity response of the material, that is $\varepsilon_{kl}(t)$.

Under the assumption that the strain history is continuous and the functional is linear, by making use of the Riesz representation theorem [1] we can rephrase Equation

[1] Every linear functional can be written as a Stieltjes integral of the form $\int_a^b f(x) d\alpha(x)$, where $f(x)$ is a continuous function, and $\alpha(x)$ is a fixed function of bounded variation in the closed interval [a,b].

(1.1) as a Stieltjes integral:

$$\sigma_{ij}(t) = \int_0^\infty \varepsilon_{kl}(t-\tau) dG_{ijkl}(\tau)\,, \tag{1.2}$$

in which G is a fourth-order tensor such that $G_{ijkl}(t) = 0$ for $-\infty < t < 0$ and each component is of bounded variation in every closed subinterval of $-\infty < t < \infty$ [51, 54]. Moreover, because of the symmetry of stress and strain tensors, we have $G_{ijkl}(t) = G_{jikl}(t) = G_{ijlk}(t)$. Equation (1.2) also highlights that the constitutive relation is unaffected by any shift in the time scale, i.e. we have time translation invariance. Furthermore, taking $\varepsilon_{kl}(t) = 0$ for $t < 0$ together with the assumption that G_{ijkl} and its first derivative are continuous on the interval $0 \leq t < \infty$, Equation (1.2) can be written as:

$$\sigma_{ij}(t) = G_{ijkl}(0)\varepsilon_{kl}(t) + \int_0^t d\tau\ \varepsilon_{kl}(t-\tau)\frac{dG_{ijkl}(\tau)}{d\tau}, \tag{1.3}$$

and, making use of the change of variable rule $\lambda = t - \tau$ the following is obtained:

$$\sigma_{ij}(t) = \int_0^t d\lambda\ G_{ijkl}(t-\lambda)\frac{d\varepsilon_{kl}(\lambda)}{d\lambda}. \tag{1.4}$$

Now, the constitutive relation derived can be considered the formulation of Boltzmann's superposition principle: the current state is determined by the superposition of the responses to the complete spectrum of increments of strain. The integrating functions $G_{ijkl}(t)$ are known as relaxation functions and are mechanical properties of the material. If the roles of stress and strain are reversed, it is possible to retrieve a complementary relation:

$$\varepsilon_{ij}(t) = \int_0^t d\lambda\ J_{ijkl}(t-\lambda)\frac{d\sigma_{kl}(\lambda)}{d\lambda}, \tag{1.5}$$

in which $J_{ijkl}(t)$ are the so-called creep functions, obeying the causality principle, that is $J_{ijkl}(t) = 0$ for $t < 0$, and $J_{ijkl}(t) = J_{jikl}(t) = J_{ijlk}(t)$.

To exploit the relationship between creep and relaxation functions, by making use of the Laplace transformation of Equations (1.4) and (1.5), it can be seen that $\bar{G}(s)\bar{J}(s) = 1/s^2$, with $\bar{G}(s)$ and $\bar{J}(s)$ being the Laplace transform of the generic relaxation function $G(t)$, and the generic creep function $J(t)$ [55]. By taking the inverse transform, and using the convolution theorem, it is possible to retrieve

$$\int_0^t d\tau\ J(t-\tau)G(\tau) = \int_0^t d\tau\ G(t-\tau)J(\tau) = t, \tag{1.6}$$

or, alternatively

$$J(0)G(t) + \int_0^t d\tau\ G(t-\tau)\frac{dJ(\tau)}{d\tau} = 1. \tag{1.7}$$

It is interesting now to determine any restrictions which may be imposed upon the constitutive relations for a particular type of memory effect, known as *fading memory*, which has been extensively examined in the studies of Volterra [56] and Coleman [57,58]. A simple definition of such an effect is the following [51]: the current value of a field variable, that has a linear functional type dependence upon the complete past history of a second field variable, depends more strongly upon the recent history than upon the distant history of the second variable. Therefore, this dependence is determined through

a weighting function assigning a continuously decreasing dependence as the past events are continuously more distant from the current time. Looking at Equation (1.3), it is evident that the slopes of the relaxation functions *weight* the dependence of the current stress upon the past history of strain. Thus, it is sufficient that the magnitudes of the slopes of the relaxation functions continuously decrease with time, that is:

$$\left|\frac{dG(t)}{dt}\right|_{t=t_1} \leq \left|\frac{dG(t)}{dt}\right|_{t=t_2} \tag{1.8}$$

for $t_1 > t_2 > 0$. Clearly, the fading memory hypothesis is satisfied by the restrictions on the creep functions:

$$\left|\frac{dJ(t)}{dt}\right|_{t=t_1} \leq \left|\frac{dJ(t)}{dt}\right|_{t=t_2} \tag{1.9}$$

for $t_1 > t_2 > 0$.

1.1 Steady-state constitutive relations

Let us consider a viscoelastic body subjected to steady-state harmonic oscillation conditions. In particular, let us examine the case in which the strain history is specified as $\varepsilon(t) = \varepsilon_0 \exp(i\omega t)$, with ε_0 being the amplitude and ω the frequency of oscillation. As presented in Ref. [51], the relaxation function $G(t)$ can be decomposed into two parts, that is $G(t) = \tilde{G} + \hat{G}(t)$, the latter vanishing as $t \to \infty$. Thus, making use of Equation (1.4), the following expression for the stress is obtained:

$$\sigma(t) = \tilde{G}\varepsilon_0 \exp(i\omega t) + i\omega\varepsilon_0 \int_{-\infty}^{t} d\tau\, \hat{G}(t-\tau) \exp(i\omega\tau), \tag{1.10}$$

that, with the change of variable $\xi = t - \tau$ becomes

$$\sigma(t) = \left[\tilde{G} + \omega \int_0^{\infty} d\xi\, \hat{G}(\xi) \sin(\omega\xi) + i\omega \int_0^{\infty} d\xi\, \hat{G}(\xi) \cos(\omega\xi)\right] \varepsilon_0 \exp(i\omega t). \tag{1.11}$$

Coherently with the definition of the steady state conditions for the strain history, the stress can be cast as $\sigma(t) = G^*(\omega)\varepsilon_0 \exp(i\omega t)$, where

$$G^*(\omega) = \tilde{G} + \omega \int_0^{\infty} d\xi\, \hat{G}(\xi) \sin(\omega\xi) + i\omega \int_0^{\infty} d\xi\, \hat{G}(\xi) \cos(\omega\xi) \tag{1.12}$$

is termed *complex modulus*. Henceforth, it can be decomposed into its real and imaginary parts, such that $G^*(\omega) = G'(\omega) + G''(\omega)$. The former is usually referred to as the *storage modulus* and it is equal to

$$G'(\omega) = \tilde{G} + \omega \int_0^{\infty} d\xi\, \hat{G}(\xi) \sin(\omega\xi), \tag{1.13}$$

while the so-called *loss modulus* $G''(\omega)$ is equal to

$$G''(\omega) = \omega \int_0^{\infty} d\xi\, \hat{G}(\xi) \cos(\omega\xi). \tag{1.14}$$

Interestingly, integration by parts of these helps understand what happens at frequencies approaching zero and infinity. Indeed, at zero frequency, we have $G'(0) = \tilde{G} =$

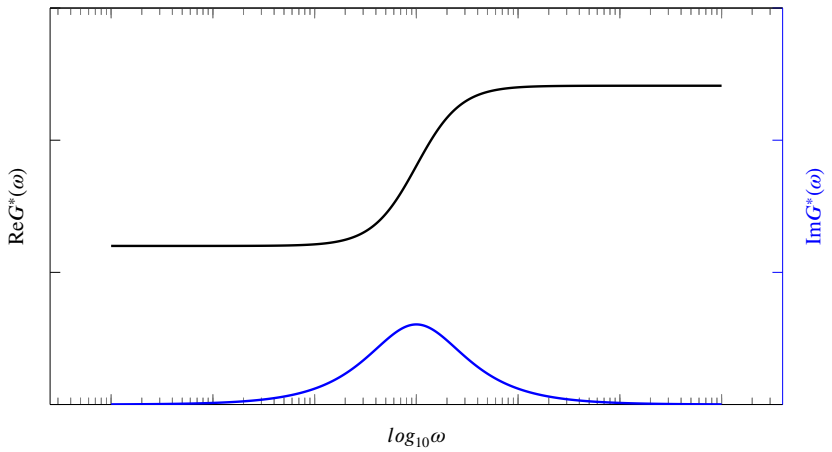

Figure 1.1: The real part of the viscoelastic complex modulus, $G'(\omega) = \mathrm{Re}G^*(\omega)$ (solid black line on the left) and the imaginary part of the viscoelastic complex modulus, $G''(\omega) = \mathrm{Re}G^*(\omega)$ (solid blue line on the right), as function of the frequency ω.

$G(t)|_{t\to\infty}$ and $G''(0) = 0$, while at infinite frequency the real and imaginary moduli are $G'(\infty) = \tilde{G} + \hat{G}(0) = G(t)|_{t\to 0}$ and $G''(\infty) = 0$. Notably, as the frequency of excitation becomes very large, the material behaves as an elastic solid, since the imaginary part of the complex modulus vanishes; at very small frequencies the material behaves either as an elastic solid or as a viscous fluid. Therefore, a viscoelastic fluid behaves elastically for very fast processes and viscously for very slow processes, while a viscoelastic solid behaves elastically when it is subject to very fast or very slow frequencies of excitation. Schematic representations of the storage and loss moduli for a typical viscoelastic material with a single relaxation time are qualitatively depicted in Figure 1.1.

Notably, it is possible to write the stress-strain relation in an alternative form, that is

$$\sigma(t) = |G^*(\omega)|\varepsilon_0 \exp(i\omega t + \delta(\omega)), \tag{1.15}$$

with $\delta(\omega) = \tan^{-1}(G''(\omega)/G'(\omega))$. This representation better highlights the lag between the steady-state harmonic strain and stress.

1.2 Thermoviscoelasticity

Viscoelastic materials, as explained in the previous sections, do not conserve energy, so a proper derivation of a general linear theory of thermoviscoelasticity is necessary. This derivation is based upon the balance of energy and the entropy production inequality, as presented by Christensen and Naghdi [50]. Crucially, since the analyses carried out in this thesis assume isothermal conditions, some of the implications and restrictions in deducing an isothermal theory are examined. Let us consider the load balance of energy for infinitesimal theory, that is:

$$\rho r - \rho(\dot{A} + \dot{T}S + T\dot{S}) + \sigma_{ij}\dot{\varepsilon}_{ij} - Q_{i,i} = 0, \tag{1.16}$$

with ρ being the mass density, r being the heat supply function per unit mass, and provides the means of either adding or removing heat by an external agent. Moreover, A is the Helmholtz free energy per unit mass, S the entropy per unit mass, T is the absolute

temperature, and Q_i are the Cartesian components of the heat flux vector $\mathbf{Q}$ measured per unit area per unit time. Furthermore, the local entropy production inequality, often referred to as the Clausius-Duhem inequality, is given by:

$$\rho\dot{T}S - \rho r + Q_{i,i} - Q_i(T_{,i}/T) \geq 0, \tag{1.17}$$

It is evident that the free energy is a functional of both strain and temperature history, and cannot be considered to be a linear functional. Making use of the Stone-Weierstrass approximation theorem, under the assumption that $\varepsilon_{ij}(t)$ and $T(t)$ are continuous on the interval $-\infty < t < \infty$, and $\varepsilon_{ij}(t) \to 0$ and $T(t) \to T_0$ as $t \to -\infty$, the real continuous scalar-valued functional of $\varepsilon_{ij}(t)$ and $T(t)$ may be uniformly approximated by a polynomial in a set of real, continuous, linear functionals of $\varepsilon_{ij}(t)$ and $T(t)$. Then, the Riesz representation theorem can be employed, and these linear functionals are expressed in terms of Stieltjes integrals in which the integrating functions are of bounded variation. The complete formulation can be found in Ref. [51]. In particular, the authors obtain the following inequality:

$$\Lambda - Q_i(\theta_{,i}/T_0) \geq 0, \tag{1.18}$$

where $\theta(t) = T(t) - T_0$, with T_0 being the base temperature, and Λ represents the rate of dissipation of energy and is given by

$$\begin{aligned}\Lambda = &-\frac{1}{2}\int_{-\infty}^{t}\int_{-\infty}^{t} d\tau d\eta \ \frac{\partial}{\partial t}G_{ijkl}(t-\tau,t-\eta)\frac{\partial\varepsilon_{ij}(\tau)}{\partial\tau}\frac{\partial\varepsilon_{kl}(\eta)}{\partial\eta}+\\ &+\int_{-\infty}^{t}\int_{-\infty}^{t} d\tau d\eta \ \frac{\partial}{\partial t}\varphi_{ij}(t-\tau,t-\eta)\frac{\partial\varepsilon_{ij}(\tau)}{\partial\tau}\frac{\partial\theta(\eta)}{\partial\eta}+\\ &+\frac{1}{2}\int_{-\infty}^{t}\int_{-\infty}^{t} d\tau d\eta \ \frac{\partial}{\partial t}m(t-\tau,t-\eta)\frac{\partial\theta(\tau)}{\partial\tau}\frac{\partial\theta(\eta)}{\partial\eta}.\end{aligned} \tag{1.19}$$

We recall that the mechanical properties, i.e. the integrating functions $G_{ijkl}(t,t')$, $\varphi_{ij}(t,t')$, and $m(t,t')$ obey causality: they vanish as $t < 0$, $t' < 0$, while they are assumed to be continuous for positive arguments.

Then, considering a particular process such that $\theta_{,i} = 0$, i.e. uniform temperature field, Equation (1.17) becomes $\Lambda \geq 0$, which is also known as *dissipation inequality*, where Λ now is rephrased as:

$$\Lambda = -\frac{1}{2}\int_{-\infty}^{t}\int_{-\infty}^{t} d\tau d\eta \ \frac{\partial}{\partial t}G_{ijkl}(t-\tau,t-\eta)\frac{\partial\varepsilon_{ij}(\tau)}{\partial\tau}\frac{\partial\varepsilon_{kl}(\eta)}{\partial\eta}, \tag{1.20}$$

which expresses the thermodynamical restriction that the rate of dissipation of energy must be non-negative. Furthermore, non-negative work requirement is common in continuum mechanics: in linear isothermal viscoelasticity, Gurtin and Herrera [59] have made use of the requirement that the work done to deform the material from the virgin state must fulfill the nonnegative work relation $\int_0^t d\tau \ \sigma_{ij}(\tau)\partial\varepsilon_{ij}(\tau)/\partial\tau \geq 0$. Hence, making use of Equation (1.16) and Equation (1.17), under isothermal conditions, we find:

$$-\rho\dot{A} + \sigma_{ij}\dot{\varepsilon}_{ij} \geq 0. \tag{1.21}$$

Now, performing integration of (1.21), we can write:

$$-\rho A + \int_0^t d\tau \ \sigma_{ij}(\tau)\frac{\partial\varepsilon_{ij}(\tau)}{\partial\tau} \geq 0, \tag{1.22}$$

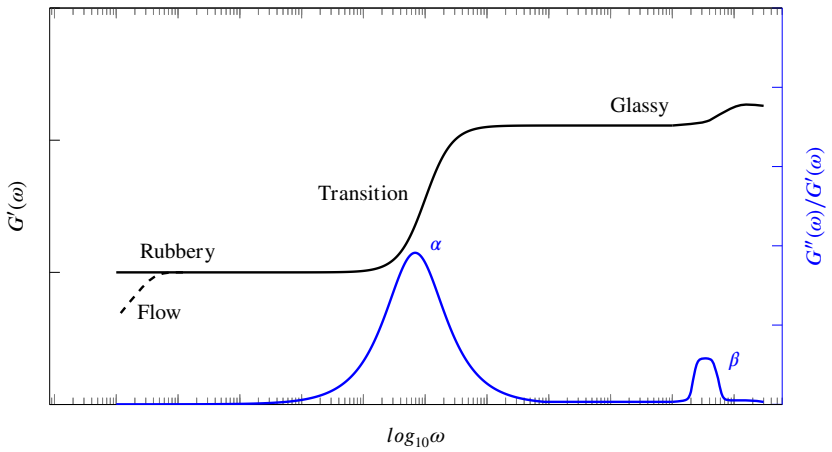

Figure 1.2: General form of viscoelastic behavior of polymer: on the left, the real part of the viscoelastic complex modulus, $G'(\omega) = \mathrm{Re}G^*(\omega)$ and, on the right, the loss tangent $\tan\delta = G''(\omega)/G'(\omega)$ as function of the frequency ω.

Recognizing that the left-hand side of (1.21) corresponds to the rate of dissipation of energy Λ, we have that the non-negative work requirement can be expressed as:

$$\int_0^t d\tau\ \Lambda(\tau)\ \geq 0. \tag{1.23}$$

with the Helmholtz free energy per unit mass, that is the stored energy, A being equal to

$$A = \frac{1}{2}\int_{-\infty}^{t}\int_{-\infty}^{t} d\tau d\eta\ G_{ijkl}(t-\tau, t-\eta)\frac{\partial\varepsilon_{ij}(\tau)}{\partial\tau}\frac{\partial\varepsilon_{kl}(\eta)}{\partial\eta}. \tag{1.24}$$

Some considerations about (1.22) and (1.23) are then needed: accepting the thermodynamical requirement $\Lambda \geq 0$, from (1.22) we observe that $\rho A \geq 0$ implies non-negative work; on the contrary, non-negative work does not imply $\rho A \geq 0$. Therefore, requiring $\rho A \geq 0$ is a stronger and physically meaningful condition than requiring non-negative work. Thus, investigating the effects of discontinuous strain, $\varepsilon_{ij}(t) = \bar{\varepsilon}_{ij}\mathcal{H}(t)$, with $\mathcal{H}(t)$ being the Heaviside step function, the requirement of non-negative stored energy, that is, then, $\rho A \geq 0$, leads to $G_{ijkl}(t, t') \geq 0$, while Equation (1.20) requires that the slope of the relaxation function must be negative, and the fading memory hypothesis also requires that the second derivative, with respect to time, of the relaxation function is non-negative, that is the relaxation function is concave up [50, 55].

Now, we can focus on the very strong dependence upon the temperature that the mechanical properties, appropriate to the linear theory of viscoelasticity, generally exhibit. Specifically, the thermoviscoelasticity theory permits mechanical properties to be dependent on a fixed base temperature T_0, but any dependency on infinitesimal temperature deviations from T_0 is necessarily ignored. To include a temperature dependence effect based upon a continuously changing total temperature, some modifications have to be made.

Before proceeding, proper terminology has to be introduced. For example, let us take as representative the complex modulus $G^*(\omega)$ (see Figure 1.2). Notably, the high-frequency or short-time range is referred to as the glassy region, while the low-frequency or long-time region is referred to as the rubbery region. Furthermore, the region where

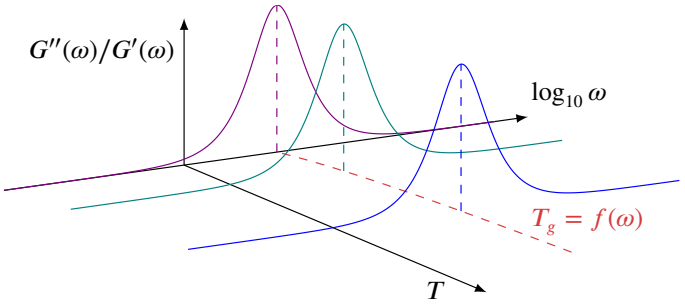

Figure 1.3: Temperature dependence of $G''(\omega)/G'(\omega)$ (inspired by [51])

the greatest dependence upon temperature is observed, i.e. the region where the curves exhibit the maximum magnitude of slope, is the so-called transition region. The corresponding temperature range is designated as the glass transition temperature T_g, which necessarily depends upon the frequency of measurement of the complex modulus, as shown in Figure 1.3. In this region, viscoelastic properties are dominated by the rearrangement of molecular segments, which are sufficiently short that entanglements of molecules or cross-links between them play a relatively minor role. Molecules with side chains tend to exhibit the transition at a progressively higher frequency for constant temperature, as the side chain length increases. Moreover, the transition region is characterized by a very large peak of the loss tangent, known as the α peak, as shown in Figure 1.2.

The concept of a glass transition temperature is important in a wide range of viscoelastic material applications that include changing temperature conditions. Hence, to better define T_g, let us consider a stress-free sample of material subject to a uniform and changing temperature field. A measurement of the volume change from some initial volume has the characteristic shown in Figure 1.4: the temperature at which the slope has a discontinuity is referred to as the glass transition temperature. The slope discontinuity accounts for the sharp transition between rubbery and glassy regions. Furthermore, the additional volume above this temperature is considered to be *free volume*, or voids in the molecular scale. Hence, Figure 1.4 also caters to a molecular interpretation for the glassy and rubbery behavior. In fact, at low temperatures, due to the volumetric shrinking, the polymer backbones have little freedom of movement, and the modulus is relatively stiff; nevertheless, the loss tangent may present peaks. As depicted in Figure 1.2, in the glassy region, a wide band of relatively small damping is superposed to small peaks, known as *secondary maxima*, in the loss tangent. Among these, the peak at the lowest temperature, the γ peak, is thought to be caused by the flexing or twisting of segments of the main polymer chain. A β peak may be obtained at higher temperatures, and thermorheological complexity can be observed if both the α peak and the β peak are present in the same frequency window [60].

On the other hand, at high temperatures, the individual molecules now have a considerable deal of mobility with very little restriction thanks to the volume expansion, which is shown macroscopically in a low value for the modulus. Thus, long-chain molecule entanglements control the rubbery behavior, and the asymptotic or equilibrium modulus at the terminal region depends upon the cross-link density and molecular weight. If given enough time or thermal activation at a high temperature, molecular chains in polymers without cross-links can slide over one another, and the behavior, then, resembles that of

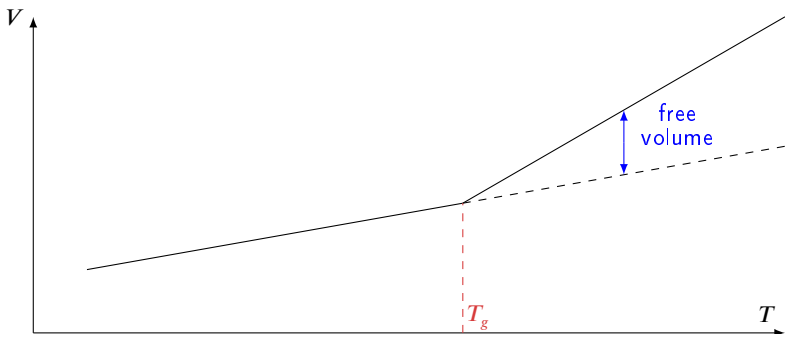

Figure 1.4: Volume as a function of temperature in polymers.

liquids [55]. The main complexity of this definition of the glass transition temperature, based on free volume changes, is that it is also a time-dependent measurement, as confirmed by Kovacs [61]. Therefore, an additional definition of T_g is presented, based upon the loss tangent [51]. To this regard, as previously pointed out, the loss tangent may exhibit more than a peak, but there is a local maximum close to the same frequency at which the largest variation with frequency of the storage modulus, that is, the real part of the complex modulus, is retrieved. Then, as shown in Figure 1.3 and in Ref. [51], there is a single space curve connecting the relative maxima of the loss tangent, whose projection onto the temperature-frequency plane is taken as that of the glass transition temperature as a function of frequency $T_g = f(\omega)$. It is clear how such a relationship is fundamental to assessing whether a material will respond in a rubbery or glassy manner at a particular frequency of excitation. It is important to underline that glass transition temperature may be controlled by adding various constituents, e.g., a plasticizer may be added to reduce T_g: indeed, small molecules included in plasticizers pierce the polymer and increase the mobility of individual molecular chain segments [62]. On the other hand, particulate inclusions tend to slightly raise T_g, as the free volume is reduced in the vicinity of the interface.

Interestingly, there are materials with a special type of temperature dependence of mechanical properties known as *thermorheologically simple* [63–65]. In particular, the mathematical description of such temperature dependence is formulated in Ref. [51] for constant temperature states. We indicate with $G(t)$ the relaxation function at the base temperature T_0, and we let the temperature field be changed uniformly, i.e. independently of the spatial coordinates, such that the relaxation function corresponding to an absolute temperature equal to T is designated as $\mathcal{G}(t, T)$. Clearly, at the base temperature T_0, we have $\mathcal{G}(t, T_0) = G(t)$. Changing the independent variable in $G(t)$, it is possible to write $G(t) = L(\log_{10} t)$. Now, a material is referred to as thermorheologically simple if it behaves according to the following relationship:

$$\mathcal{G}(t, T) = L(\log_{10} t + \psi_T(T)), \tag{1.25}$$

with $\psi_T(T)$ being a shift function, which obeys the relations $\psi_T(T_0) = 0$ and $d\psi_T(T)/dT > 0$. In particular, Equation (1.25) states that a change in temperature causes the relaxation function to be shifted along the time axis. This postulate is also referred to as *time-temperature superposition principle*.

Now, setting $\psi_T(T) = \log_{10} a_T(T)$, we have that $a_T(T_0) = 1$ and $da_T(T)/dT > 0$, and Equation (1.25) can be rephrased as $\mathcal{G}(t, T) = L(\log_{10} t a_T(T))$ and, thereafter, we

have that

$$\mathcal{G}(t,T) = G(\zeta), \tag{1.26}$$

with $\zeta = ta_T(T)$. This result explains that the relaxation function at any temperature T, that is $\mathcal{G}(t,T)$, can be obtained from the relaxation function at the base temperature T_0, i.e. $G(t)$, by replacing t with ζ. For the sake of completeness, the relationship (1.26) is sometimes taken in the expanded form $\mathcal{G}(t,T) = b_T(T)G(\zeta)$, with $b_T(T) = \rho T/\rho_0 T_0$, ρ_0 being the initial density. Therefore, together with the shift of the data along the time axis, which is taken into account from ζ, $b_T(T)$ is responsible for the shifting of the data along the G axis, due to the change of density and temperature. Usually, this effect is small compared with the time scale shift, and, hence, neglected.

A similar approach can be used to formulate a proper description of the temperature dependence of complex moduli: the complex modulus at any temperature T can be obtained from the complex modulus $G^*(\omega)$ at the base temperature by replacing ω with $\omega/a_T(T)$. The same reasoning holds for creep functions.

1.3 Rheological models

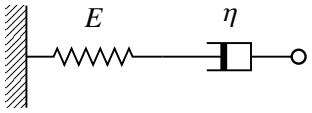

Figure 1.5: Schematic of the Maxwell model.

In this Section, the most common models of viscoelastic materials are analyzed. Let us start with the Maxwell model, sketched in Figure 1.5. It is constituted by a purely elastic spring and a purely viscous damper connected in series. First, we notice that, from the equilibrium of each component, it is possible to write:

$$\sigma(t) = E\varepsilon_s(t) \rightarrow \ \dot{\varepsilon}_s(t) = \frac{\dot{\sigma}(t)}{E}, \tag{1.27a}$$

$$\sigma(t) = \eta(\dot{\varepsilon}_d(t) - \dot{\varepsilon}_s(t)) = \eta\dot{\varepsilon}_d(t) - \eta\frac{\dot{\sigma}(t)}{E}, \tag{1.27b}$$

so that we retrieve the following linear differential equation

$$\frac{\dot{\sigma}(t)}{E} + \frac{\sigma(t)}{\eta} = \dot{\varepsilon}_d(t). \tag{1.28}$$

Now, considering an input step strain, the stress $\sigma(t)$ will be equal to the relaxation function $G(t)$. Substituting it into Equation (1.28):

$$\dot{G}(t) + \frac{1}{\tau}G(t) = E\delta(t), \tag{1.29}$$

where τ is the relaxation time and it is equal to $\tau = \eta/E$.
First, let us integrate both members of Equation (1.29) in the time interval $t \in [0^-, 0^+]$:

$$\int_{0^-}^{0^+} \dot{G}(t)\mathrm{d}t + \int_{0^-}^{0^+} \frac{1}{\tau}G(t)\mathrm{d}t \ = E\int_{0^-}^{0^+} \delta(t)\mathrm{d}t, \tag{1.30}$$

where we reckon that the second term of the sum at the left-hand side can be neglected since the interval of integration is so small that we can consider as null the variation undergone by the function $G(t)$. Thus we obtain $G(0^+) - G(0^-) = E\int_{0^-}^{0^+} \delta(t)\mathrm{d}t = E$ and, finally, recalling causality, the initial condition for the relaxation function can be found as $G(0^+) = E$. Incidentally, it is possible to understand that, once the input signal is applied, the damper behaves as a rigid body and, consequently, the system behaves as an elastic solid.
Now, for $t > 0$, Equation (1.29) is a homogeneous differential equation, as the Dirac delta vanishes. In particular, we have:

$$\dot{G}(t) + \frac{1}{\tau}G(t) = 0 \tag{1.31}$$

and, together with the initial condition $G(0^+) = E$, it is straightforward to determine the relaxation function $G(t)$, which is equal to

$$G(t) = E\ e^{-t/\tau}\mathcal{H}(t). \tag{1.32}$$

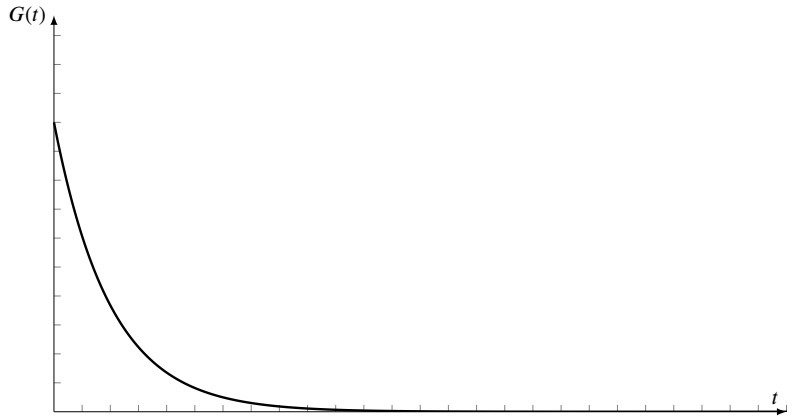

Figure 1.6: Relaxation function $G(t)$ as function of time for the Maxwell model.

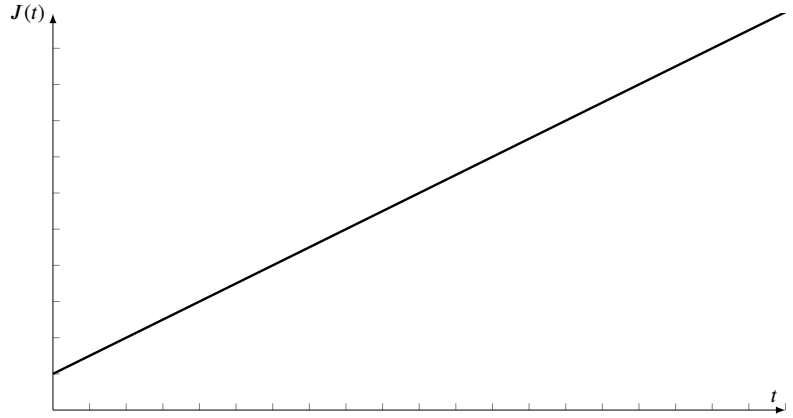

Figure 1.7: Creep function $J(t)$ as function of time for the Maxwell model.

Equation (1.32) points out a very important property of the Maxwell model: the relaxation function of the material goes to zero at very large times (see Figure 1.6). Hence, the Maxwell model resembles a viscoelastic fluid, where the viscous part, i.e. the damper, can be seen as a Newtonian fluid, and the elastic component, i.e. the spring, behaves like a solid body.

Now, we analyze the system response to a step stress input, i.e. $\sigma(t) = \mathcal{H}(t)$. Since the two elements constituting the model are in a series configuration, the total strain $\varepsilon(t)$ is equal to $\varepsilon(t) = \varepsilon_s(t) + \varepsilon_d(t)$; consequently the creep function $J(t)$ is equal to:

$$J(t) = \left(\frac{1}{E} + \frac{t}{\eta}\right)\mathcal{H}(t). \tag{1.33}$$

Thus, the predicted creep response is a straight line, but this form is unrealistic for primary creep, since it is in contrast to the curves that are observed experimentally.

Now, the response of the system to a circular input function is investigated: moving to the frequency domain, it is possible to study the behavior of the system by using the equivalent complex modulus of two viscoelastic materials connected in series, i.e. $1/G^*(\omega) = \sum_i 1/G_i^*(\omega)$, with $G_i^*(\omega)$ being the viscoelastic complex modulus of the i-th

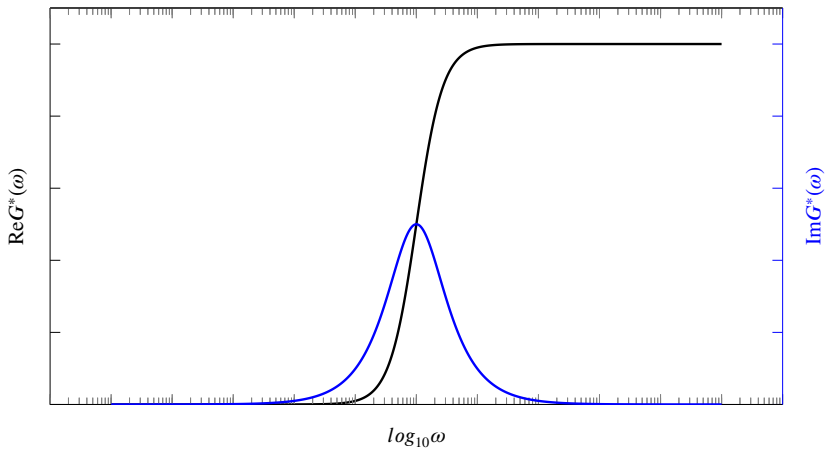

Figure 1.8: The real part of the viscoelastic complex modulus of the Maxwell model Re$G^*(\omega)$ (solid black line on the left), and the imaginary part of the viscoelastic complex modulus of the Maxwell model Im$G^*(\omega)$ (solid blue line on the right) as function of the frequency ω.

element the system is composed by. Specifically, for the Maxwell model, we have:

$$G^*(\omega) = E\frac{i\omega\eta}{E + i\omega\eta} = E\frac{i\omega\tau}{1 + i\omega\tau} = \frac{E\omega^2\tau^2}{1 + \omega^2\tau^2} + i\frac{E\omega\tau}{1 + \omega^2\tau^2} \tag{1.34}$$

Figure 1.8 shows the real and imaginary parts of the viscoelastic complex modulus, as functions of ω, for an arbitrary value of the characteristic time τ. Incidentally, looking at the real part of the complex modulus, it is possible to notice that the material behaves as a liquid at very low frequencies, while, at very high frequencies, the material enters the glassy region, where it behaves like a solid elastic body; instead, at intermediate frequencies viscoelasticity effects take place and high energy dissipation occurs, as shown in Figure 1.8 by the imaginary part of $G^*(\omega)$, which vanishes at very low- and very high-frequencies.

Next, let us consider another model: the standard linear solid. It is constituted by a Maxwell model and a purely elastic spring in parallel, as illustrated in Figure 1.9, and the total stress applied to the system will be the sum of the stress applied on each branch. In particular, with reference to Figure 1.9, we can derive the expression for the relaxation modulus $G(t)$ as:

$$G(t) = (E_0 + E_1 e^{-t/\tau})\mathcal{H}(t) \tag{1.35}$$

It is possible to observe a decreasing trend of the relaxation function for increasing times: for very long times, the spring with stiffness $G(t \to \infty) = E_0$ is the only one reacting to the applied load, and the system behaves as a solid. On the other hand, as explained previously, as soon as the stress is applied, the damper behaves as a rigid body, so that the system behaves again as an elastic solid, though stiffer than it is at long times; indeed, the equivalent stiffness of the system as $t \to 0$ is equal to $G(t \to 0) = E_0 + E_1 = E_\infty$. This is highlighted in Figure 1.10, where the relaxation function is plotted as function of time, for an arbitrary value of the characteristic time τ.

To obtain the expression for the creep function, let us analyze the response of the system for a step stress input. In particular, it is possible to write the following differential

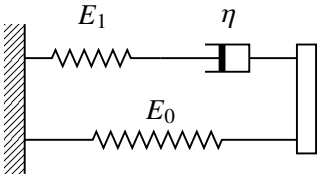

Figure 1.9: Schematic of the standard linear solid model.

equation:

$$\dot{J}(t) + \frac{1}{\beta\tau} J(t) = \frac{1}{E_\infty}\left(\delta(t) + \frac{1}{\tau}\mathcal{H}(t)\right), \tag{1.36}$$

where $\beta = E_\infty/E_0$. Now, we observe that the particular solution J_p of Equation (1.36) can be expressed in terms of the system equilibrium as $t \to \infty$; specifically, when the equilibrium condition is reached, the derivative of $J(t)$ vanishes, so that for $t > 0$ it is possible to write $J_\infty/\beta\ \tau = 1/E_\infty\tau$, whence:

$$J_p = J_\infty = \frac{\beta}{E_\infty} = \frac{1}{E_0} \tag{1.37}$$

On the other hand, when $t \in [0^-, 0^+]$, integrating both sides of Equation (1.36):

$$\int_{0^-}^{0^+} \dot{J}(t)\mathrm{d}t + \int_{0^-}^{0^+} \frac{1}{\beta\tau} J(t)\mathrm{d}t = \int_{0^-}^{0^+} \frac{\mathcal{H}(t)}{\tau E_\infty}\mathrm{d}t + \int_{0^-}^{0^+} \frac{1}{E_\infty}\delta(t)\mathrm{d}t \tag{1.38}$$

Then, since the integrating interval is too small to provide appreciable variations of $J(t)$, it is possible to neglect the corresponding integral and, recalling that the creep function obeys causality, the initial condition of the system is:

$$J(0^+) = \frac{1}{E_\infty}. \tag{1.39}$$

Finally, solving the associated homogeneous differential equation

$$\dot{J}(t) + \frac{1}{\beta\tau} J(t) = 0, \tag{1.40}$$

we retrieve the expression of the creep function for the standard linear solid:

$$J(t) = \left[\frac{1}{E_0} + \left(\frac{1}{E_\infty} - \frac{1}{E_0}\right) e^{-\dfrac{t}{\beta\tau}}\right]\mathcal{H}(t) \tag{1.41}$$

Figure 1.11 illustrates the creep function of the standard linear viscoelastic model as a function of time, for an arbitrary value of the relaxation time τ.

As for the Maxwell model, let us analyze the response of the standard linear model when subject to circular functions as input signals. Recalling the expression for the equivalent viscoelastic complex modulus for a parallel configuration, i.e. $G^*(\omega) = \sum_i G_i^*(\omega)$, it is possible to write:

$$G^*(\omega) = E_0 + E_1\frac{i\omega\tau}{1 + i\omega\tau} = \left(E_0 + E_1\frac{\omega^2\tau^2}{1 + \omega^2\tau^2}\right) + i\left(E_1\frac{\omega\tau}{1 + \omega^2\tau^2}\right) \tag{1.42}$$

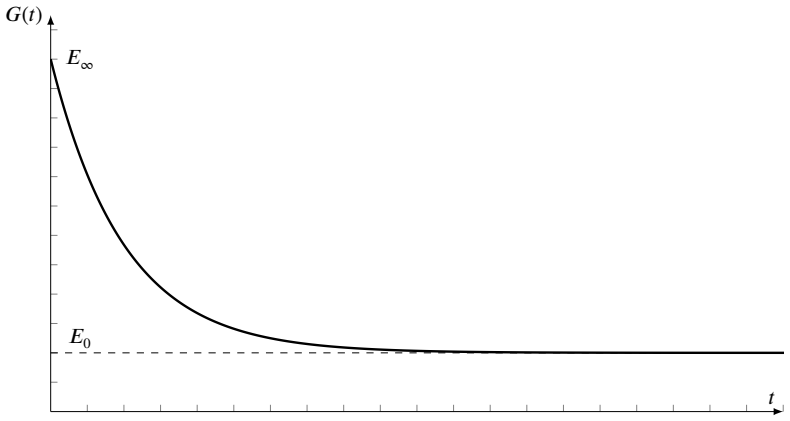

Figure 1.10: Relaxation function $G(t)$ as function of time for the standard linear solid model.

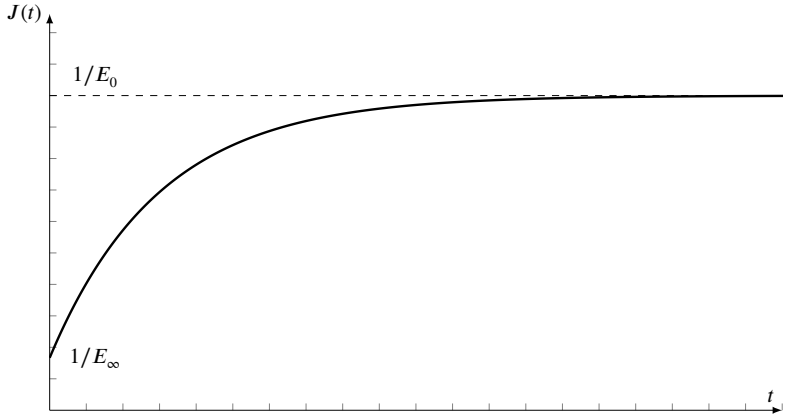

Figure 1.11: Creep function $J(t)$ as function of time for the standard linear solid model.

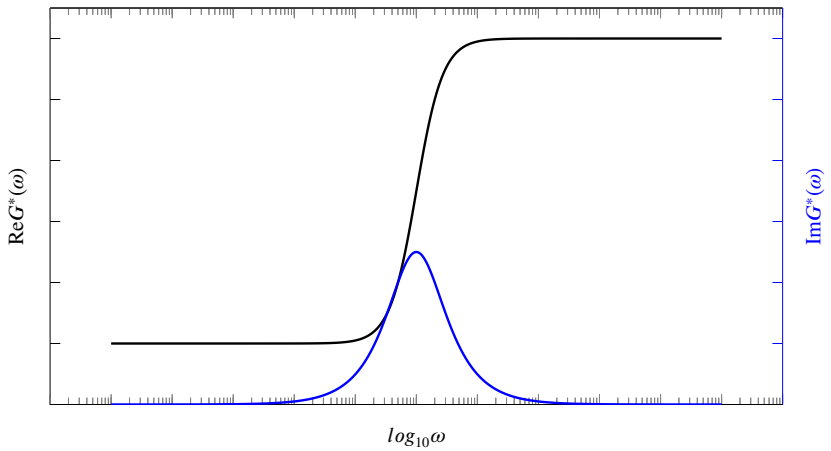

Figure 1.12: The real part of the viscoelastic complex modulus of the standard linear solid model $\mathrm{Re}G^*(\omega)$ (solid black line on the left), and the imaginary part of the viscoelastic complex modulus of the standard linear solid model $\mathrm{Im}G^*(\omega)$ (solid blue line on the right) as function of the frequency ω.

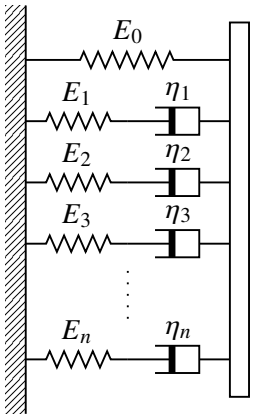

Figure 1.13: Schematic of the generalized Maxwell model.

Figure 1.12 illustrates the real and imaginary parts of the viscoelastic complex modulus, as functions of ω. Observe that at very low- and very high-frequencies the system behaves as an elastic solid, with modulus being equal to $G^*(\omega \to 0) = E_0$ and $G^*(\omega \to \infty) = E_0 + E_1$ respectively, and the energy dissipation is negligible. Instead, at intermediate frequencies, a transition region, characterized by high energy dissipation, is observed.

However, real polymers are characterized by a continuous spectrum of relaxation times, and it is clear that such single relaxation time models are not able to properly describe real viscoelastic materials. Indeed, a single relaxation time material undergoes most of its relaxation over about one decade in time scale, hence it undergoes a very abrupt transition; conversely, real materials relax (or creep) over many decades of time scales. Therefore, it is possible to consider a model, whose relaxation function is represented by the sum of a constant and a series of decaying exponential terms: this model is referred to as the Weichert model or the generalized Maxwell model. Specifically, it is composed of a purely elastic spring in parallel with as many Maxwell branches as are needed to approximate the material response satisfactorily (see Figure 1.13). For such a model, it is then possible to write the expressions of the relaxation function $G(t)$ as

$$G(t) = (E_0 + \sum_{j=1}^{n} E_j e^{-t/\tau_j})\mathcal{H}(t), \tag{1.43}$$

while the viscoelastic complex modulus is equal to:

$$G^*(\omega) = E_0 + \sum_{j=1}^{n} E_j \frac{i\omega\tau_j}{1 + i\omega\tau_j}. \tag{1.44}$$

Chapter 2

Dry circular contacts

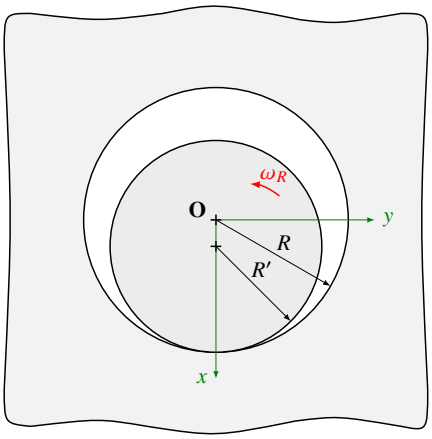

Figure 2.1: Schematic of the rigid pin rolling into a cylindrical hole on a viscoelastic infinite space.

In this Chapter, an efficient Boundary Element approach for viscoelastic circular contact mechanics is presented. Crucially, it is valid for both conforming and non-conforming surfaces. Incidentally, in conforming contacts, the contact area dimension is not negligible with respect to the characteristic dimension of the contact domain [66,67], so the half-plane approximation, usually done in non-conforming problems, is not able to properly assess the contact problem.

Therefore, in the following Sections, particular attention is paid to steady-state contacts, and the crucial point is the derivation of the viscoelastic Green's function that intrinsically accounts for the circular domain. In particular, at first the paradigmatic problem of a pin rolling, with a constant angular velocity ω_R, into a cylindrical hole on a viscoelastic infinite space is considered (see Figure 2.1). Nevertheless, the present methodology is not limited to single relaxation time materials, as it is able to deal with any real viscoelastic material, characterized by a wide spectrum of relaxation times.

Furthermore, one of the main purposes of the formulation is to quantify the hysteretic dissipation contribution to the overall friction. This is of the utmost importance in mechanics to provide an enhanced understanding of the behavior of a variety of tribosystems, in which soft materials are involved; consequently, this would lead the way to tailor the operating characteristics to obtain a specific response of the system. Crucially,

as discussed later, the Boundary Element methodology here introduced is not restricted to such *single* contact problems; indeed, it blazes the trail to investigations of multiple contact problems, such as the rolling element bearing, and lubricated contact problems, such as the journal bearing, the latter thoroughly discussed in the next Chapter. As a matter of fact, it will be evident how viscoelasticity strongly affects the response of these machine elements, and how a clear understanding of these effects is critical in rotor-dynamics in a large variety of industrial applications.

2.1 Mathematical formulation

As presented in Chapter 1, the creep response of a linear viscoelastic material may be described through Equation (1.5), namely:

$$\varepsilon(t) = \int_{-\infty}^{t} d\tau \, J(t-\tau)\dot{\sigma}(\tau) \tag{2.1}$$

where $\varepsilon(t)$ is the time-dependent strain, $\dot{\sigma}(t)$ is the time derivative of the stress and $J(t)$ is indeed the so-called creep function. We recall that the creep function must satisfy the causality principle: this means that $J(t)$ has to vanish for a time $t < 0$. The most general form of $J(t)$ is:

$$J\left(t\right) = \mathcal{H}\left(t\right)\left[1/E_0 - \int_0^{+\infty} d\tau \, \mathcal{C}\left(\tau\right) \exp\left(-t/\tau\right)\right], \tag{2.2}$$

where $\mathcal{H}(t)$ is the Heaviside step function, and the real quantity E_0 is the rubbery modulus (i.e. the low-frequency modulus) of the viscoelastic material, $C(t)$ is a positive function known as the creep (or retardation) spectrum, and τ is the relaxation time. As discussed beforehand, real viscoelastic materials are characterized by a continuously distributed relaxation times spectrum, though, in numerical simulations, a discrete form of the creep compliance in Equation (2.1) is generally preferred. Hence, we write:

$$J\left(t\right) = \mathcal{H}\left(t\right)\left[1/E_0 - \sum_{k=1}^{n} C_k \exp\left(-t/\tau_k\right)\right], \tag{2.3}$$

or, alternatively, considering that $J\left(t=0\right) = 1/E_\infty$, where E_∞ is the glassy modulus (i.e. the high-frequency modulus) of the material, as

$$J\left(t\right) = \mathcal{H}\left(t\right)\left[1/E_\infty + \sum_{k=1}^{n} C_k \left(1 - \exp\left(-t/\tau_k\right)\right)\right]. \tag{2.4}$$

Now, let us start defining the geometry under investigation. Specifically, we are focusing on the contact problem involving a pin in a bushing: as we assume plane strain conditions, the system is studied as two-dimensional and, as sketched in Figure 2.1, can be modeled as a circular punch placed in a cylindrical hole on an infinite space. Now, in order to show in a clearer way the paradigmatic features of this system, the pin, and the space are considered respectively as rigid and deformable. We note that the system is rotationally invariant. Hence, recalling the elastic-viscoelastic correspondence

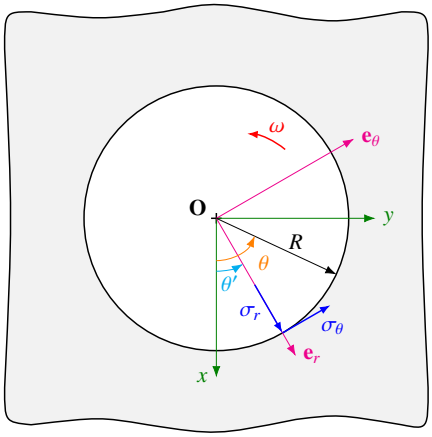

Figure 2.2: Schematic of a cylindrical hole drilled throughout a viscoelastic infinite space, subjected to plane strain conditions. An isolated load is applied to the boundary of the hole.

principle [22, 55, 68–70] [1], the displacement $\mathbf{u} = u_r\mathbf{e}_r + u_\theta\mathbf{e}_\theta$ can be related to the stress $\boldsymbol{\sigma} = \sigma_r\mathbf{e}_r + \sigma_\theta\mathbf{e}_\theta$, through the following integral equation:

$$\mathbf{u}(s,t) = \int_{-\infty}^{t} dt' \int_{0}^{2\pi R} ds'\, J(t-t')\mathbf{G}(s-s')\dot{\boldsymbol{\sigma}}(s',t'), \tag{2.5}$$

where $s = R\theta$ and $s' = R\theta'$, with R being the hole radius, t is the time and, most importantly, $\mathbf{G}(s)$ is the spatial Green's tensor. Incidentally, in Equation (2.27), we observe that the characteristic velocity at which the phenomenon occurs is assumed much smaller than the wave propagation speed in the viscoelastic medium: this implies that all the inertial effects can be neglected. According to the polar reference system sketched in Figure 2.2, we have defined $\mathbf{e}_r$ as the radial unit vector and $\mathbf{e}_\theta$ the tangential one.

Now, moving from the complex potentials theory, extensively treated by Stevenson [42] and Muskhelishvili [43], and briefly presented in the Appendix, all the different components of this tensor have been calculated, and can be found in Appendix A.2.

In the following developments, we will neglect tangential stresses σ_θ, and we will focus only on the radial displacement u_r at the interface. Recall that the coupling between normal and tangential stresses may become critical in applications in which the thickness of the viscoelastic tribopartner is extremely low: in this case, a certain deviation from the solution given by the purely normal case may be expected [71, 72]. However, in the application under consideration, this has to be ruled out as the thickness of the contacting bodies is much larger than each contact patch: as a consequence, we can consider uncoupled the normal and the tangential problems. Hence, the assumption of neglecting tangential stresses for the aim of the present analysis is well posed.

[1] The correspondence principle, also known as the elastic-viscoelastic analogy, states that if a solution to a linearly elastic problem is known, the solution to its corresponding linearly viscoelastic problem can be found by substituting each quantity that depends on time with the Laplace transform multiplied by the transform variable, e.g. $p(t) \to sp(s)$, where $p(s)$ denotes the Laplace transform of the function $p(t)$, and then transforming back to the time domain. Thus, the enormous collection of static solutions can be converted into quasi-static viscoelastic solutions. However, the principle cannot be employed for boundary value problems in which the type of boundary condition varies with time at a point on the surface of the body, such as from specified displacement to prescribed traction.

Thus, from Equation (2.27) we get the following scalar equation:

$$u_r(s,t) = \int_{-\infty}^{t} dt' \int_0^{2\pi R} ds'\, J(t-t') G_{rr}(s-s') \dot{\sigma}_r(s',t'), \tag{2.6}$$

where G_{rr} can be obtained as

$$G_{rr}(s) = \frac{1+\nu}{2\pi}\left[-\frac{\kappa}{\kappa+1}(2\log R + 1)\cos\theta - \frac{\kappa+1}{2}\mathrm{B}(\theta)\cos\theta + (\kappa-1)\mathrm{A}(\theta)\sin\theta \right], \tag{2.7}$$

with $\theta = s/R$ being the angle subtended by the arc s, ν is the Poisson's ratio, and κ is the Kolosov's constant equal to $\kappa = 3-4\nu$ and $\kappa = (3-\nu)/(1+\nu)$ for plane strain and plane stress problems respectively. Furthermore, the terms $\mathrm{A}(\theta)$ and $\mathrm{B}(\theta)$ are equal to $\mathrm{A}(\theta) = \arg(1/2 - i/2\cot(\theta/2))$ and $\mathrm{B}(\theta) = \log(2-2\cos\theta) = 2\log(2|\sin(\theta/2)|)$.

As shown in Appendix A.2, let us observe that G_{rr} is the purely radial term due to a normal stress σ_r equal to a Dirac delta load, i.e., $\sigma_r = \delta(s)$. Interestingly, G_{rr} is the sum of two terms: one is the radial component of the mean displacement due to a radial force, that is, $\bar{G}_{rr} = (\kappa(1+\nu)/2\pi(\kappa+1))(2\log R + 1)\cos\theta$; the other one is an additional term that varies with the angle and, specifically, is equal to $\tilde{G}_{rr} = ((\kappa-1)\mathrm{A}(\theta)\sin\theta - (1/2)(\kappa+1)\mathrm{B}(\theta)\cos\theta)(1+\nu)/2\pi$. This is usual in two-dimensional elasticity [66], but, in this case, differently from the case of half-plane problems, we can quantify the mean term $\bar{G}_{rr}$. Physically speaking, this is possible as the system has a characteristic length scale, that is the radius R: for this reason, the mean term keeps finite and, thus, could be experimentally measured. Consistently, when R tends to infinity, also such a mean contribution diverges. Furthermore, notice that, for a Poisson's ratio $\nu = 0.5$, the additional term $\tilde{G}_{rr}$ is identical to the elastic Green's function obtained by Carbone and Mangialardi in Ref. [73,74], properly rotated in a polar reference frame.

Now, by focusing on Equation (2.6), let us observe that we can exchange the order of integration and rewrite it as:

$$u_r(s,t) = \int_0^{2\pi R} ds'\, G_{rr}(s-s') \int_{-\infty}^{t} dt'\, J(t-t')\, \dot{\sigma}_r(s',t'), \tag{2.8}$$

where the term $\int_{-\infty}^{t} dt'\, J(t-t')\dot{\sigma}_r(s',t')$ can be integrated by parts leading to:

$$\begin{aligned} u_r(s,t) =& J(0)\int_0^{2\pi R} ds'\, G_{rr}(s-s')\,\sigma_r(s',t) + \\ &+ \int_{-\infty}^{t} dt' \int_0^{2\pi R} ds'\, \dot{J}\left(t-t'\right) G_{rr}\left(s-s'\right)\sigma_r(s',t'). \end{aligned} \tag{2.9}$$

Recalling that the rigid pin is rotating at constant angular velocity ω_R, we can write $\sigma_r(s,t) = \sigma_r(s-\omega R t)$ and $u_r(s,t) = u_r(s-\omega R t)$, where ω is the angular velocity of the contact patch equal to $\omega = -\omega_R R'/(R-R')$, with R' being the radius of the pin, as sketched in Figure 2.1. Applying the transformation rule $S = s - \omega R t$ and recalling linearity and rotational invariance, it is possible to write:

$$u_r(S) = \int_0^{2\pi R} dS'\, \mathcal{G}_{rr}(S-S',\omega)\,\sigma_r(S'), \tag{2.10}$$

where $\mathcal{G}_{rr}$ is the steady-state viscoelastic Green's function. The latter can be found by assuming in Equation (2.9) that the stress distribution at the interface is a Dirac-delta

distribution, moving at a constant angular velocity, that is, $\sigma_r(s,t) = \delta(s - \omega Rt)$:

$$\begin{aligned}\mathcal{G}_{rr}(s-\omega Rt) =& J(0)\int_0^{2\pi R} ds'\, G_{rr}(s-s')\delta(s'-\omega Rt)+ \\ &+\int_{-\infty}^{t} dt' \int_0^{2\pi R} ds'\, \dot{J}(t-t')\, G_{rr}\left(s-s'\right)\delta\left(s'-\omega Rt'\right).\end{aligned} \tag{2.11}$$

Now, by observing that for $\omega t > 2\pi$ or $\omega t < 0$ we necessarily have $\delta\left(s - \omega Rt\right) = 0$, since s satisfies the condition $0 < s < 2\pi R$. Thus, we can write:

$$\mathcal{G}_{rr}(s-\omega Rt) = J(0)\, G_{rr}(s-\omega Rt) + \int_0^{2\pi/\omega} dt'\, \dot{J}(t-t')\, G_{rr}\left(s-\omega Rt'\right). \tag{2.12}$$

Then, applying the transformation rule $t - t' = \lambda$, we get:

$$\mathcal{G}_{rr}\left(s-\omega Rt\right) = J(0)\, G_{rr}\left(s-\omega Rt\right) + \int_{t-2\pi/\omega}^{t} d\lambda\, \dot{J}(\lambda)\, G_{rr}\left(s-\omega Rt+\omega R\lambda\right), \tag{2.13}$$

where $\dot{J}\left(\lambda\right) = \int_0^{+\infty} d\tau\, \exp(-\lambda/\tau)\left(C\left(\tau\right)/\tau\right)$. Enforcing periodicity, recalling that $S = s - \omega Rt$, and changing the integration variable λ as $\lambda = \tau\zeta$, we obtain:

$$\mathcal{G}_{rr}\left(S\right) = J(0) G_{rr}\left(S\right) + \int_0^{+\infty} d\tau\, C\left(\tau\right) \int_0^{2\pi/\omega\tau} d\zeta\, e^{-\zeta} G_{rr}\left(S+\omega R\tau\zeta\right). \tag{2.14}$$

It is interesting to observe that, unlike what happens in a plane system, where a cartesian reference frame is employed (the reader is referred to Ref. [22]), here the integration interval for the $\zeta-$variable is finite and, specifically, equal to $[0, 2\pi/\omega\tau]$. From a physical point of view, this is again due to the intrinsic features of the geometric domain under investigation: in a half-plane, the contacting surface is infinite, whilst, in a circular domain, this is finite and the viscoelastic memory effect can be related to nothing else than the circumference size. The latter is indeed the characteristic dimension of the system. Let us notice that, recalling that the angular velocity ω can be expressed as $\omega = v/(R - R')$, with v being the sliding/rolling linear velocity, the upper limit of integration in Equation (2.14) is $2\pi(R - R')/v\tau$. By taking the limit as $R \to \infty$, consistently with a system that tends to behave like a half-plane, we retrieve the same viscoelastic Green's function obtained by Carbone and Putignano [22]. This not only corroborates Equation (2.14) but leads, to some extent, to a generalization of the methodology in Ref. [22].

Once $\mathcal{G}_{rr}(S)$ is found, in order to numerically solve the contact problem, we can discretize the contact domain with N elements, each covering an arc of length $2\alpha R$, and, assuming that for each element the stress is constant and equal to $\sigma_k = \sigma_r(S_k)$, where S_k is the angular position of the center of the k-th interval, the radial displacement $u_i = u_r(S_i)$ at the center of the i-th interval is:

$$u_i = \sum_{k=1}^{N} \sigma_k \int_{S_k-\alpha R}^{S_k+\alpha R} dS'\, \mathcal{G}_{rr}(S_i - S', \omega) \tag{2.15}$$

with the assumption that the discretization step is small enough to consider the stress $\sigma_k = \sigma_r(S_k)$ constant on an arc $[S_k - \alpha R, S_k + \alpha R]$.

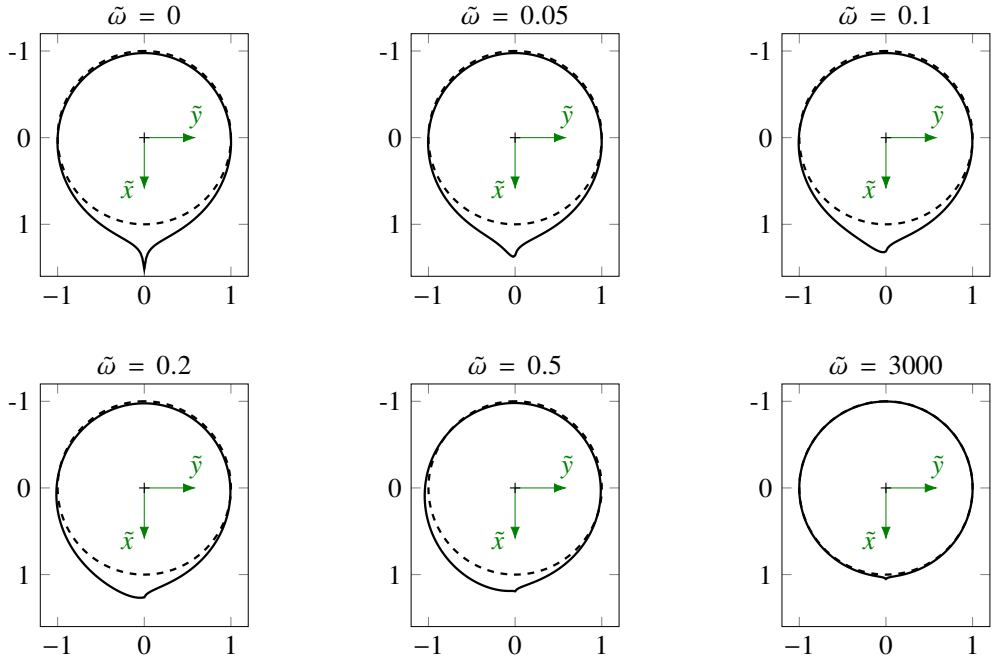

Figure 2.3: The undeformed profile (dashed black line) and the magnified deformed profile (solid black line), with $K = 10^7$ being the magnification factor, as a result of the application of a radial unit pressure distribution in the arc $[-\alpha R, \alpha R]$ for different values of the dimensionless speed $\tilde{\omega} = \omega\tau$. The numerical results are carried out for a viscoelastic material, characterized by a single relaxation time $\tau = 0.01$ s, glassy and soft moduli respectively equal to $E_\infty = 10^7$ Pa and $E_0 = 10^6$ Pa, Poisson's ratio $\nu = 0.5$, with $\alpha = 7.85 \cdot 10^{-3}$ and $R = 0.08$ m. The axes $\tilde{x}$ and $\tilde{y}$ refer to the normalized x- and y-coordinates, i.e., $\tilde{x} = x/R$ and $\tilde{y} = y/R$.

Now, in order to further develop Equation (2.34), let us introduce $\mathcal{L}_{rr}(S)$ as:

$$\mathcal{L}_{rr}(S) = J(0)L_{rr}(S) + \int_0^{+\infty} d\tau\, C(\tau) \int_0^{2\pi/\omega\tau} dz\; e^{-z}\, L_{rr}(S + \omega R\tau z), \tag{2.16}$$

where

$$L_{rr}(S) = \int_0^{2\pi R} dS'\, G_{rr}(S - S')\chi_r\left(S'\right), \tag{2.17}$$

with χ_r being a pressure unitary in the arc $[-\alpha R, \alpha R]$ and vanishing outside. The mathematical details on $L_{rr}(s)$ can be found in Appendix A.2. Figure 2.3 represents, in the polar reference system, $\mathcal{L}_{rr}(S)$ for increasing values of the dimensionless speed $\tilde{\omega} = \omega\tau$. The deformation is magnified to better appreciate the viscoelastic effects. Indeed, we observe that the deformed profile is symmetrical at very low-speed and very high-speed values, where the material enters respectively the rubbery and the glassy elastic regions. For intermediate velocity, we have the proper viscoelastic effects: the displacement is larger upon the pressure distribution passage as the material is still relaxing; hence, the marked non-symmetric trend in Figure 2.3 occurs.

Now, given the definition of $\mathcal{L}_{rr}$, Equation (2.34) can be rephrased as the following system of linear equations [22, 73, 75]:

$$u_i = \mathcal{L}_{ik}(\omega)\sigma_k, \tag{2.18}$$

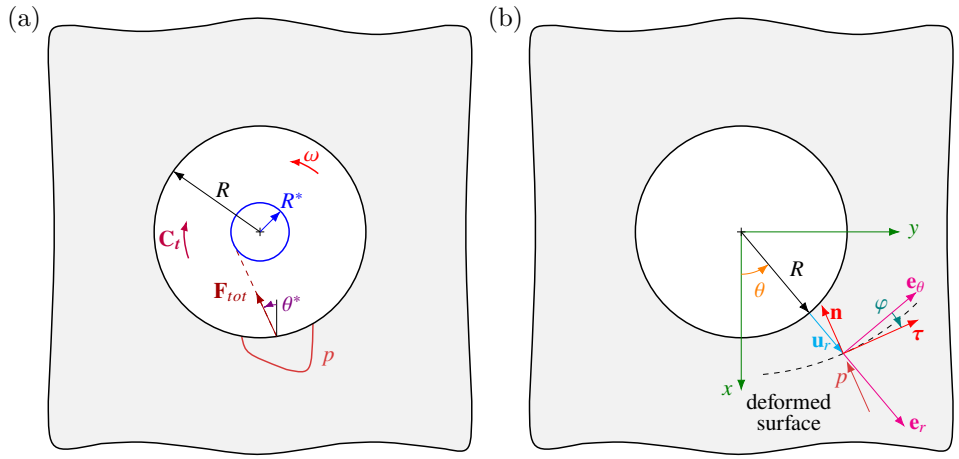

Figure 2.4: Schematic of the radial displacement $\mathbf{u}_r$ and the resulting deformed surface (black dashed line) with the normal and tangential unit vectors being $\mathbf{n}$ and $\boldsymbol{\tau}$ respectively (a); the total force $\mathbf{F}_{tot}$ as the integral of the pressure distribution p, the viscoelastic friction torque $\mathbf{C}_t$, the friction circumference (solid blue line) and the attitude angle θ^* (b).

where $\mathcal{L}_{ik} = \mathcal{L}_{rr}(S_i - S_k, \omega)$. Equation (2.36) is, then, solved following the scheme proposed by Carbone and Putignano [22]. Indeed, although we are dealing with a two-dimensional problem, we can fix the absolute penetration value, as in Equation (2.6) the Green's functions accounts also for the mean displacement that the deformable body will experience.

Now, once the total penetration is fixed, the displacement distribution in the contact area is found on a geometrical basis; then, by inverting the relation (2.36), the stress distribution is determined. Clearly, as in any contact problem, the contact area is not known a priori: thus, the numerical solver implements an iterative procedure, where, at each iteration, the elements with negative pressure are removed, and those for which numerical compenetration occurs are added.

Once the contact solution is known, a crucial point in the present analysis deals with the viscoelastic contribution to friction. To this aim, without any loss of the generality for the formulation, let us focus again on the simple case of a pin in contact with the contour of a cylindrical hole on an infinite space: the key quantity to take into account is the contact pressure p acting on the pin. This one is equal to $|\sigma_r|$ and directed as reported in Figure 2.4a. In particular, Figure 2.4a includes a magnified view of the deformed system: the pressure direction is along the unit vector $\mathbf{n}$ being normal to the deformed surface element $dl = (R + u_r)d\theta/\cos\varphi$, with u_r being the radial displacement and φ the angle between $\mathbf{e}_\theta$ and $\boldsymbol{\tau}$, the latter being the unit vector tangential to the deformed profile. Consequently, we can write the pressure as:

$$p\,\mathbf{n} = p\,(-\cos\varphi\,\mathbf{e}_r + \sin\varphi\,\mathbf{e}_\theta). \tag{2.19}$$

Now, observe that, as $u_r \ll R$, $\varphi \ll 1$: this implies that $\cos\varphi \approx 1$ and $\sin\varphi \approx \partial u_r/R\partial\theta$, and $dl = ds = Rd\theta$. Then, we can write:

$$p\,\mathbf{n} = p\left(-\mathbf{e}_r + \frac{1}{R}\frac{\partial u_r}{\partial\theta}\mathbf{e}_\theta\right). \tag{2.20}$$

At this point, as sketched in Figure 2.4b, we can focus on the total load $\mathbf{F}_{tot}$ obtained as the integral of the pressure distribution. In particular, let us consider the two components along the x- and y-axes that are

$$F_x = -R \int_\Omega d\theta \, p(\theta) \left(\cos\theta + \frac{1}{R} \frac{\partial u_r}{\partial \theta} \sin\theta \right) \tag{2.21}$$

$$F_y = R \int_\Omega d\theta \, p(\theta) \left(-\sin\theta + \frac{1}{R} \frac{\partial u_r}{\partial \theta} \cos\theta \right) \tag{2.22}$$

where Ω denotes the contact domain.
Consequently, the total load is $|\mathbf{F}_{tot}| = \sqrt{F_x^2 + F_y^2}$.

Now, it is interesting also to quantify the direction of $\mathbf{F}_{tot}$ through the angle θ^* defined as

$$\theta^* = \arctan(F_y/F_x). \tag{2.23}$$

This will be referred to as attitude angle, as outlined in Figure 2.4b. Then, we can define the friction torque as:

$$\mathbf{C}_t = R \int_\Omega d\theta \, p(\theta) \frac{\partial u_r}{\partial \theta} \, \mathbf{k}, \tag{2.24}$$

where $\mathbf{k} = \mathbf{i} \wedge \mathbf{j}$, with $\mathbf{i}$ and $\mathbf{j}$ being the unit vectors of the x- and y-axis respectively. Finally, the friction circumference radius, as sketched in Figure 2.4b, is

$$R^* = |\mathbf{C}_t| / |\mathbf{F}_{tot}|. \tag{2.25}$$

2.2 Conformal contact problem

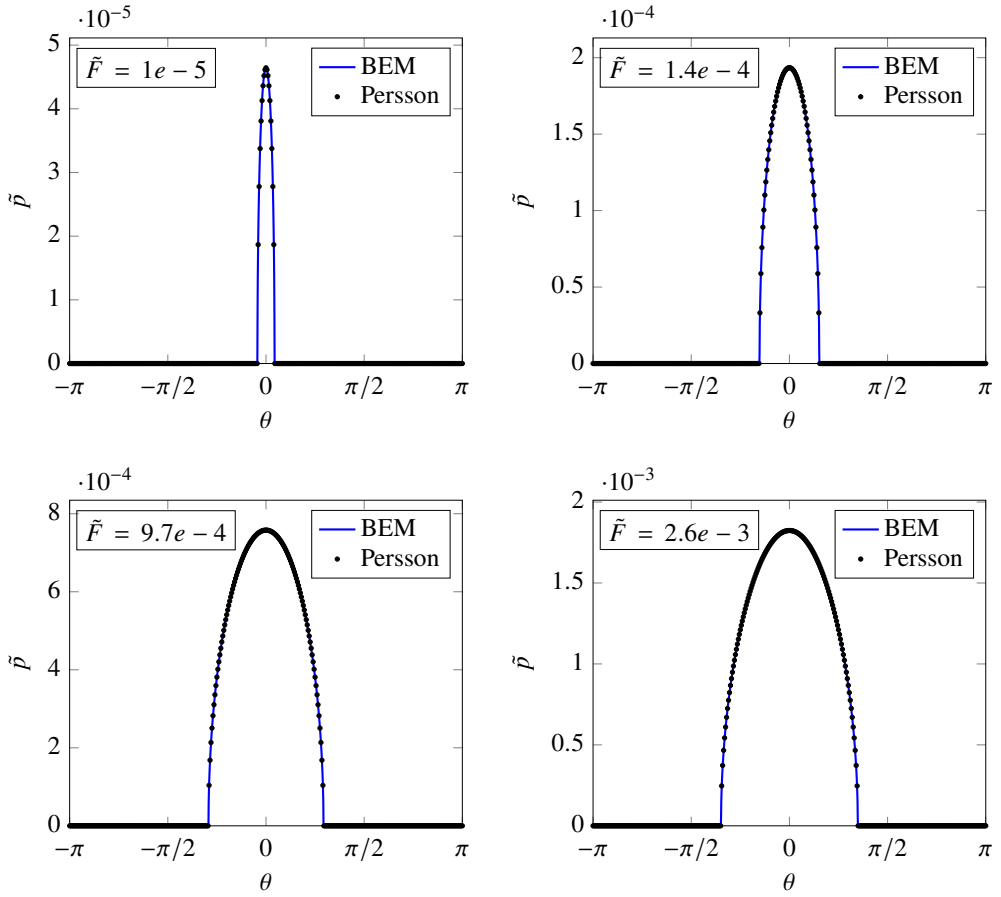

Figure 2.5: The dimensionless pressure distribution $\tilde{p} = p/E_0$ as a function of the dimensionless force $\tilde{F} = F_x/(E_0 R)$. The numerical calculations are carried out for a hole radius $R = 0.08$ m, $\Delta R = 4 \cdot 10^{-5}$ m. A very good agreement between the analytical predictions (black dots) [34] and the numerical calculations (solid line) is observed.

To show the impact and the generality of the Boundary Element formulation developed above, let us start with the paradigmatic problem of a rigid pin in conformal contact with a deformable space with a cylindrical hole. The radii of the hole and the pin are R and R' respectively. We employ a linear viscoelastic material with a glassy and a rubbery elastic modulus respectively equal to $E_\infty = 10^7$ Pa and $E_0 = 10^6$ Pa, a single relaxation time $\tau = 0.01$ s and a Poisson's ratio $\nu = 0.5$. We assume no Coulomb friction at the interface as our investigation is specifically focused on viscoelastic dissipation: the latter depends on the solution of the normal problem [22].

As a first step, the methodology is validated against the analytical solution available in Ref. [34], where A. Persson solves the contact problem for a purely elastic case when $\Delta R = R - R' \ll 1$, namely when the pin has almost the same dimension of the hole. We assume that the center of the pin is free to move along the x-axis only, while it is constrained along the y-axis.

We numerically study the case with $R = 0.08$ m, $\Delta R = 4 \cdot 10^{-5}$ m, and with an elastic modulus equal to the rubbery modulus E_0, for different values of the dimensionless load

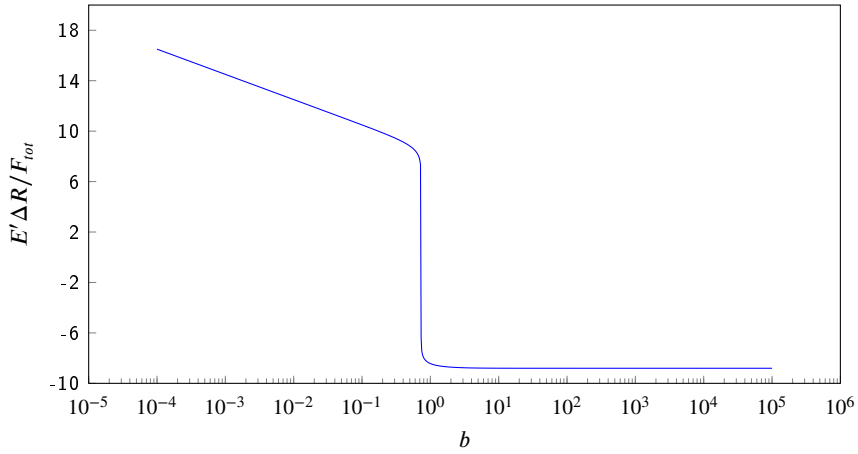

Figure 2.6: Relationship between the load parameter $E'\Delta R/F_{tot}$ as function of the parameter $b = \tan(\alpha/2)$, with α being the semi-angle of contact.

$\tilde{F} = F_x/(E_0 R)$. In Figure 2.5, numerical outcomes and analytical predictions are compared in terms of pressure distribution $\tilde{p} = p/E_0$: the agreement is really good and the error is always smaller than 0.1%. Incidentally, let us recall that, for this kind of problem, when the load is very small, the Hertzian limit is approached; on the other hand, for increasing values of the load, the contact area grows until a limiting arc of contact is reached [34]. Specifically, for the geometry under investigation, the limit contact angle is θ_c=1.24 and is reached for a load $\tilde{F} = 2.3 \cdot 10^{-2}$; for larger loads, the contact area cannot grow, namely complete contact occurs. This is shown in Figure 2.6, where the load parameter $E'\Delta R/F_{tot}$, with E' being the equivalent Young's modulus, is plotted against the parameter b, defined as $b = \tan(\alpha/2)$, α being the semi-angle of contact. In particular, it can be observed that, as soon as we increase the load from very small values, the problem is linear until a limiting condition is reached, namely the neat-fit condition $E'\Delta R/F_{tot} = 0$, where the curve presents a vertical line corresponding to a certain limiting angle θ_c; for larger loads full contact occurs [35]. Notice that at infinite loads the neat-fit condition is again retrieved.

Now, we can focus on the conformal contact of a rigid pin rotating, at a constant speed ω, in a cylindrical hole on a viscoelastic space: the radii R and R' are respectively equal to $R = 0.08$ m and $R' = 0.075$ m. Figure 2.7 shows the results of the numerical simulation, in terms of pressure and displacement distributions. Also, calculations have been performed for a force acting along the x-direction with a dimensionless value of $\tilde{F} = 3.5 \cdot 10^{-2}$, and increasing values of the dimensionless rotational speed $\tilde{\omega}$. On the right column, we report the pressure distribution, the deformed surface, and the equivalent indenting profile. In detail, for a stationary contact, i.e., for $\tilde{\omega} = 0$, we observe, for the pressure, a Hertzian-like trend, but, as soon as $\tilde{\omega}$ is increased, a peak appears at the leading edge with the distribution becoming more and more asymmetric. Correspondingly, at the trailing edge, we observe larger displacement values, where the material is deformed upon the pin passage and is relaxing and thus a shrinking contact region. At very high speeds, a new elastic (glassy) regime is reached: as we are keeping constant the normal force, the contact area reduces and smaller displacements are found.

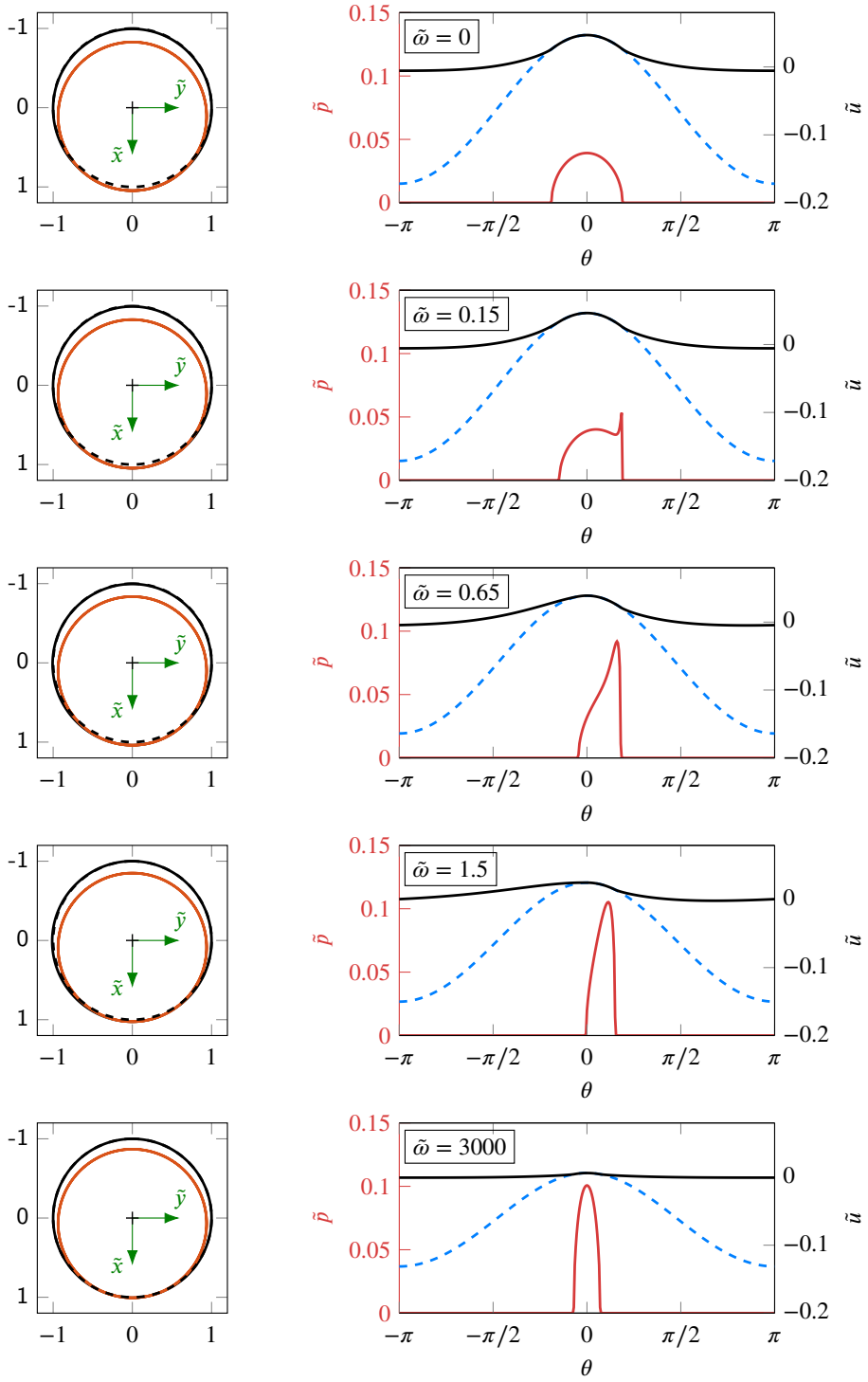

Figure 2.7: The undeformed (dashed black line) and the deformed (solid black line) contour of the hole in contact with the pin (solid orange line) on the left; the deformed contour (solid black line), the dimensionless pressure distribution $\tilde{p} = p/E_0$ (solid red line) and the indentation profile (dashed blue line) on the right. The axes $\tilde{x}$ and $\tilde{y}$, on the left, refer to the normalized x- and y-coordinates, i.e., $\tilde{x} = x/R$ and $\tilde{y} = y/R$.

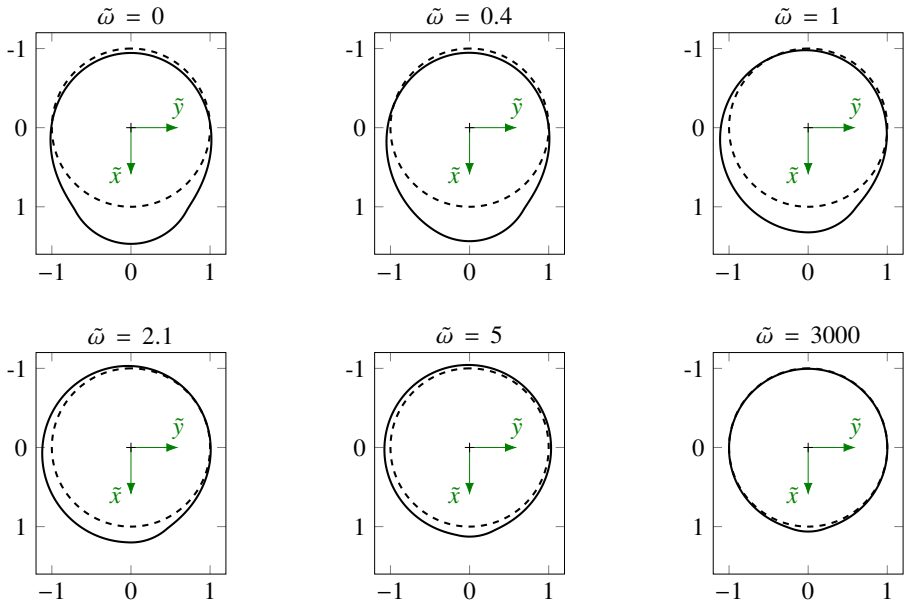

Figure 2.8: The undeformed (dashed black line) and the magnified deformed contour of the hole (solid black line), with $K = 10$ being the magnification factor, for a viscoelastic material with a single relaxation time $\tau = 0.01$ s, glassy modulus equal to $E_\infty = 10^7$ Pa, $E_\infty/E_0 = 10$, and Poisson's ratio $\nu = 0.5$. Results are carried out for different values of the dimensionless speed $\tilde{\omega} = \omega\tau$ and fixed dimensionless force $\tilde{F} = F_x/(E_0 R) = 3.5{\cdot}10^{-2}$. The axes $\tilde{x}$ and $\tilde{y}$ refer to the normalized x- and y-coordinates, i.e., $\tilde{x} = x/R$ and $\tilde{y} = y/R$.

All this is qualitatively consistent with what was observed for plane systems in non-conformal contacts [24], but, for the first time, it is found in a conformal contact viscoelastic problem. The latter has its peculiarities including, as previously mentioned, a limit for the contact area and a finite value for the mean displacement of the deformed surface. This last aspect is particularly interesting. In fact, on the left column in Figure 2.7, we can observe the absolute position of the pin in contact with the deformable viscoelastic counterpart.

From an applicative point of view, this may be crucial in multiple contacts, as occurs, for example, in needle roller bearings: in this case, although the contact of each rolling element with the rings can be considered non-conformal, a sort of conformal-like effect should be observed, due to the finiteness and the circular geometry of the system, and to the contact interaction between each roller. This allows us to determine how the load is distributed among the different rollers [67], and is widely investigated in Section 2.3.

Looking more in detail at the magnified shape of the deformed system at different velocities $\tilde{\omega}$ in Figure 2.8, we observe a strongly non-symmetrical shape about the x-axis. Indeed, in addition to a general shift of the deformed profile due to the finite mean deformation previously discussed, a larger deformation is found at the trailing edge of the contact region: this is related to the system viscoelasticity and to the different relaxation between leading and trailing edges.

As depicted in Figure 2.9, there are, then, consequences on the pressure distribution, which becomes asymmetric, and, crucially, on the resultant force $\mathbf{F}_{tot}$ of the pressure distribution at the interface between the pin and the hole. $\mathbf{F}_{tot}$ presents, besides the x-component that equilibrates the externally applied load, a y-component, which originates

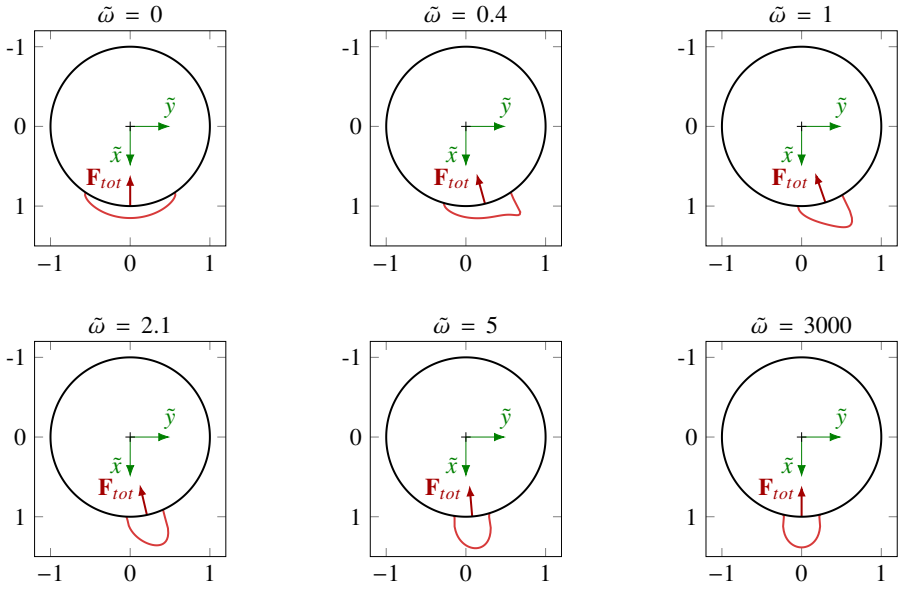

Figure 2.9: The pressure distribution on the contact area (red line) and the resulting net force $\mathbf{F}_{tot}$ at different dimensionless speeds $\tilde{\omega}$ and fixed dimensionless force $\tilde{F} = F_x/(E_0 R) = 3.5 \cdot 10^{-2}$. The axes $\tilde{x}$ and $\tilde{y}$ refer to the normalized x- and y-coordinates, i.e., $\tilde{x} = x/R$ and $\tilde{y} = y/R$.

as a consequence of the viscoelastic hysteretic behavior of the material. Note that we are dealing with a frictionless interface and, so, no tangential surface stresses due to Coulomb friction are present at the contact interface, but, due to the viscoelastic dissipation occurring in the material, the pressure distribution becomes asymmetric, so that the resultant force $\mathbf{F}_{tot}$ of the pressure distribution generates a resistant torque about the center of the pin. Indeed, $\mathbf{F}_{tot}$ is tangent to the so-called friction circumference. In Figure 2.10, we plot the torque $\tilde{C} = |\mathbf{C}_t|/F_x R$, the trigonometric tangent of the attitude angle θ^* and the radius $\tilde{R}$. These quantities are, clearly, all related to the viscoelastic dissipation: indeed, for very small and very large velocities, where the material behaves elastically, they tend to zero, whereas, for intermediate values of the speed, they reach a maximum.

Ultimately, it has been shown that the numerical methodology is able to provide a complete contact solution in terms of stress, strain, and friction. It has to be pointed out that the Boundary Element formulation has, crucially, no limitation in terms of material properties- it can be applied to any linear viscoelastic material- and geometry. This is an interesting aspect as, in the deformable ring, multiple contacts at different scales, ranging from the macro-scale down to the roughness can be managed [76]: this unique feature is reached thanks to the intrinsic computational efficiency of Boundary Element approaches which discretize just the boundary of the problem domain.

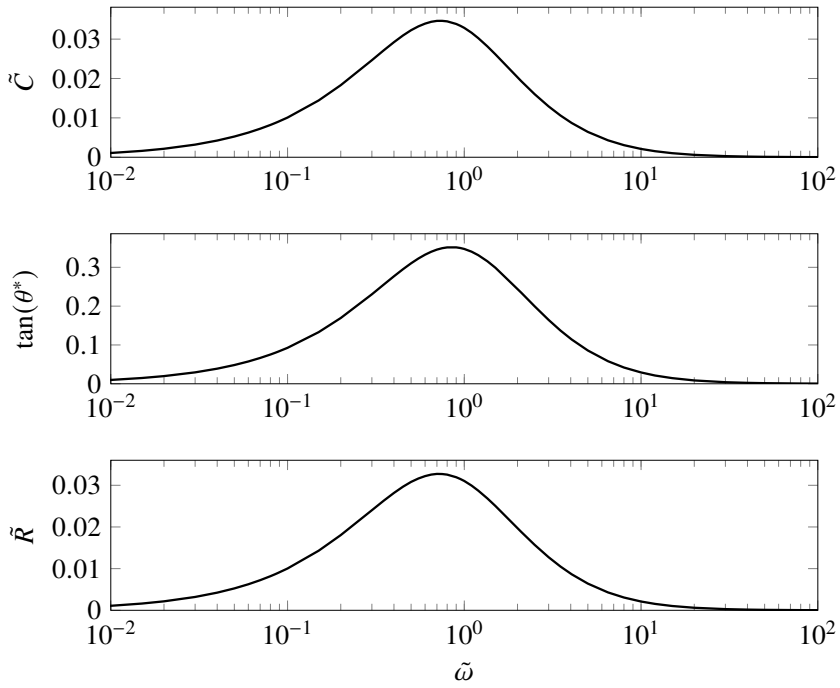

Figure 2.10: Friction torque due to viscoelastic rolling contact $\tilde{C} = |\mathbf{C}_t|/F_x R$, the attitude angle θ^* and the dimensionless friction circumference radius $\tilde{R} = R^*/R$ as a function of the dimensionless speed $\tilde{\omega} = \omega\tau$.

2.3 Multiple contact problem: rolling element bearing

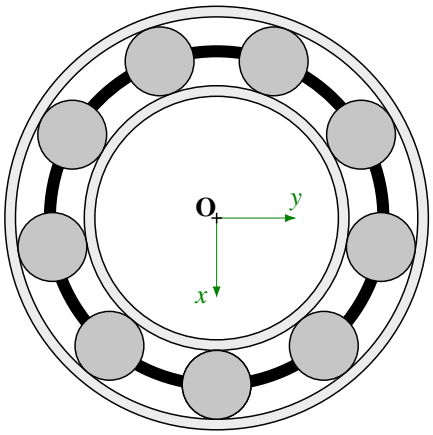

Figure 2.11: Schematic of the rolling element bearing.

The BE methodology presented in Section 2.1 is not only limited to single contacts but, crucially, it blazes the trail to further studies in multiple contact applications. Indeed, in this Section, we focus our attention on a component of crucial importance in mechanical engineering, that is, the rolling element bearing. Referring to Figure 2.11, we consider a structure where the two rings, i.e., the inner one and the outer one, are linearly viscoelastic, while the rolling elements, assumed as needles, are rigid. Let us notice that, beyond the importance of the application, this problem has a strong

theoretical interest as it refers to a circular multiple contacts configuration: indeed, each contact patch interacts with the others in the circular domain. Incidentally, this is of utmost importance in many problems in biomechanics: the hip joint [30] and all the prostheses [31] are just possible examples. Coming back to the rolling element bearing case, one of the most important functional aspects to monitor is the load distribution on the rolling elements as it determines the number of active rolling elements where the external load is applied. A large number of researchers have tried to address this problem, starting from the pioneering research contribution by Stribeck in Ref. [77]: he investigated the case of a ball bearing with zero radial clearance and subjected to an external radial load directed as one of the rolling elements and, later, extended this solution to the case of a ball bearing with a nominal radial clearance. Other significant contributions to tackle the problem have been provided by Harris [78]: moving from the studies of Sjovall [79], he introduced a load distribution factor, thus developing a 2D model of an elastically-deformable rolling element bearing. Later, in Ref. [80], Lazovic presented a mathematical model of the load distribution among the rolling elements by taking into account the influence of the internal radial clearance and the shape of the races. Another considerable contribution has been recently provided by Tomovic [81,82], who developed a mathematical model to assess the external radial load necessary for a roller to take part to the contact. Despite this broad and well-consolidated research in the field, a clear understanding of the role played by viscoelasticity in this scenario is still missing, but, at the same time, is getting crucial given the increasing diffusion of polymer bearings.

Therefore, the goal is to understand how viscoelastic rheology intervenes in determining the mechanics of the rolling element bearing in terms of load distribution among the rolling elements and of the overall viscoelastic hysteresis. To this aim, a numerical analysis relying on the mathematical formulation presented in Section 2.1 for conformal and non-conformal circular contacts is implemented, and *ad-hoc* Green's functions for both the inner ring-roller and outer ring-roller contacts have been introduced. Crucially, these Green's functions intrinsically account for the circular hallmark of the contact domain. On this basis, here an efficient Boundary Element methodology to numerically solve the contact problem in a rolling element bearing is developed.

2.3.1 Problem formulation

Let us consider the multiple contact problem characterizing a rolling element bearing, where the rolling elements are rigid and the rings are deformable and viscoelastic. Incidentally, let us observe that great efforts have been spent to determine how the bearing load is distributed among the rollers [67,78,81,82]: to solve this problem, load-deflection relationships for the rolling elements in contact with the raceways have been developed, but these analyses have been conducted only for a purely elastic case. As mentioned before, due to the wide use of polymers in the industry, the aim of this study is to fill the gap in the field, considering linearly viscoelastic raceways. In particular, we consider the steady-state rotation of the inner and the outer ring, with the rotational speeds sufficiently small to avoid roller centrifugal forces or gyroscopic moments of significant magnitudes: these effects are, thus, neglected.

Focusing on the geometry under analysis, as sketched in Figure 2.12a, the total approach δ_r along the loading direction between the two raceways in contact with the interposed rolling element can be seen as the sum of the penetration between the rolling

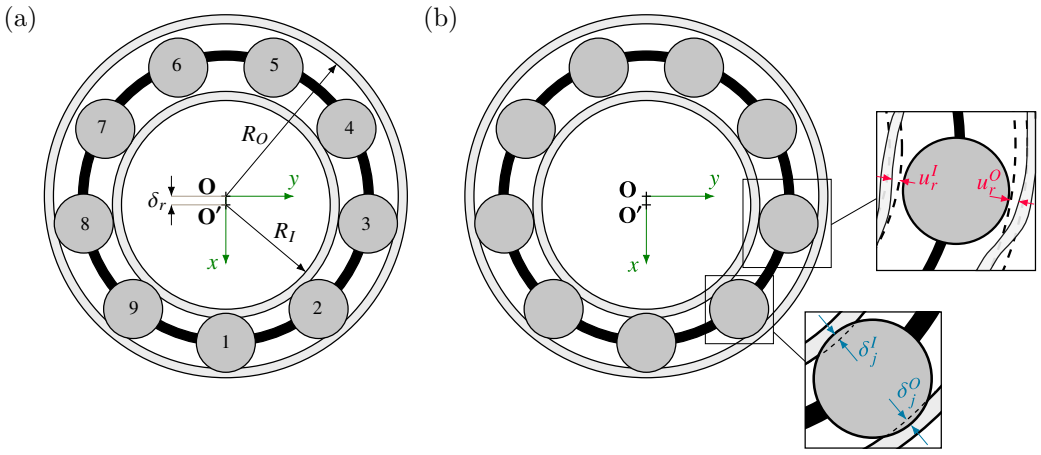

Figure 2.12: Schematic of the rolling element bearing with the indication of the total radial approach between the raceways δ_r (a); the relative radial approaches between the j-th rolling element and the inner and outer raceways, respectively δ_j^I and δ_j^O, and the radial deflection of the rings, $\mathbf{u}_r^I$ and $\mathbf{u}_r^O$.

element and each ring, i.e., $\delta_r = \delta_O + \delta_I$, where the subscripts O and I refer to outer- and inner-raceway respectively. Furthermore, for a rigidly supported bearing subject to radial load, the total radial deflection at any rolling element angular position, that is $\delta_j = \delta(\psi_j)$, has been presented in Ref. [67, 78]:

$$\delta_j = \delta_r \cos\psi_j - \frac{1}{2} P_d, \tag{2.26}$$

in which δ_r is the ring radial shift, which, under the assumption of perfectly vertical load, occurs at $\psi = 0$, ψ_j is the angular position of the j-th rolling element, and P_d is the diametral clearance, that is equal to $P_d = 2(R_O - R_I - D_r)$, with R_O and R_I being the radii of the outer and inner ring respectively, and D_r is the diameter of the rolling elements. This definition in Equation (2.26) perfectly fits the system under analysis, that is, a rolling element bearing with deformable rings and rigid rollers, as shown in Figure 2.12a, and in details in Figure 2.12b. According to the reference frame adopted, $\psi = 0$ corresponds to the angular position of rolling element 1; the other rollers are, then, numbered according to the schematic in Figure 2.12a.

Now, to correctly define the contact problems and determine how the bearing load is distributed among the rollers, we have to define the pressure distribution. To this aim, we move from the mathematical formulation presented Section 2.1, where a fully general approach to deal with steady-state viscoelastic circular contact problems has been developed: this relies on the definition of *ad-hoc* Green's functions, capturing the nature of the circular contact domain. Moving from this, to approach the problem under investigation, let us observe that we can distinguish two different contact conditions: one refers to the contact between the outer raceway and the rollers, and the other to the inner ring and, again, the rollers. In the first case, each roller acts as a rigid cylindrical punch placed inside a circular hole within an infinite viscoelastic space; in the second one, the rigid punch is in contact with a viscoelastic cylinder. As sketched in Figure 2.13a and 2.13b, and commented later in detail, the two cases will lead to completely different contact boundary conditions.

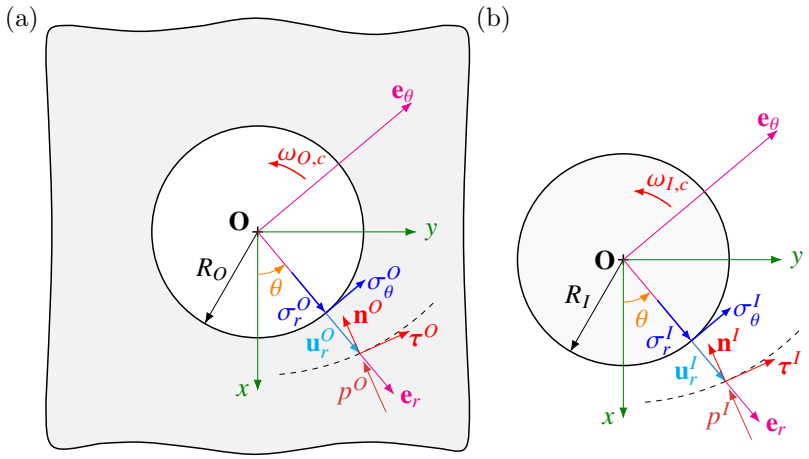

Figure 2.13: Schematic of the outer ring radial displacement $\mathbf{u}_r^O$, the pressure p^O directed along the unit vector $\mathbf{n}^O$, normal to the deformed profile(dashed line), for the outer ring-roller contact, modeled as a cylindrical hole drilled throughout a viscoelastic infinite space, subject to an isolated load on the boundary (a); schematic of the inner ring radial displacement $\mathbf{u}_r^I$, the pressure p^I directed along the unit vector $\mathbf{n}^I$, normal to the deformed profile(dashed line), for the inner ring-roller contact modeled as an infinite viscoelastic cylinder, fixed at the center $\mathbf{O}$, subject to an isolated load on the boundary (b).

For the time being, let us focus on the common boundary element formulation which can be employed for the two cases. First of all, the bearing is studied as two-dimensional, as we assume plane strain conditions. Then, by recognizing that the system is rotationally invariant, and recalling the elastic-viscoelastic correspondence principle, in the system in Figure 2.13, following the mathematical formulation presented in Section 2.1, we can relate, for both the two different circular contact problems, the total displacement $\mathbf{u}$ and the stress $\boldsymbol{\sigma}$, respectively defined in a polar reference frame as $\mathbf{u} = u_r\mathbf{e}_r + u_\theta\mathbf{e}_\theta$ and $\boldsymbol{\sigma} = \sigma_r\mathbf{e}_r + \sigma_\theta\mathbf{e}_\theta$ through the following integral equation:

$$\mathbf{u}(s,t) = \int_{-\infty}^{t} dt' \int_0^{2\pi R} ds'\, J(t-t')\mathbf{G}(s-s')\dot{\boldsymbol{\sigma}}(s',t'), \tag{2.27}$$

where $s = R\theta$ and $s' = R\theta'$, R being the characteristic radius of the contact domain, t is the time and, most importantly, $\mathbf{G}(s)$ is the spatial Green's tensor. Again, as the characteristic velocity of the phenomenon is negligible with respect to the wave propagation speed, inertial effects have no relevance in the present analysis and, thus, are neglected in Equation (2.27).

Now, by moving from the complex potentials theory (see Appendix A for more details), we can particularize Equation (2.27) for the two contact cases previously described. In particular, looking at the contact problem involving the outer ring and the rollers, all the different components of the Green's tensor have been calculated in the Appendix A.2. These are now presented for the contact occurring at the inner ring (see Appendix A.3 for the complete derivation). Given the aim of the present investigation, that is, to assess the normal contact problem to determine the pressure distribution on each roller, the tangential stresses σ_θ are neglected, and the attention is particularly focused just on

the radial displacement u_r at the interface, thus recalling Equation (2.6), we have:

$$u_r(s,t) = \int_{-\infty}^{t} dt' \int_0^{2\pi R} ds'\, J(t-t') G_{rr}(s-s') \dot{\sigma}_r(s',t'), \tag{2.28}$$

where G_{rr} is the purely radial term displacement due to a normal stress σ_r equal to a Dirac delta load, i.e., $\sigma_r = \delta(s)$.

Now, recalling linearity and rotational invariance, together with the assumption that the stress distribution at the interface is a Dirac-delta distribution moving at a constant angular speed, that is, $\sigma_r(s,t) = \delta(s - \omega R t)$, it is possible to rewrite Equation (2.28) in the following steady-state form:

$$u_r(S) = \int_0^{2\pi R} dS'\, \mathcal{G}_{rr}(S-S',\omega)\, \sigma_r(S'). \tag{2.29}$$

$\mathcal{G}_{rr}(S)$ is the viscoelastic steady-state Green's function, whose expression is given by Equation (2.14).

Now, it is crucial to particularize this integral formulation in Equation (2.29) to each of the two contact problems involved in our analysis. First of all, let us specify the angular velocity ω. Specifically, we recall that, from a kinematic point of view, the rolling elements are driven by the cage, which is rotating at constant angular speed ω_c around the origin of the fixed reference frame, shown in Figure 2.11 and coincident with the geometric center of the bearing. In particular, being ω_I and ω_O the angular velocities of the inner ring and the outer ring, ω_c is equal to $\omega_c = (\omega_I R_I + \omega_O R_O)/(R_I + R_O)$. Consequently, the contact patch at the outer raceway moves with a constant angular speed equal to $\omega_{O,c} = \omega_O - \omega_c$, while for the inner raceway, we have that $\omega_{I,c} = \omega_I - \omega_c$.

Hence, we can particularize Equation (2.29) for the outer raceway contact as:

$$u_r^O(S) = \int_0^{2\pi R_O} dS'\, \mathcal{G}_{rr}^O(S-S',\omega_{O,c})\, \sigma_r^O(S') \tag{2.30}$$

where $\mathcal{G}_{rr}^O$ can be found by setting in Equation (2.14) G_{rr} as:

$$G_{rr}^O(s) = \frac{1+\nu}{2\pi}\left[-\frac{\kappa}{\kappa+1}(2\log R_O + 1)\cos\theta - \frac{\kappa+1}{2}\mathrm{B}(\theta)\cos\theta + (\kappa-1)\mathrm{A}(\theta)\sin\theta\right], \tag{2.31}$$

where $\theta = s/R_O$ is the angle subtended by the arc s and, as presented in Appendix A.2, the terms $\mathrm{A}(\theta)$ and $\mathrm{B}(\theta)$ are equal to $\mathrm{A}(\theta) = \arg(1/2 - i/2\cot(\theta/2))$ and $\mathrm{B}(\theta) = \log(2 - 2\cos\theta) = 2\log(2|\sin(\theta/2)|)$.

On the other hand, for the inner raceway interface, the contact problem can be described by the following integral equation:

$$u_r^I(S) = \int_0^{2\pi R_I} dS'\, \mathcal{G}_{rr}^I(S-S',\omega_{I,c})\, \sigma_r^I(S') \tag{2.32}$$

where $\mathcal{G}_{rr}^I$ can be found by setting G_{rr} in Equation (2.14) as

$$G_{rr}^I(s) = \frac{1+\nu}{2\pi}\left[\frac{1-(\kappa^2+1)\log R_I}{\kappa+1}\cos\phi - \cos\phi - \frac{\kappa+1}{2}(\kappa-1)\mathrm{A}'(\phi)\sin\phi - \frac{\kappa+1}{2}\mathrm{B}(\phi)\cos\phi\right], \tag{2.33}$$

where $\phi = s/R_I$ is the angle subtended by the arc s previously defined, and $\mathrm{A}'(\theta) = \arg(-1/2 - i/2\,\cot(\theta/2))$ (see Figure 2.13b).

Once the Green's functions are defined, we adopt the numerical scheme proposed in Section 2.1 to numerically assess the circular contact problem. Specifically, we discretize the contact domain with N elements, each covering an arc of length $2\alpha R$, with R being the characteristic radius of the paradigmatic circular contact domain; with the assumption that the discretization step is small enough on an arc $[S_k - \alpha R, S_k + \alpha R]$, S_k being the angular position of the center of the k-th interval, we can consider the stress constant and equal to $\sigma_k = \sigma_r(S_k)$, and write the radial displacement $u_i = u_r(S_i)$ at the center of the i-th interval as follows:

$$u_i = \sum_{k=1}^{N} \sigma_k \int_{S_k-\alpha R}^{S_k+\alpha R} dS' \, \mathcal{G}_{rr}(S_i - S', \omega), \tag{2.34}$$

where $\mathcal{G}_{rr}$ is the corresponding viscoelastic Green's function in the two cases. Then, Equation (2.34) can be further developed by using the definition of the function L_{rr} (see Equation (2.17)), that is $L_{rr}(S) = \int_0^{2\pi R} dS' \, G_{rr}(S - S')\chi_r(S')$, with χ_r being a pressure unitary in the arc $[-\alpha R, \alpha R]$ and vanishing outside. Hence, with reference to Equation (2.16), $\mathcal{L}_{rr}(S)$ is equal to:

$$\mathcal{L}_{rr}(S) = J(0)L_{rr}(S) + \int_0^{+\infty} d\tau \, C(\tau) \int_0^{2\pi/\omega\tau} dz \; e^{-z} \, L_{rr}(S + \omega R \tau z). \tag{2.35}$$

The definition of $\mathcal{L}_{rr}$ leads us to rephrase Equation (2.30) and (2.32) as the following linear systems [22, 73, 75]:

$$\{u_i^O\} = [\mathcal{L}_{ik}^O(\omega)]\{\sigma_k^O\} \tag{2.36a}$$
$$\{u_i^I\} = [\mathcal{L}_{ik}^I(\omega)]\{\sigma_k^I\} \tag{2.36b}$$

where the indexes I and O refer to the inner and the outer ring respectively; moreover, the intercorrelation matrix elements $\mathcal{L}_{ik}$ are defined as $\mathcal{L}_{ik} = \mathcal{L}_{rr}(S_i - S_k, \omega)$.

Each contact problem can be solved by means of the numerical scheme proposed in Ref. [83]: given the penetration of each rigid punch in the deformable solid, we can immediately calculate the displacement distribution in the contact area and, then, by inverting the relation (2.36), determine the stress distribution σ_k^O and σ_k^I. Clearly, as in each problem the contact area is not known a priori, we implement an iterative procedure, where, at each step, the elements with negative pressure are removed, and those for which there occurs numerical compenetration, are added [84].

However, a relevant piece of information is still missing. In fact, once the total penetration δ_r is properly tuned to set the total load supported by the bearing, thanks to Equation (2.26), we understand how δ_r applies to each rolling element, but, for the general j-th rolling element, the relative approaches between this rigid element at the angular position ψ_j and the raceways are unknown. These quantities can be defined, respectively for the outer and the inner ring, as δ_j^O and δ_j^I, and they are clearly related to δ_j:

$$\delta_j = \delta_j^I + \delta_j^O \tag{2.37}$$

Determining the set of penetration values for the inner ring and the outer one, i.e., δ_j^I and δ_j^O, is essential to solve the contact problems. This can be done by imposing the force balance on each roller. Neglecting second-order terms, we focus on the radial equilibrium: the radial force component on each roller, interacting on the j-th contact patch Ω_j^I with

the inner ring, i.e., $F^I_{r,j} = R_I \int_{\Omega^I_j} d\theta \sigma^I_r(\theta)$, is assumed equal to that one in contact with the outer ring, i.e., $F^O_{r,j} = R_O \int_{\Omega^O_j} d\theta \sigma^O_r(\theta)$. Interestingly, we have checked, *a posteriori*, that the tangential force component is negligible compared to the radial one: thus, the approximation made is well-posed. Furthermore, let us notice that, without any loss of generality, we have assumed the rotational speeds are small enough to neglect gyroscopic moments and centrifugal forces; however, should this assumption become inconsistent with the application conditions, it is straightforward to include these components in the radial balance. Finally, we assume that the interaction forces between the cage and the rolling elements are supposed to be much smaller than the contact forces: thus, these are not accounted for in this analysis. Thanks to the closing condition on the radial balance of each roller, it is possible to find the contact solution and determine the stresses on each roller. It should be noted that a final iteration will be done on δ_r to ensure that the total load applied to the bearing is transmitted.

Understanding how the global load distributes among the different rollers is one of the aims of our analysis. To this extent, it should be noted that a local load can be transmitted through a rolling element only when the rings are effectively in contact with the roller and, thus, the radial clearance at the given angular position is filled. Hence, we can introduce the gap $g(\psi) = u^O_r(\psi) - u^I_r(\psi) - \delta(\psi)$, with u^O_r and u^I_r being the corresponding radial displacements of the outer and inner raceway respectively, as depicted in Figure 2.12, and $\delta(\psi)$ is the total radial deflection, defined in Equation (2.26). A roller can transmit load only if, at any point, the gap is equal to zero.

The other crucial focus of the present analysis is related to the viscoelastic contribution to friction. In particular, similarly to what is presented in Section 2.1, we assume that the Coulomb friction is negligible. We can find the net forces, per unit length, acting on each ring, $\mathbf{F}_{tot} = \mathbf{F}_x + \mathbf{F}_y$, where $\mathbf{F}_x = F_x\,\mathbf{i}$ and $\mathbf{F}_y = F_y\,\mathbf{j}$ are the components along the x- and y-axes respectively, with $\mathbf{i}$ and $\mathbf{j}$ being the corresponding unit vectors. Specifically, we can write:

$$F_x = R \int_0^{2\pi} d\theta\, p(\theta)\mathbf{n}(\theta) \cdot \mathbf{i}, \tag{2.38}$$

and

$$F_y = R \int_0^{2\pi} d\theta\, p(\theta)\mathbf{n}(\theta) \cdot \mathbf{j}, \tag{2.39}$$

where R is equal to R_O and R_I respectively for the outer and the inner ring, and p is the pressure acting on each ring. In detail, as reported in Figure 2.13, the pressure on the inner ring p^I is equal to $|\sigma^I_r|$ and is directed along the unit vector $\mathbf{n}^I$, that is normal to the deformed cylinder; on the other hand, the pressure on the outer ring p^O, being equal to $|\sigma^O_r|$, is directed along the unit vector $\mathbf{n}^O$, that is normal to the deformed hole (see Figure 2.13).

Now, we can compute the friction torque as:

$$\mathbf{C}_t = R \int_0^{2\pi} d\theta\, (\mathbf{P}(\theta) - \mathbf{O}) \wedge p(\theta)\mathbf{n}(\theta), \tag{2.40}$$

where $\mathbf{P}(\theta)$ is the point of the deformed profile at angular coordinate θ, and $\mathbf{O}$ is the center of the bearing, coincident with the origin of the fixed reference frame adopted, as shown beforehand. Finally, it is interesting to quantify the radius of the friction circumference as $R^* = |\mathbf{C}_t|/|\mathbf{F}_{tot}|$, and the direction of the net force $\mathbf{F}_{tot}$ with respect to the radial direction through the so-called friction angle $\varphi^* = \arccos(F_r/F_{tot})$, with F_r being its radial projection.

2.3.2 Single relaxation time materials: results and discussion

In order to point out the main capabilities of the Boundary Element methodology developed, we focus on a rolling element bearing with rigid needle rollers and deformable linearly viscoelastic rings characterized by a single relaxation time $\tau = 0.01$ s, a rubbery elastic modulus, i.e., the low-frequency modulus, $E_0 = 10^6$ Pa, and the glassy elastic modulus, i.e., the high-frequency modulus, $E_\infty = 10^7$ Pa, and a Poisson's ratio $\nu = 0.5$. With regards to the bearing geometry, we consider a rolling element bearing, in which the outer raceway has a radius equal to $R_O = 6$ mm, the inner ring has radius $R_I = 4$ mm, and rolling elements with diameter $D_r = 2$ mm. Hence, the diametral clearance P_d is $P_d = 0$ mm and, consequently, the angular extent of the load zone is equal to $\psi_l = \pi/2$, as shown in [67, 78].

Since the main angle is to investigate the viscoelastic contribution to friction, the interface is assumed to be frictionless, thus assuming that the Coulomb friction is negligible. Then, numerical calculations have been performed for a constant force acting along the $x-$direction with a dimensionless value being equal to $\tilde{F} = F_x/E_0R_O = 6.5 \cdot 10^{-3}$, and increasing values of the shaft speed ω_I, while the outer ring is considered fixed, i.e. $\omega_O = 0$. Hence, the relative speeds at the inner raceway contact $\omega_{I,c}$ and outer raceway contact $\omega_{O,c}$ are equal to $\omega_{I,c} = \omega_I - \omega_c$ and $\omega_{O,c} = -\omega_c$, with $\omega_c = \omega_I R_I/(R_I + R_O)$ being the angular velocity at which the cage is rotating with respect to the center of the bearing **O**.

Figure 2.14 presents, as a function of the dimensionless speed $\tilde{\omega} = \omega_{O,c}\tau$, a set of dimensionless quantities, related to local displacements and forces, for each of the rolling elements in the loaded zone, that is, $-\psi_l \leq \psi \leq \psi_l$. First of all, we plot the dimensionless total radial deflection $\tilde{\delta}_j = \delta_j/R_O$, which is the sum of the relative radial approaches between the rings and the rollers, the latter found by means of an iterative technique, as explained in Section 2.1. Such a methodology allows us to find the complete contact solution and, *inter alia*, also the radial displacement distribution of the rings, being respectively equal to $u_r^O(\psi)$ and $u_r^I(\psi)$. If we define with ψ_j the angular position of the j-th roller, that is the position of its centroid, we can introduce and plot, again in Figure 2.14, the dimensionless displacements $\tilde{u}_j^O = u_r^O(\psi_j)/R_O$ and $\tilde{u}_j^I = u_r^I(\psi_j)/R_O$: interestingly, when the j-th rolling element is in contact, $\tilde{u}_j^O$ and $\tilde{u}_j^I$ coincide with the dimensionless penetration $\tilde{\delta}_j^O = \delta_j^O/R_O$ and $\tilde{\delta}_j^I = \delta_j^I/R_O$, while are still well defined in non-contact cases. The latter are monitored by means of the gap $\tilde{g}_j = g\left(\psi_j\right)/R_O$: when this is different from zero, contact conditions are lost. Finally, we plot also the local radial load $\tilde{F}_{r,j} = F_{r,j}/E_0R_O$ applied to each roller by the internal and the external ring.

Coming to the analysis of the results in Figure 2.14, let us start observing that, for all the rollers, given the global constant load $\tilde{F}$, the total radial deflection $\tilde{\delta}_j$ obeys to a sigmoidal trend, due the stiffening of the viscoelastic material with the speed. Let us observe that, at very low speeds, the material behaves as an elastic soft solid, while at very high speeds, where the material resembles a stiff elastic solid, the penetration strongly decreases. For the other quantities, a more intricate behavior is observed. In fact, we notice that, in a certain speed interval, the rolling elements 3 and 8 lose the contact with the rings as the local forces $\tilde{F}_{r,3}$ and $\tilde{F}_{r,8}$ vanish, and the gap $\tilde{g}_3$ and $\tilde{g}_8$ gets different from zero. Correspondingly, the displacements $\tilde{u}_j^O$ and $\tilde{u}_j^I$ have not a monotonic trend. From a mechanical point of view, contact is lost due to viscoelasticity-induced deflections of the rings and, consequently, to the viscoelasticity-induced radial clearance g between the rollers and the raceways: indeed, as we will notice later when observing in

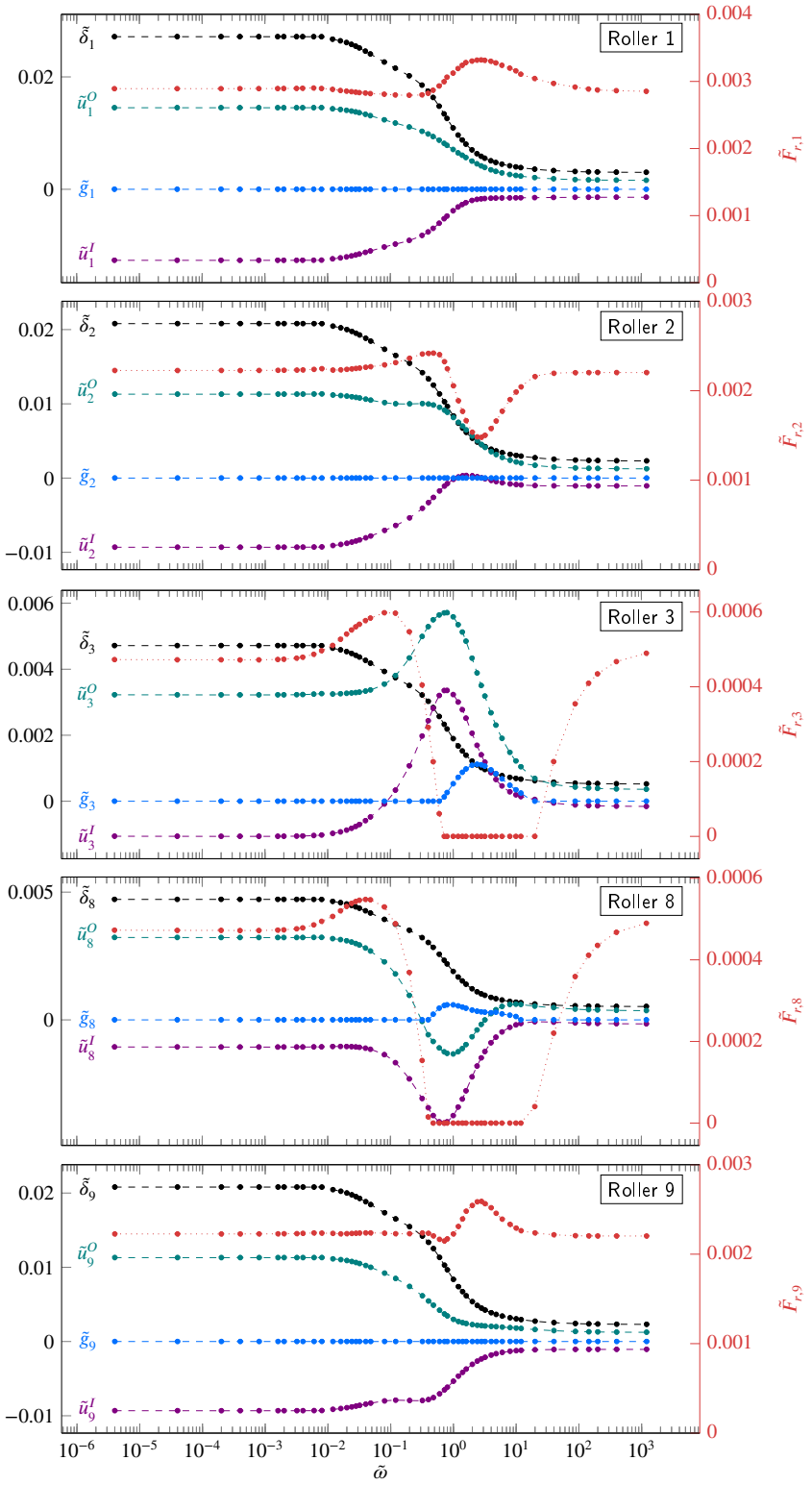

Figure 2.14: On the left y-axis, the dimensionless total radial deflection at angular position ψ_j, occupied by the j-th rolling element, $\tilde{\delta}_j = \delta_j/R_O$, the dimensionless outer- and inner-raceway deflections, respectively $\tilde{u}_j^O = u_r^O(\psi_j)/R_O$ and $\tilde{u}_j^I = u_r^I(\psi_j)/R_O$, and the dimensionless radial clearance $\tilde{g}_j = g(\psi_j)/R_O$. On the right y-axis, the dimensionless radial component of the resultant force, that is, $\tilde{F}_{r,j} = F_{r,j}/E_0 R_O$ for the j-th rolling element. The numerical results are carried out at a fixed value of the dimensionless force $\tilde{F} = 6.5 \cdot 10^{-3}$ at different dimensionless speed $\tilde{\omega}$.

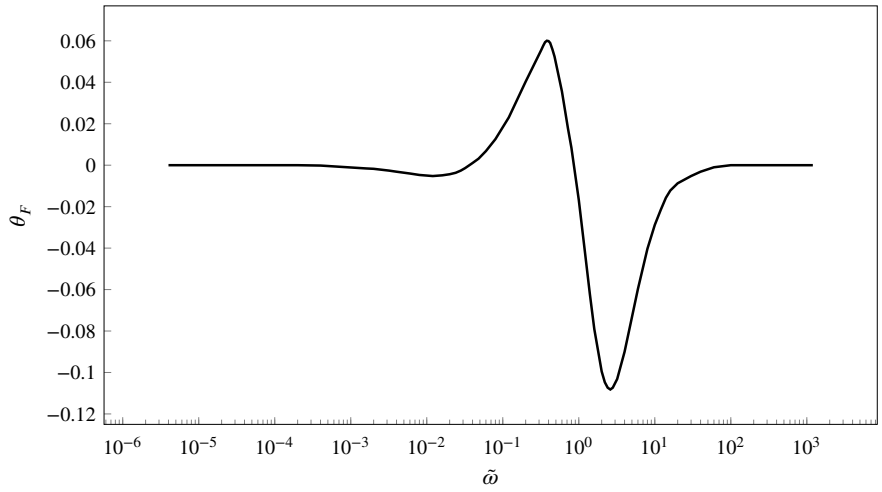

Figure 2.15: The angular position θ_F of the net force $\mathbf{F}_{tot}^{O}$ as a function of the dimensionless speed $\tilde{\omega}$.

detail the deformed rings, this is due to the delay intrinsically introduced when dealing with a viscoelastic process [23].

For the time being, let us focus on the local forces $\tilde{F}_{r,j}$ observing that, although the global load is constant, the evolution of the contact for the rollers 3 and 8 has relevant consequences on the bearing load distribution, with all the terms $\tilde{F}_{r,j}$ showing a different trend. As highlighted in Figure 2.15, this has consequences on the angular position of the global resultant force $\mathbf{F}_{tot}^{O}$: this will change with the angular speed. As expected, at very low and very high speeds, we have that θ_F is null since the material behaves elastically and a symmetric stress distribution is obtained; on the other hand, at intermediate speeds, it is interesting to notice that, due to viscoelasticity, the application point of the net force moves from the perfectly lined position, that is along the $x-$axis: the evolution is clearly non-monotonic as dependent on the number of rollers participating to the contact.

Ultimately, let us observe that, unlike what happens in a purely elastic system, an additional clearance is induced due to the viscoelastic rheology: this hinders some rollers from participating to the load transmission, thus affecting the bearing load distribution and, as a consequence, the angular position of the resultant force.

Now, we can look more in detail at the distribution of displacements and stresses. Indeed, Figures 2.16, 2.17, 2.18, 2.19, 2.20 show the results in terms of displacements and pressures at the inner- and outer-raceway contact at increasing shaft angular speed. In detail, in the left column, we report the deformed contours of the rings, the net forces $\mathbf{F}_{tot}$ (red arrows), and the extensions of the contact areas (green curves) on the active rolling elements, i.e. on the rolling elements participating to the contact. In the right column, we plot the undeformed contours (dashed lines) and the deformed contours of the races, the latter magnified to better appreciate the viscoelastic effects (solid lines). Below, we can observe the dimensionless pressure distributions $\tilde{p} = p/E_0$ on each rolling element in the loaded zone.

For stationary contact, in Figure 2.16, we retrieve a Hertzian-like trend for the pressure distributions, and the resulting forces, $\mathbf{F}_{tot}$(red arrows), are directed along the load line, that is the $x-$axis.

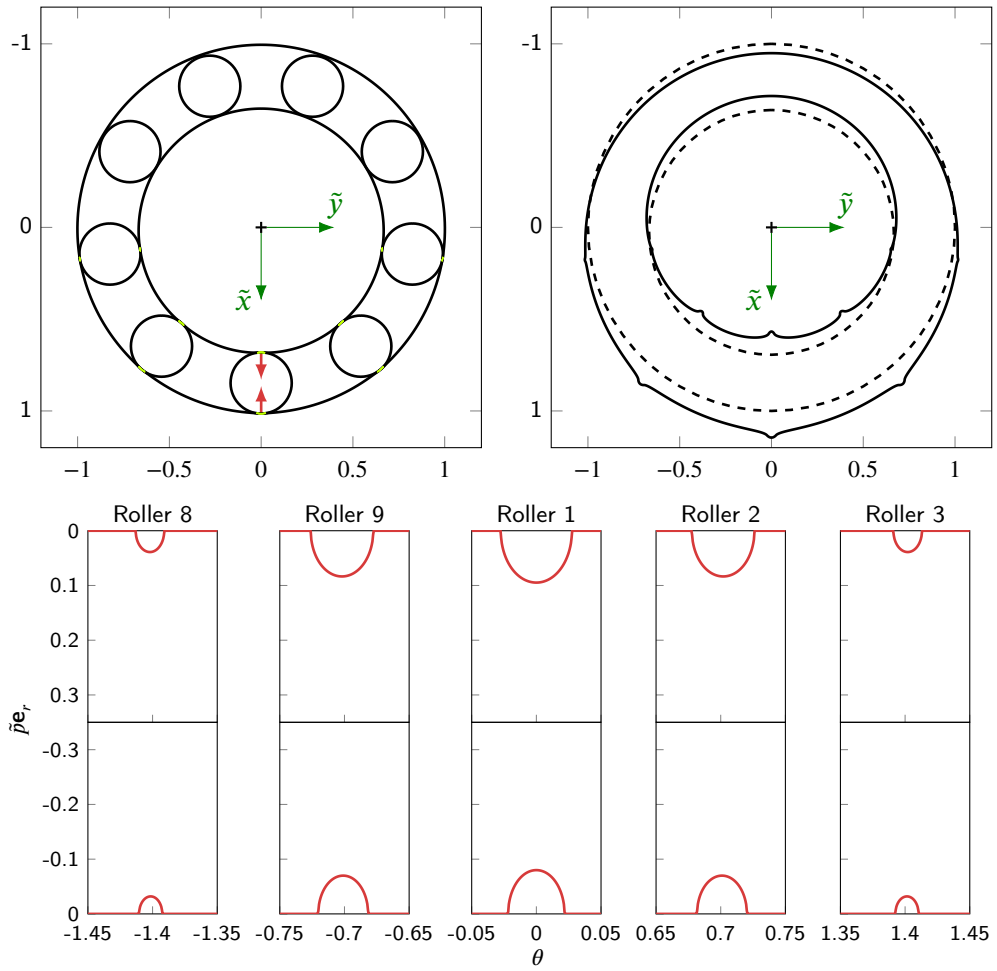

Figure 2.16: The deformed (solid black line) contour of the raceways, the resultant force $\mathbf{F}_{tot}$(red arrow), and the contact areas (green line) for each active rolling element on the left; the undeformed (dashed black line) and the magnified deformed contour of the raceways (solid black line), with $K = 10$ being the magnification factor, on the right. Results are carried out at $\tilde{\omega} = 0$, and fixed dimensionless force $\tilde{F} = F_x/E_0R_O = 6.5{\cdot}10^{-3}$; the pressure distribution acting on the rolling elements in the load zone, for the inner raceway contact (above) and the outer raceway contact (below). The axes $\tilde{x}$ and $\tilde{y}$ refer to the normalized $x-$ and $y-$coordinates, i.e., $\tilde{x} = x/R_O$ and $\tilde{y} = y/R_O$.

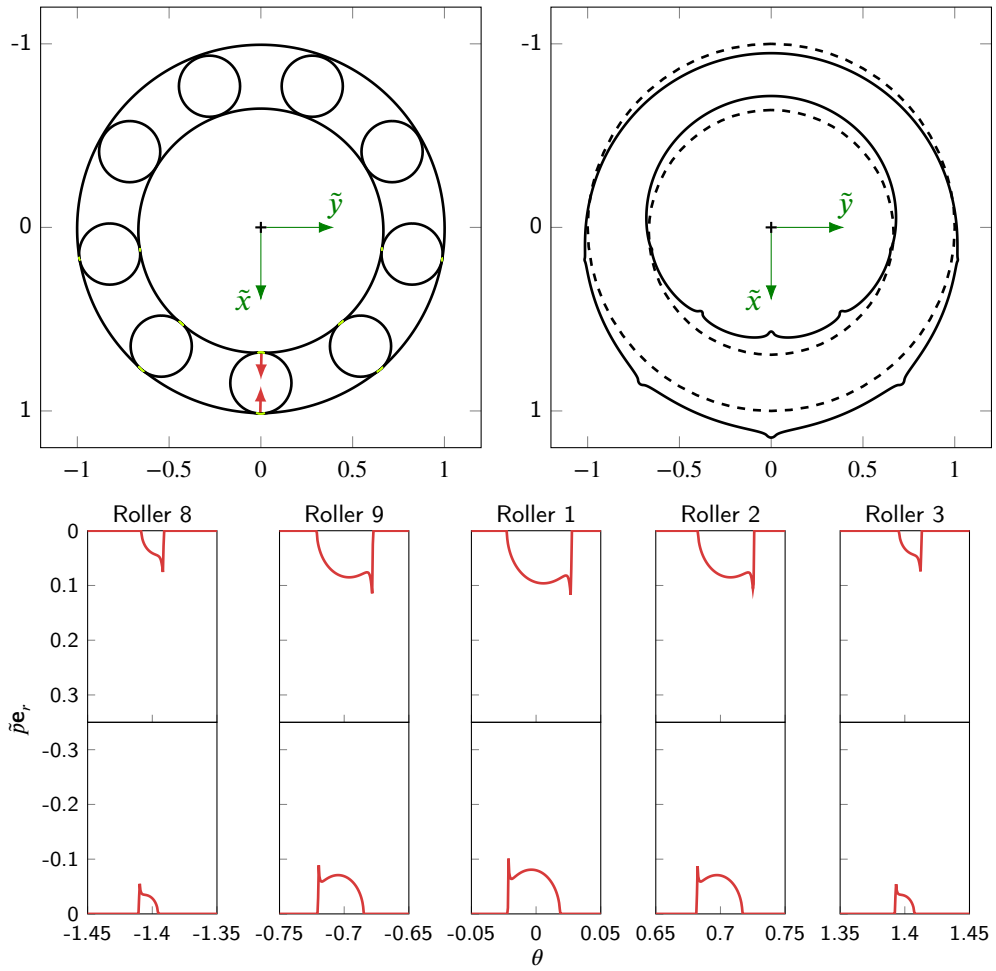

Figure 2.17: The deformed (solid black line) contour of the raceways, the net force $\mathbf{F}_{tot}$(red arrow), and the contact areas (green line) for each active rolling element on the left; the undeformed (dashed black line) and the magnified deformed contour of the raceways (solid black line), with $K = 10$ being the magnification factor, on the right. Results are carried out at $\tilde{\omega} = 0.004$, and fixed dimensionless force $\tilde{F} = F_x/E_0R_O = 6.5 \cdot 10^{-3}$; the pressure distribution acting on the rolling elements in the load zone, for the inner raceway contact (above) and the outer raceway contact (below). The axes $\tilde{x}$ and $\tilde{y}$ refer to the normalized $x-$ and $y-$coordinates, i.e., $\tilde{x} = x/R_O$ and $\tilde{y} = y/R_O$.

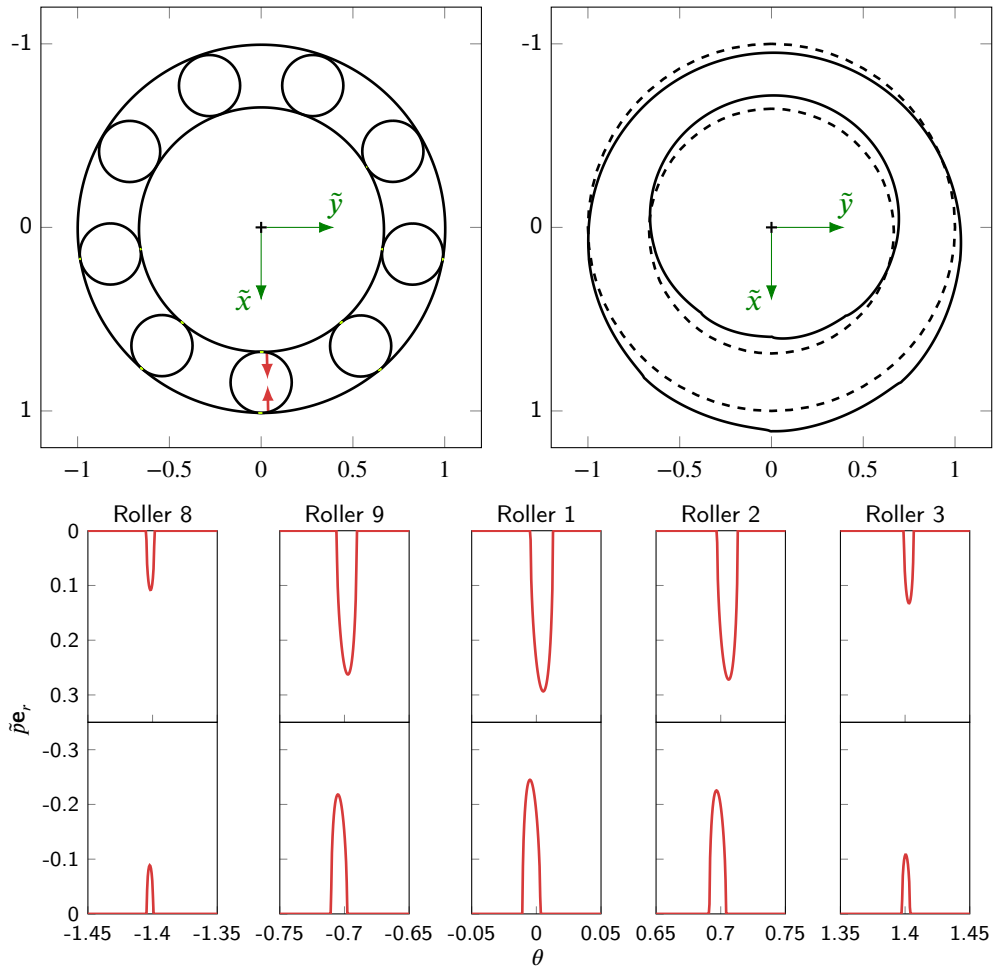

Figure 2.18: The deformed (solid black line) contour of the raceways, the net force $\mathbf{F}_{tot}$(red arrow), and the contact areas (green line) for each active rolling element on the left; the undeformed (dashed black line) and the magnified deformed contour of the raceways (solid black line), with $K = 10$ being the magnification factor, on the right. Results are carried out at $\tilde{\omega} = 0.2$, and fixed dimensionless force $\tilde{F} = F_x/E_0R_O = 6.5 \cdot 10^{-3}$; the pressure distribution acting on the rolling elements in the load zone, for the inner raceway contact (above) and the outer raceway contact (below). The axes $\tilde{x}$ and $\tilde{y}$ refer to the normalized $x-$ and $y-$coordinates, i.e., $\tilde{x} = x/R_O$ and $\tilde{y} = y/R_O$.

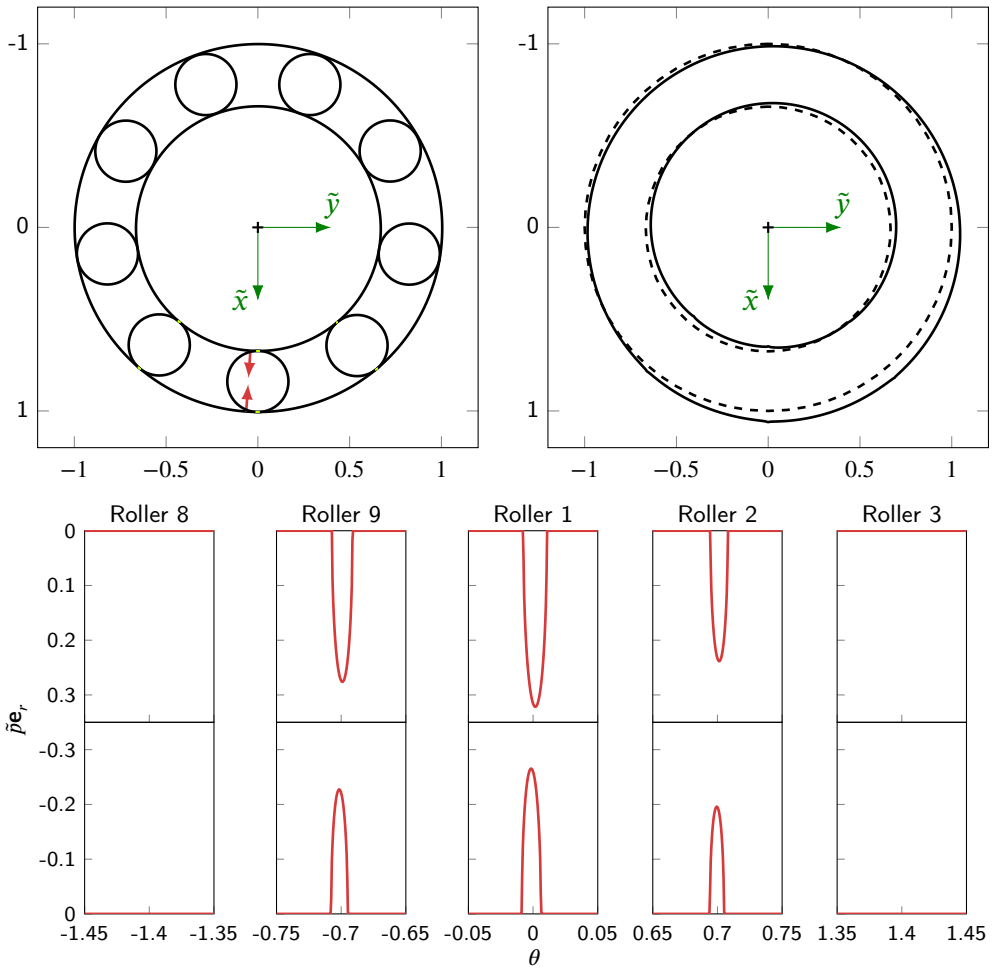

Figure 2.19: The deformed (solid black line) contour of the raceways, the net force $\mathbf{F}_{tot}$(red arrow), and the contact areas (green line) for each active rolling element on the left; the undeformed (dashed black line) and the magnified deformed contour of the raceways (solid black line), with $K = 10$ being the magnification factor, on the right. Results are carried out at $\tilde{\omega} = 1.4$, and fixed dimensionless force $\tilde{F} = F_x/E_0R_O = 6.5 \cdot 10^{-3}$; the pressure distribution acting on the rolling elements in the load zone, for the inner raceway contact (above) and the outer raceway contact (below). The axes $\tilde{x}$ and $\tilde{y}$ refer to the normalized $x-$ and $y-$coordinates, i.e., $\tilde{x} = x/R_O$ and $\tilde{y} = y/R_O$.

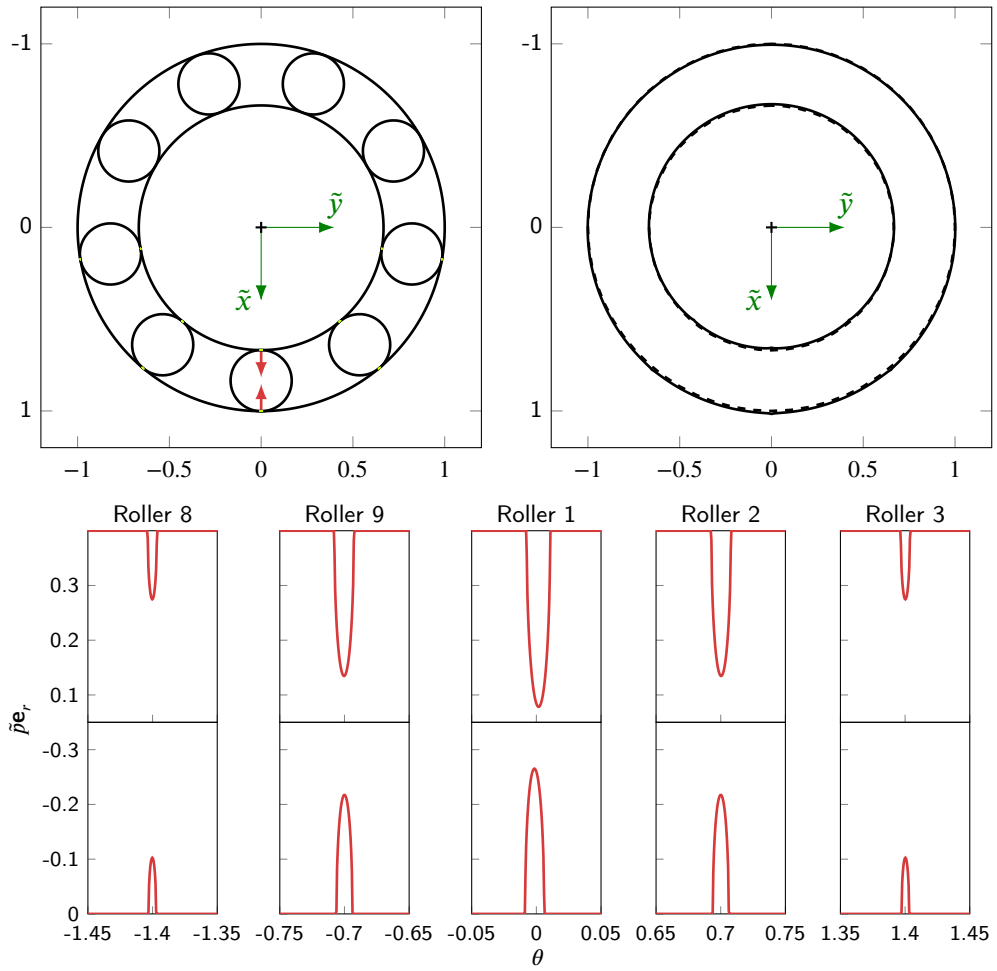

Figure 2.20: The deformed (solid black line) contour of the raceways, the net force $\mathbf{F}_{tot}$(red arrow), and the contact areas (green line) for each active rolling element on the left; the undeformed (dashed black line) and the magnified deformed contour of the raceways (solid black line), with $K = 10$ being the magnification factor, on the right. Results are carried out at $\tilde{\omega} = 10^3$, and fixed dimensionless force $\tilde{F} = F_x/E_0R_O = 6.5 \cdot 10^{-3}$; the pressure distribution acting on the rolling elements in the load zone, for the inner raceway contact (above) and the outer raceway contact (below). The axes $\tilde{x}$ and $\tilde{y}$ refer to the normalized $x-$ and $y-$coordinates, i.e., $\tilde{x} = x/R_O$ and $\tilde{y} = y/R_O$.

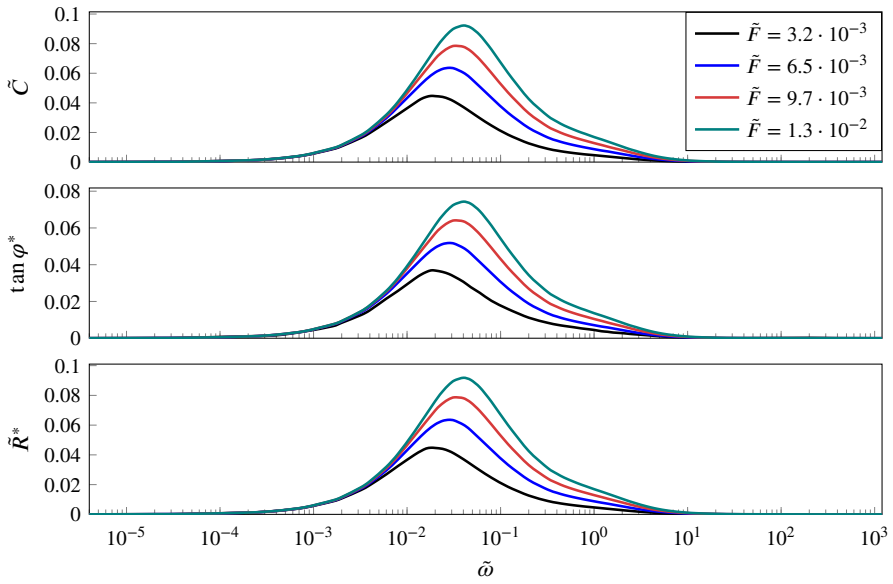

Figure 2.21: The friction torque due to viscoelastic rolling contact $\tilde{C} = |\mathbf{C}_t|/F_x R_O$, the tangent of friction angle $\varphi^* = \arccos(F_r/F_{tot})$, with F_r being the radial component of the net force F_{tot}, and the dimensionless friction circumference radius $\tilde{R}^* = R^*/R_O$ at different values of the dimensionless fixed load $\tilde{F} = F_x/E_0 R_O$, as a function of the dimensionless speed $\tilde{\omega}$. The dimensionless quantities refer to the outer raceway contact problem.

As soon as the speed is increased, we notice a peak appearing at the leading edge, while large displacement values are observed at the trailing edge, where the material is relaxing and, thus, a shrinking of the contact area occurs. This is evident in Figures 2.17 and 2.18. It is crucial to point out that the leading and the trailing edges observed at the inner raceway are inverted compared to the outer ring, consistently with the direction of the speed of the corresponding contact patches. Indeed, while the inner raceway contact patches move with a constant angular speed $\omega_{I,c}$ in a counterclockwise direction, we have that the contact strips at the outer raceway move with a clockwise angular speed $\omega_{O,c}$.

Crucially, at higher values of the shaft speed, and, specifically, for a dimensionless speed $\tilde{\omega}$ equal to $\tilde{\omega} = 1.4$, in Figure 2.19, we observe that the rollers 3 and 8 are not in contact anymore, as the material is unable to recover the viscoelastic deformation at the angular position occupied by these rollers: the penetration is not sufficient, in fact, to recover the viscoelasticity-induced decrease in the load-bearing capacity of these two rolling elements. Incidentally, at this stage, the inverted position, for the inner and the outer ring, of the trailing and the leading edges appears even more evident. Furthermore, it should be noted that, at very high speeds, an elastic regime is reached again, but this time it is the glassy one and the material behaves as a stiff elastic solid. Therefore, since we are keeping constant the normal force, the contact area reduces, and smaller displacements are retrieved. This is highlighted in Figure 2.20, where, as expected in the elastic field, all the rolling elements in the load zone are actively participating to the contact.

Now, as well proved in literature both theoretically and experimentally, the asymmetry in the pressure distribution, shown previously and related to the hysteretic behavior of the viscoelastic material, has consequences on the resultant force: the latter is tilted

with a certain angle with respect to the approach line, which is purely vertical, thus generating a friction torque $\mathbf{C}_t$ around the center of the bearing **O**. Indeed, as shown in Section 2.1, $\mathbf{F}_{tot}$ is tangent to the friction circumference, whose radius is equal to R^*. In Figure 2.21, we plot, with reference to the outer ring contact problem, for different values of the dimensionless fixed load $\tilde{F} = F_x/E_0R_O$, the dimensionless friction torque $\tilde{C} = |\mathbf{C}_t|/F_xR_O$, the trigonometric tangent of the friction angle φ^*, defined as the angle $\mathbf{F}_{tot}$ is tilted with respect to the radial direction, i.e., $\varphi^* = \arccos(F_r/F_{tot})$, and the dimensionless radius of the friction circumference $\tilde{R}^* = R^*/R_O$. As expected, at very low and very high velocities, where the material behaves as an elastic solid, these quantities tend to zero, as they are closely related to viscoelastic energy dissipation: this is negligible in the rubbery and glassy regimes, while reaching its maximum value at intermediate speeds. Interestingly, as the load is increased, a larger energy dissipation due to viscoelastic friction is observed: the viscoelastic hysteresis is, indeed, a bulk phenomenon. Furthermore, also the peak of the curves is shifted toward higher frequencies: this is, *inter alia*, related to the mutual interaction between the rollers, that is, to the number of them participating to contact, and, thus, can depend on the load.

2.3.3 Experimental corroboration

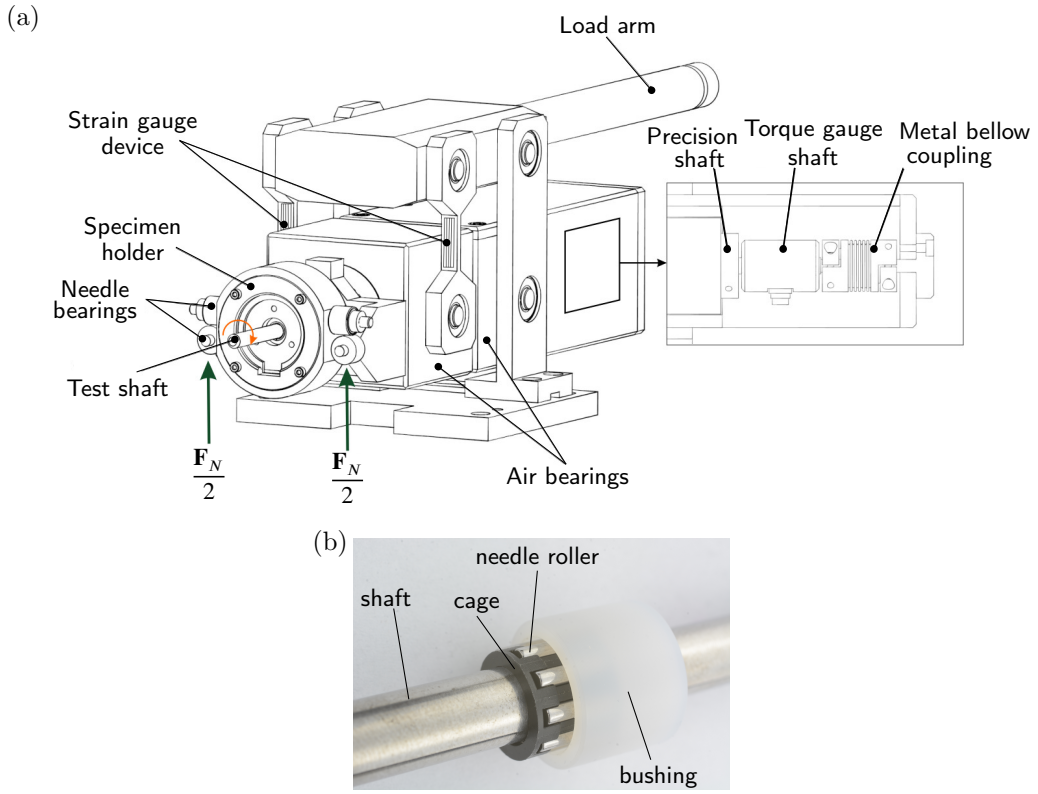

Figure 2.22: Schematic of the experimental rig (a); test sample assembly constituted by a Cf53-made precision test shaft and a needle roller bearing with PTFE-based bushing(b).

It is important to notice that the current Boundary Element methodology is not limited to viscoelastic materials with just one relaxation time, but can be employed for any linear viscoelastic material to investigate, in terms of stresses, deformation, and friction, the steady-state operating condition of a rolling element bearing, in which the viscoelastic raceways are characterized by a large number of relaxation times.

Consequently, to corroborate the methodology, we carry out tribological tests performed on a specific tribometer (Precision Bearing Test Rig 2) at the Austrian Excellence Centre for Tribology (AC2T research GmbH). Comparable testing on this precision bearing test rig, sketched in Figure 2.22a, was successfully conducted in the past for porous sinter metal journal bearings [85, 86]. The specific design of the tribometer enables a multitude of test procedures to be programmed: the test temperature, which can be varied via a controlled resistive heating element, the shaft rotation speed, the normal load, and the friction torque can be automatically recorded and analysed. For the application of this thesis, the experimental setup has been particularized as follows. A Cf53 steel precision test shaft with diameter 8 mm (⌀8h6), is clamped in the chuck and then driven by an electric motor. As a test sample, we focus on a simplified version of the bearing previously studied in the numerical part: a needle roller bearing with a PTFE bushing mounted in the specimen holder, the latter being connected to a torque transducer via an air-bearing supported shaft. The bushing has an inner diameter of 12 mm, an outer diameter of 16 mm, and a length of 12 mm. To complete the test sample assembly a

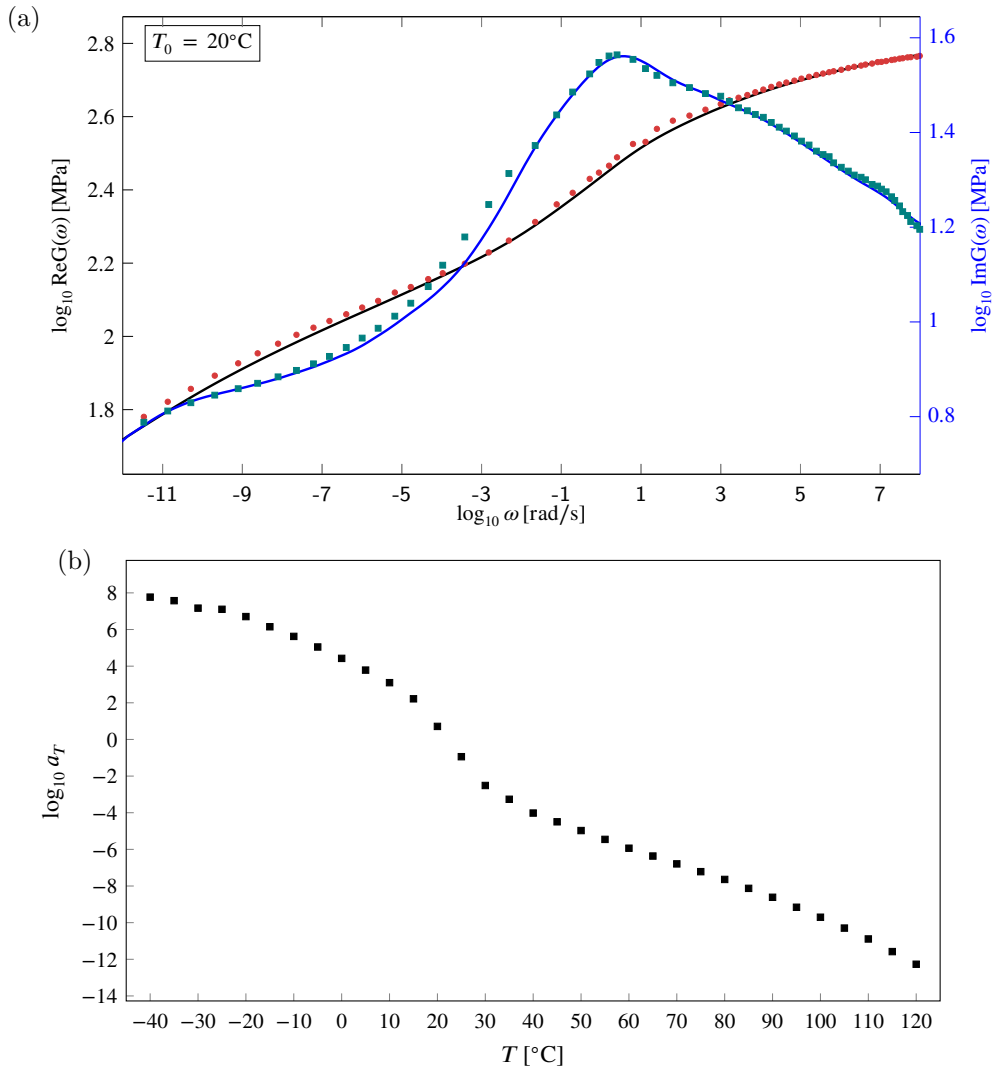

Figure 2.23: The viscoelastic modulus master curves for Polytetrafluoroethylene (PTFE). The storage(black line) and the loss(blue line) moduli, respectively equal to ReG(ω) and ImG(ω) (a); the viscoelastic modulus shift factors a_T as a function of temperature for Polytetrafluoroethylene (PTFE) (b). The reference temperature is $T_0 = 20°C$.

needle roller cage, with 9 needle rollers with a diameter and length being ⌀2 mm and 7.8 mm respectively, is placed between the test shaft and the bushing, as shown in Figure 2.22b.

In order to carry out the numerical-experimental corroboration, it is necessary to characterize the polymer's mechanical properties and, specifically, the viscoelastic complex modulus. Hence, the viscoelastic response of the PTFE material has been characterized via the MCR 702 Dynamic Mechanical Analyzer (DMA), manufactured by Anton Paar, which enables the measurement of the viscoelastic complex modulus in given frequency and temperature ranges. The characterization is performed on a PTFE bar, with a cross-section of 3 mm × 3 mm and a length of 25 mm, under torsional loading over a frequency interval between 0.1 Hz and 10 Hz, and temperatures ranging

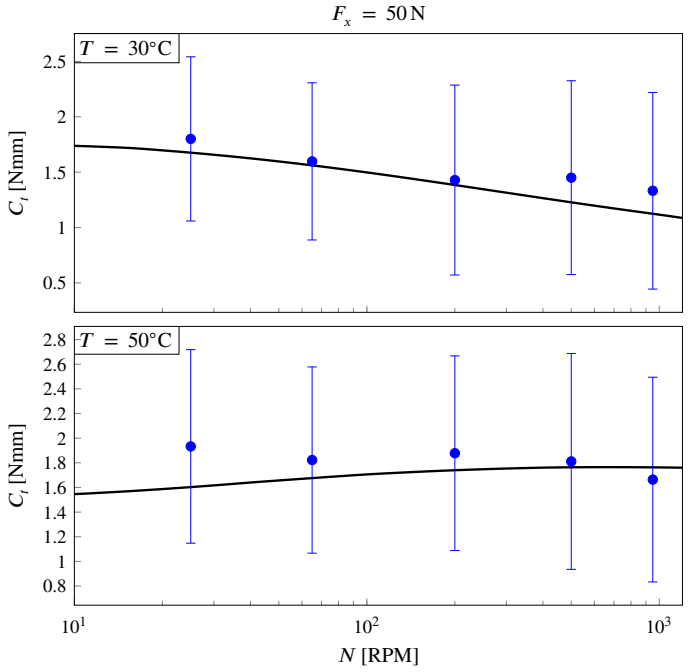

Figure 2.24: The viscoelastic friction torque C_t as a function of the shaft speed N. The numerical predictions(solid black lines), carried out at a fixed load $F_x = 50\,\mathrm{N}$ and at different temperatures, $T = 30°\mathrm{C}$ and $T = 50°\mathrm{C}$, are compared to the measured ones. The outer ring is made of Polytetrafluoroethylene (PTFE). For the latter, the scatter is reported.

from $-40°\mathrm{C}$ to $120°\mathrm{C}$ with $5°\mathrm{C}$ steps. Figure 2.23a shows the DMA data points and the resulting fitted complex modulus in terms of storage and loss modulus, $\mathrm{ReG}(\omega)$ and $\mathrm{ImG}(\omega)$ respectively, at a reference temperature $T_0 = 20°\mathrm{C}$. The master curve is constructed by making use of the shift factors a_T, sketched in Figure 2.23b as a function of temperature. Hence, the definition of the shift factors a_T allows us to retrieve the complex viscoelastic modulus for any temperature and frequency, being $\mathrm{G}(\omega, T)$ defined as $\mathrm{G}(\omega, T) = \mathrm{G}(a_T\,\omega, T_0)$, as treated in Section 1.2.

Within the scope of this study, torque measurements have been carried out with different settings, by varying the radial load and the temperature. Particularly, tests have been performed at two different load conditions, $F_x = 50\,\mathrm{N}$ and $F_x = 100\,\mathrm{N}$, at $T = 30°\mathrm{C}$ and $T = 50°\mathrm{C}$.

Figure 2.24 presents the comparison, in terms of the viscoelastic friction torque C_t, between the numerical predictions and experimental outcomes at a fixed load $F_x = 50\,\mathrm{N}$ and at different temperatures, $T = 30°\mathrm{C}$ and $T = 50°\mathrm{C}$. We notice that experimental data are in very good agreement with the numerical curve. Scatter is generally large possibly due to wear, other friction contributions, and parasitic effects occurring in the rig, but we reckon that this does not affect the reliability of the comparison as the investigation is focused on the purely viscoelastic contribution to friction and its dependence on the rotational speed.

When increasing the load to $F_x = 100\,\mathrm{N}$, as shown in Figure 2.25, we obtain a good agreement for a fixed temperature of $T = 30°\mathrm{C}$. In fact, the descending trend of the friction torque, obtained from numerical analysis, matches the descending trend

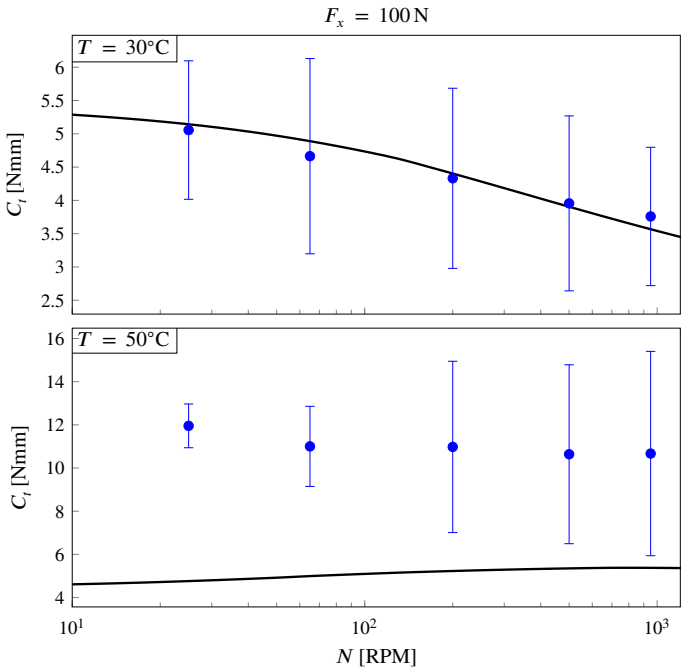

Figure 2.25: The viscoelastic friction torque C_t as a function of the shaft speed N. The numerical predictions(solid black lines), carried out at a fixed load $F_x = 100\,\mathrm{N}$ and at different temperatures, $T = 30°\mathrm{C}$ and $T = 50°\mathrm{C}$, are compared to the measured ones. The outer ring is made of Polytetrafluoroethylene (PTFE). For the latter, the scatter is reported.

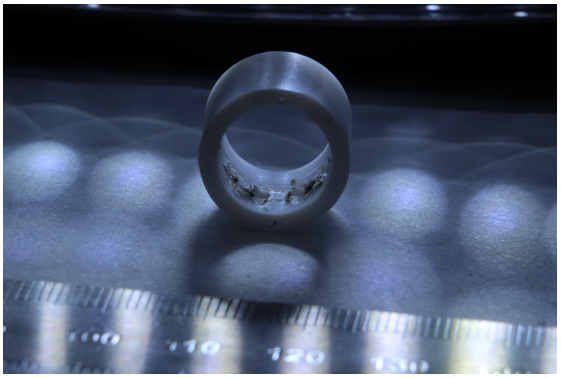

Figure 2.26: PTFE bushing sample after a test conducted for a normal load equal to 100 N and a temperature equal to 50 °C. Scratches and material loss are evident.

of the average experimental data. At $T = 50°\mathrm{C}$, a certain deviation between numerical outcomes and experiments appears: this is due to high load and high temperature conditions, and the consequent high wear. The latter was confirmed by the scratches detected on the sample after the conclusion of the test, as Figure 2.26 shows.

The same test series has been conducted for a different bushing material, namely Polyamide 6 (PA6). In particular, a bar, with a cross-section of 3 mm × 3 mm and a length of 25 mm, has been characterized via the MCR 702 Dynamic Mechanical Analyzer (DMA), under torsional loading over a frequency interval between 0.1 Hz and 10 Hz, and temperatures ranging from $-20°\mathrm{C}$ to $120°\mathrm{C}$ with $5°\mathrm{C}$ steps. Figure 2.27a shows

the DMA data points and the resulting fitted complex modulus in terms of storage and loss modulus, ReG(ω) and ImG(ω) respectively, at a reference temperature $T_0 = 20°C$, while Figure 2.27b presents the shift factors a_T, as a function of temperature, used to reconstruct the master curve. Incidentally, by comparison of the numerical predictions with the experimental outcomes, good agreement is observed for a fixed load of $F_x = 50\,\mathrm{N}$ and temperature equal to $T = 30°C$ and $T = 50°C$; conversely, large deviations are observed at $T = 80°C$. The agreement is appreciable also for a fixed load $F_x = 100\,\mathrm{N}$, and interestingly, while at $T = 30°C$ a certain offset is noticed, at $T = 80°C$ the friction torques predicted are close to those observed experimentally.

Hence, the agreement shown between numerics and experiments for the two polymeric materials investigated in the present analysis corroborates the potentialities of the proposed numerical approach.

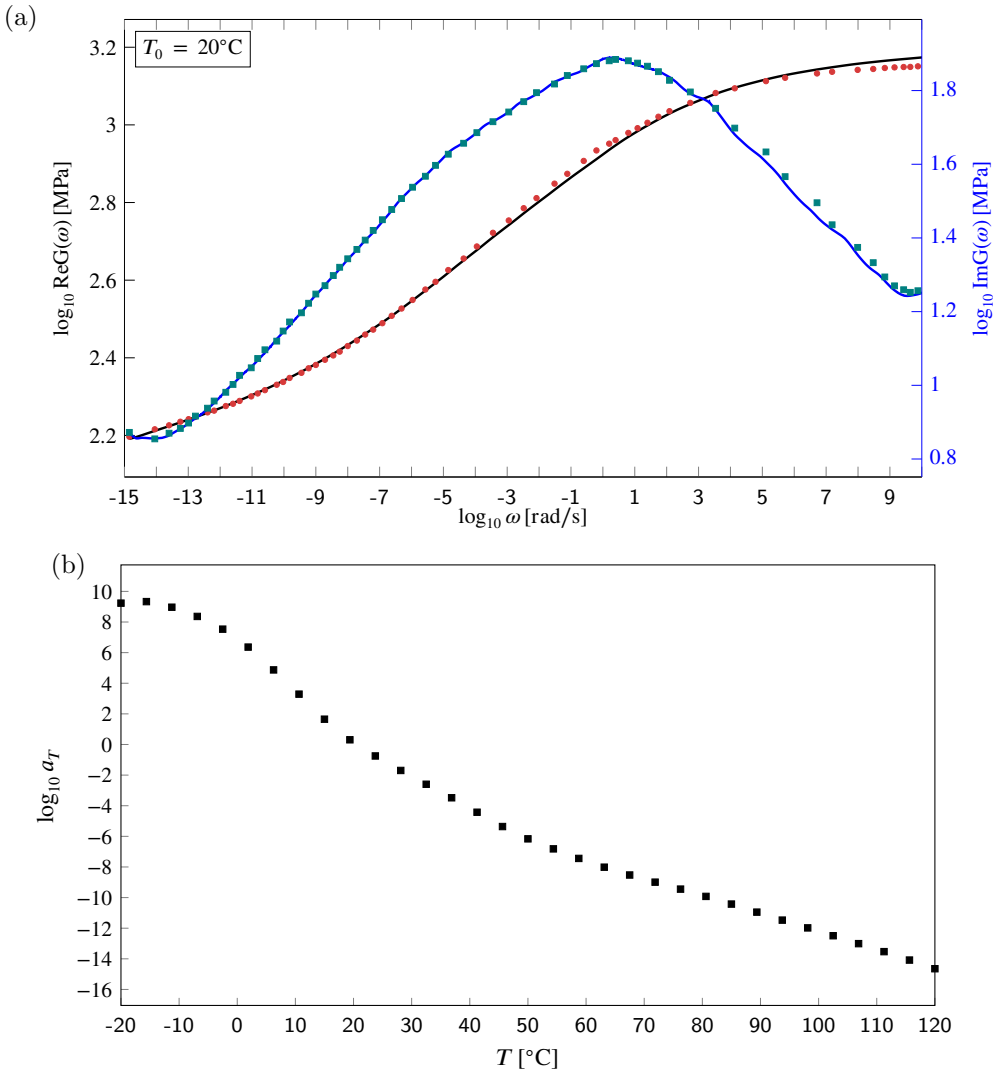

Figure 2.27: The viscoelastic modulus master curves for Polyamide 6 (PA6). The storage(black line) and the loss(blue line) moduli, respectively equal to ReG(ω) and ImG(ω) (a); the viscoelastic modulus shift factors a_T as a function of temperature for Polyamide 6 (PA6) (b). The reference temperature is $T_0 = 20°C$.

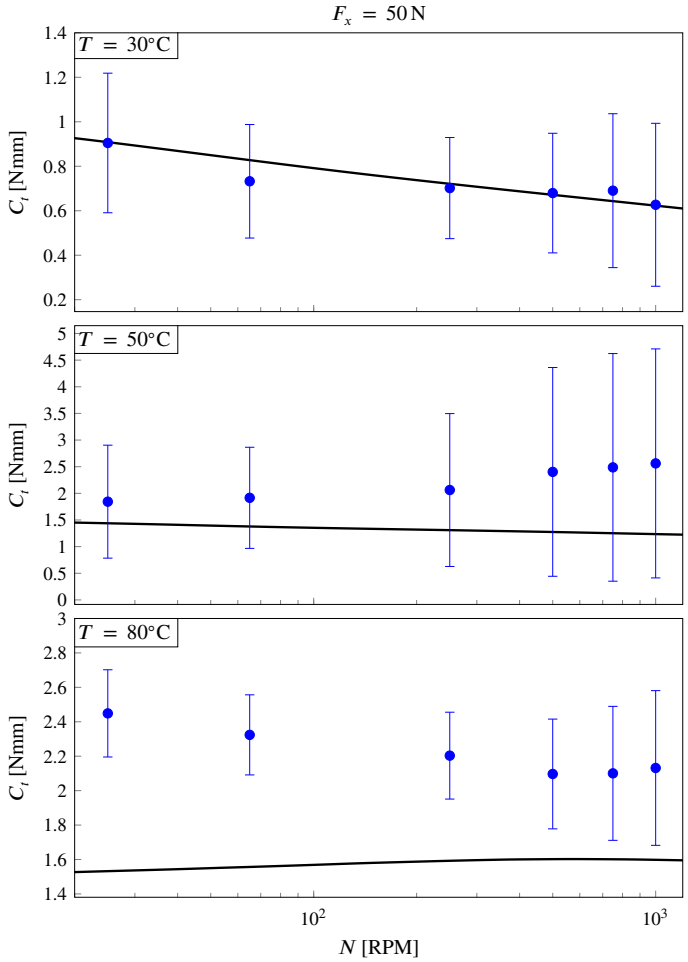

Figure 2.28: The viscoelastic friction torque C_t as a function of the shaft speed N. The numerical predictions(solid black lines), carried out at a fixed load $F_x = 50\,\mathrm{N}$ and at different temperatures, $T = 30°\mathrm{C}$, $T = 50°\mathrm{C}$ and $T = 80°\mathrm{C}$, are compared to the measured ones. The outer ring is made of Polyamide 6 (PA6). For the latter, the scatter is reported.

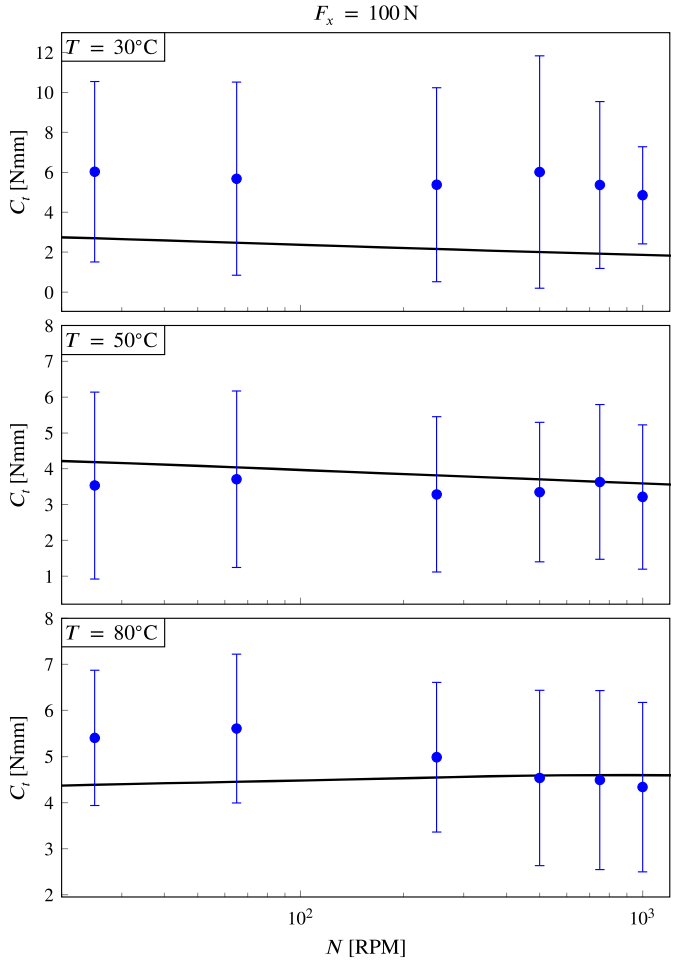

Figure 2.29: The viscoelastic friction torque C_t as a function of the shaft speed N. The numerical predictions(solid black lines), carried out at a fixed load $F_x = 100\,\mathrm{N}$ and at different temperatures, $T = 30°\mathrm{C}$, $T = 50°\mathrm{C}$ and $T = 80°\mathrm{C}$ are compared to the measured ones. The outer ring is made of Polyamide 6 (PA6). For the latter, the scatter is reported.

Chapter 3

Lubricated circular contacts

The importance that soft matter lubrication has gained in the industrial panorama is indubitable. This marked interest paves over the continuously increasing demand for new polymers [13, 44, 47, 48], biomedical implants [30, 31], soft tissues [87]. In fact, these materials are characterized by a range of advantageous properties in terms of resistance to environmental conditions, lighter weight, and reduced costs in manufacturing. Hence, the continuous shift from metals to polymers occurring in the last decades: seals [88, 89], dampers [90], and polymer bearings [45] are just examples. Nevertheless, due to their complex rheology, the mechanical response of such materials is often complicated to predict: indeed, they exhibit a strong time- and temperature-dependent behavior, which can be modeled as viscoelastic. A clear understanding of the performance of this class of materials is indeed challenging, especially when other phases are involved as it occurs in lubricated contacts, but is of the utmost importance. Indeed, in spite of the considerable efforts in investigating dry contact mechanics involving soft materials [8–10, 91], limited research has been carried out to highlight the mechanisms governing the interactions at the lubricated interface in the presence of viscoelastic materials [23, 28, 29, 92]. Furthermore, the presence of roughness may exacerbate even more the complexity of the contact problem [93, 94]. Pioneering studies were carried out by Rohde et al. [95], who analyzed the effects of viscoelasticity and fluctuating loads on the elastohydrodynamic squeeze film, and by Elsharkawy [96], who developed a numerical procedure to study the visco-elastohydrodynamic lubrication (VEHL) line contact problems, based on an iterative Newton-Raphson scheme. Later, Hooke [97] investigated the relationship between the lubrication behavior and dry contact pressures when soft solids are considered; in particular, in his analysis he found that the pressure distribution remains close to that obtained in dry, frictionless contact since the corresponding deformations are very large with respect to the film thickness. Another contribution has been provided by Scaraggi and Persson [28], who studied the effects of viscoelasticity and random surface height fluctuations on the Stribeck curve, on the traction and the separation field at the contact interface of steady sliding line contacts. Furthermore, Putignano and Dini [98–100], introduced a generalized numerical methodology to capture fluid-solid interactions, obtained by coupling a Boundary Element (BE) approach that deals with the solid viscoelastic deformation and a finite difference scheme to model the fluid flow dynamics, showing good agreement with the experimental outcomes [101]. It is evident that these interactions occurring at the lubricated interfaces are critical in a variety of contexts, including power transmission components: indeed, the role of lubrication is fundamental in rotor dynamics applications, as it reduces the level of wear of the contacting pairs. A

component of the utmost importance in a variety of industrial applications is the journal bearing, and specifically, we will analyze how viscoelasticity affects the response of such bearing, when at least one of the two interacting pairs is viscoelastic.

3.1 Steady-state 1D Reynolds equation

Before dealing with the visco-elastohydrodynamic lubrication (VEHL) problem at hand, that is the polymer journal bearing, we need first to introduce the Reynolds equation for lubrication [102], which allows us to describe the lubricant behavior when it is interposed between two bodies. For the sake of the present work, we will focus on the steady-state 1D form of the Reynolds equation.

Consider the system shown in Figure 3.1, in which body 1 is fixed, while body 2 is translating with horizontal velocity $\mathbf{V} = V\mathbf{i}$, with $\mathbf{i}$ being the unit vector of the x-axis. Furthermore, let us define the fluid film thickness $h = h(x)$, and the length of the slider along the x-direction L. Let us suppose that, in the z-direction, the slider and the body 2 are infinitely long; in this case, the fluid motion is the same in any section along the z-axis. In other words, if we call B the length along the z-direction, we have that $B \gg L$. Whence, lateral flux is negligible. However, it should be pointed out that this hypothesis is introduced to simplify our study and does not hold in reality. Furthermore, we can say that $h \ll L$ and this is true also in real cases, since the order of magnitude of h is about 100 μm or less, while the length L may be of several centimeters or even more. In addition, let us suppose the fluid is Newtonian, so that we can introduce the rheological equation that relates the tangential stress tensor $\mathbf{T}$ and the strain rate tensor $\dot{\mathbf{E}}$:

$$\mathbf{T} = \mathbf{A}\dot{\mathbf{E}}. \tag{3.1}$$

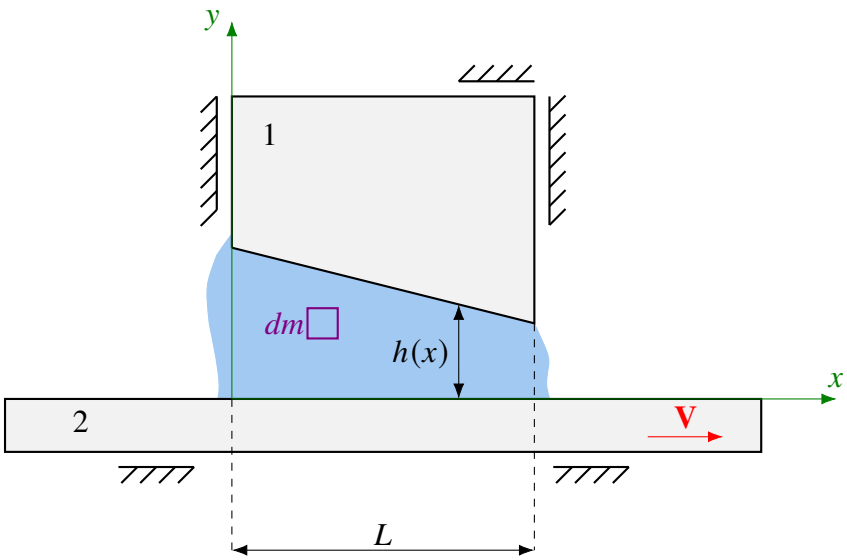

Figure 3.1: Schematics of a 1D lubricated system.

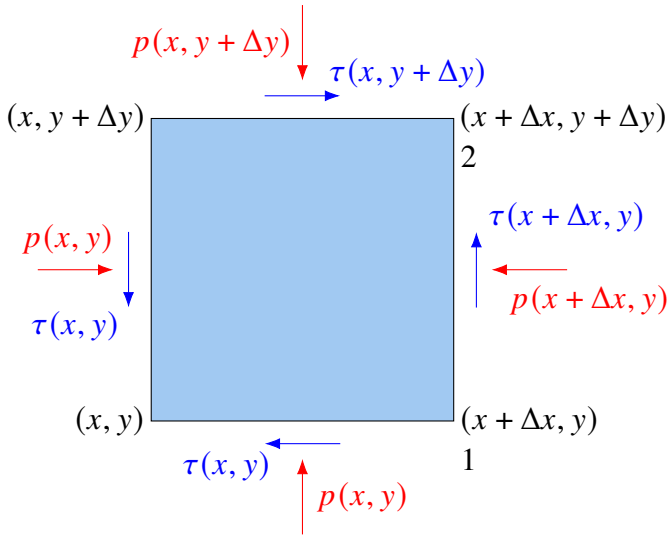

Figure 3.2: Schematics of the pressure and the shear stress acting on the faces of an infinitesimal volume.

We know that, for an isotropic fluid, all the 81 components of $\mathbf{A}$, which is a fourth-order tensor, depend on two parameters, which, in the case of Newtonian fluids, are η and η', respectively the dynamic and bulk viscosity. However, we will neglect this last quantity and say that only the dynamic viscosity identifies the rheological relation since we refer to an incompressible fluid. Furthermore, let us assume that the temperature is uniform in the fluid film. Clearly, this is an approximation, since we have energy dissipation due to shear stress and, consequently, heat is produced.

Finally, we are looking at the system by an Eulerian reference frame, as we are in steady-state conditions, namely the quantities depend only on the spatial coordinates and not on time.

Now, to write down the equations of motion, we consider an infinitesimal fluid volume, with a mass dm, as shown in Figure 3.2. We can study this volume assuming it to be isolated from the rest of the fluid, so that the latter is considered as external to the system.

Before proceeding, let us make some considerations about the forces acting on such fluid element. Indeed, by looking at Figure 3.2, the pressure can actually change while moving between point 1 and point 2 along the y-direction, but it can be shown that this variation is negligible. In fact, we can say that the force acting on the surface delimited by 1 and 2 is given by:

$$\Delta F = p \Delta y B. \tag{3.2}$$

Assuming for simplicity that the pressure distribution on the surface is linear, the relation becomes

$$\Delta F = p_{avg} \Delta y B, \tag{3.3}$$

where

$$p_{avg} = \frac{p_1 + p_2}{2} = \frac{p_1 + p_1 + \Delta p_{12}}{2} = p_1 + \frac{\Delta p_{12}}{2},$$

with Δp_{12} denoting the variation of pressure between the two points.

Therefore, the following is obtained:

$$\Delta F = \left(p_1 + \frac{\Delta p_{12}}{2}\right)\Delta y B = p_1 \Delta y B + \underbrace{\cancel{\frac{1}{2}\Delta p_{12}\Delta y B}}_{\text{second-order quantity}} . \tag{3.4}$$

As $\Delta y \to 0$, the second-order term can be neglected. Hence, the pressure variation along the y-direction at the left and at the right faces of the elementary element is negligible. Analogously, the same reasoning holds for the pressure variation along the x-direction at the top and at the bottom faces.

Hence, let us consider the equilibrium of the volume along the x-axis:

$$\begin{gathered} p(x,y)\Delta y B - p(x+\Delta x, y)\Delta y B + \tau(x, y+\Delta y)\Delta x B - \tau(x,y)\Delta x B = \\ = dm\ a_x(x,y) = a_x(x,y)\rho(x,y)\Delta x \Delta y B, \end{gathered}$$

whence

$$-\frac{p(x+\Delta x, y) - p(x,y)}{\Delta x} + \frac{\tau(x, y+\Delta y) - \tau(x,y)}{\Delta y} = \rho(x,y) a_x(x,y). \tag{3.5}$$

Thus, as $\Delta x \to 0$ and $\Delta y \to 0$, we can write

$$-\frac{\partial p}{\partial x} + \frac{\partial \tau}{\partial y} = \rho a_x. \tag{3.6}$$

Analogously, on the y-direction we have

$$-\frac{\partial p}{\partial y} + \frac{\partial \tau}{\partial x} = \rho a_y. \tag{3.7}$$

Notice that in the equations above we do not consider the z-coordinate, since we made the hypothesis $B \gg L$: any quantity is a function of x and y.

Now, the accelerations a_x and a_y in Equation (3.6) and Equation (3.7) can be evaluated respectively as

$$a_x = \frac{d}{dt} v_x(x,y) = \nabla v_x \cdot \mathbf{v} = \frac{\partial v_x}{\partial x} v_x + \frac{\partial v_x}{\partial y} v_y, \tag{3.8}$$

and

$$a_y = \frac{d}{dt} v_y(x,y) = \nabla v_y \cdot \mathbf{v} = \frac{\partial v_y}{\partial x} v_x + \frac{\partial v_y}{\partial y} v_y. \tag{3.9}$$

Observe that these are quadratic functions of the velocity and, therefore, are related to the kinetic energy. Now, let us recall the definition of the Reynolds number
$\mathrm{Re} = \rho v l/\eta$, with v being the flow speed, l is the characteristic linear dimension, ρ and η are respectively the fluid density and viscosity. More conveniently, we can rephrase this definition as:

$$\mathrm{Re} = \frac{\rho v^2}{\eta \frac{v}{l}}, \tag{3.10}$$

from which it is overt that the term at the numerator (namely, the dynamic pressure) is proportional to the kinetic energy per unit volume at a certain point and, then, it is associated with the acceleration and the inertial forces, while the term at the denominator is related to viscous forces. Therefore, the Reynolds number represents the ratio between

the inertial and the viscous forces. Incidentally, consider the characteristic length to be h, since, moving along the y direction, we have the most important velocity variation[1].

Referring to the system under consideration (see Figure 3.1), the Reynolds number Re is equal to:

$$\mathrm{Re} = \frac{\rho V^2}{\eta \frac{V}{h}},$$

and, since h is very small, we have that $\mathrm{Re} < 1$, i.e. the inertial effects are negligible and the flow is laminar. Hence, Equation (3.6) and Equation (3.7) can be rewritten, respectively, as

$$-\frac{\partial p}{\partial x} + \frac{\partial \tau}{\partial y} = 0 \tag{3.11}$$

and

$$-\frac{\partial p}{\partial y} + \frac{\partial \tau}{\partial x} = 0. \tag{3.12}$$

In other words, we can say that all the forces related to the fluid density can be neglected and so we have to consider surface forces only. To this regard, since the fluid is Newtonian, we can write the relationship between shear stress and strain rate as

$$\tau_{21} = \tau_{12} = 2\eta\dot{\varepsilon}_{12}, \tag{3.13}$$

where

$$\dot{\varepsilon}_{12} = \frac{1}{2}\left(\frac{\partial u}{\partial y} + \frac{\partial v}{\partial x}\right), \tag{3.14}$$

with u and v being respectively the components of the fluid particle velocity along the x- and y-axis.

Recalling that the flow is laminar ($\mathrm{Re} < 1$), and that the velocity u varies between 0 and V due to no-slip condition, we can estimate the partial derivatives $\partial v/\partial x$ and $\partial u/\partial y$ as:

$$\left|\frac{\partial v}{\partial x}\right| \simeq \left|\frac{v(L) - v(0)}{L}\right| \simeq \frac{Vh/L}{L} = \frac{Vh}{L^2}, \tag{3.15a}$$

$$\left|\frac{\partial u}{\partial y}\right| \simeq \left|\frac{u(h) - u(0)}{h}\right| = \frac{V}{h} \tag{3.15b}$$

whence

$$\frac{|\partial v/\partial x|}{|\partial u/\partial y|} \simeq \frac{Vh/L^2}{V/h} = \left(\frac{h}{L}\right)^2 \ll 1. \tag{3.16}$$

For this reason, we can rephrase Equation (3.14) as:

$$\dot{\varepsilon} = \frac{1}{2}\frac{\partial u}{\partial y}, \tag{3.17}$$

and the shear stress is equal to

$$\tau = \eta\frac{\partial u}{\partial y}. \tag{3.18}$$

[1]No-slip condition is assumed: in a very short distance the velocity of the fluid varies from 0 near the body 1 to V close to the body 2.

Then, from Equation (3.11) and Equation (3.12), we obtain:

$$-\frac{\partial p}{\partial x}+\eta\frac{\partial^2 u}{\partial y^2}=0 \tag{3.19}$$

and

$$-\frac{\partial p}{\partial y}+\eta\frac{\partial^2 u}{\partial x\partial y}=0. \tag{3.20}$$

Next, attention is paid to the terms $\partial p/\partial x$ and $\partial p/\partial y$. Specifically, by making use of the Taylor expansion applied on a given function $f(y)$, we can evaluate the second derivative $f''(y_0)$ as

$$f''(y_0)=\frac{f(y_0+\Delta y)-2f(y_0)+f(y_0-\Delta y)}{\Delta y^2}+\mathcal{O}(\Delta y^2) \tag{3.21}$$

and, consequently, we have that

$$\left|\frac{\partial^2 u}{\partial y^2}\right|\simeq\frac{V}{h^2},\qquad\left|\frac{\partial^2 u}{\partial x\partial y}\right|\simeq\frac{V}{hL}, \tag{3.22}$$

whence

$$\frac{\left|\partial^2 u/\partial x\partial y\right|}{\left|\partial^2 u/\partial y^2\right|}\simeq\frac{V}{hL}\frac{h^2}{V}=\frac{h}{L}\ll 1. \tag{3.23}$$

Referring to Equation (3.19) and Equation (3.20), it is overt that the dependence of the pressure on the coordinate y is negligible, so that we can approximate it as

$$p=p(x). \tag{3.24}$$

Hence, Equation (3.19) can be rephrased as:

$$p'(x)=\frac{dp}{dx}=\eta\frac{\partial^2 u}{\partial y^2}. \tag{3.25}$$

Equation (3.25) can be then integrated to obtain the velocity field $u(x,y)$ as:

$$u(x,y)=\frac{1}{\eta}p'(x)\frac{y^2}{2}+c_1(x)y+c_2(x), \tag{3.26}$$

were it can be noticed that the velocity u is nonlinear in y. To determine the two constants of integration, we consider no-slip boundary conditions [2]

$$u(x,y=0) = V \tag{3.27a}$$
$$u(x,y=h) = 0 \tag{3.27b}$$

so that we can express the velocity field $u(x,y)$ as:

$$u(x,y)=-\frac{h^2}{2\eta}p'(x)\frac{y}{h}\left(1-\frac{y}{h}\right)+V\left(1-\frac{y}{h}\right). \tag{3.28}$$

[2]These conditions are not exactly true. If we look closely at the surfaces, we can notice a small relative velocity of the fluid particles with respect to the two bodies. However, this velocity is really small, so that it is a good approximation to say the fluid adheres to the surfaces. This reasoning does not always hold: indeed, in microchannels we need to consider the fact that the fluid is sliding with a very small velocity on the surface.

In order to achieve a qualitative and quantitative description of the phenomenon, we have to combine Equation (3.28) with the mass conservation equation. Specifically, since the density is constant, we can consider the volumetric flow rate constant at each section x due to mass conservation. To facilitate the calculations, instead of the volumetric flow rate Q, we will consider the quantity $q = Q/B$, since the transversal length is not significant in the one-dimensional case we are dealing with. Then, the mass conservation equation, in the absence of squeeze, is expressed as:

$$\frac{dq}{dx} = 0. \tag{3.29}$$

By making use of Equation (3.28), we can derive the expression of the flow rate for the generic section x, namely

$$q = \int_0^h u(x,y)dy = -\frac{h^3}{12\eta}p'(x) + \frac{Vh}{2}. \tag{3.30}$$

By entering the expression of the flow rate q into the mass conservation equation (see Equation (3.29)), we obtain the Reynolds equation for the one-dimensional case:

$$\frac{d}{dx}\left(-\frac{h^3}{12\eta}\frac{dp}{dx}\right) + \frac{d}{dx}\left(\frac{Vh}{2}\right) = 0. \tag{3.31}$$

In general, if both body 1 and body 2 are moving with a certain velocity, it is possible to introduce the average velocity

$$\tilde{V} = \frac{V_1 + V_2}{2},$$

so that Equation (3.30) and Equation (3.31) become, respectively,

$$q = -\frac{h^3}{12\eta}p'(x) + \tilde{V}h \tag{3.32}$$

and

$$\frac{d}{dx}\left(\frac{h^3}{12\eta}\frac{dp}{dx}\right) = \frac{d}{dx}\left(\tilde{V}h\right). \tag{3.33}$$

Then, the pressure distribution can be determined, provided the boundary conditions

$$p(x=0) = p_a \tag{3.34a}$$
$$p(x=L) = p_b \tag{3.34b}$$

are given.

3.2 VEHL conformal problem: polymer journal bearing

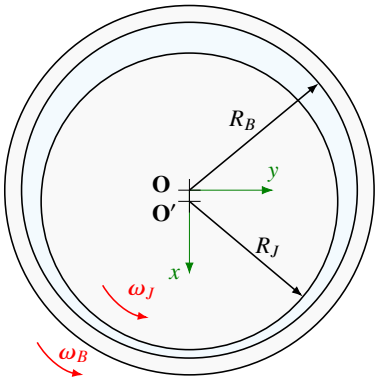

Figure 3.3: Schematic of the journal bearing.

As previously mentioned in the introduction of this Chapter, journal bearings are commonly used in various subsystems in engines and power trains, such as for crankshaft and camshaft: the piston pin-bore bearing and the big-end bearings are just possible examples [103, 104]. These components are also critical in the aerospace industry, in the rocker shaft of rocker-arm valve train systems, or in industrial turbines for power generation [105]. Hence, researchers worldwide made significant efforts to reach a comprehensive understanding of the journal bearings performances under different operating conditions [67, 102, 106–109]. The theoretical analyses of the elastic distortion of journal bearings were motivated by the experimental work of Carl [110], who was able to investigate the impact of elastic deformations, i.e., the cavitation angle rises, the pressure peak falls, and the minimum film thickness point shifts toward the maximum pressure location. Higginson [111] analyzed the conditions in a journal bearing with a thin elastic layer, but the simplified treatment of the elastic problem, assuming the distortions to be proportional to the locally applied pressure, led to notable discrepancies with the actual bearing performances. The latter were addressed by Donoghue et al. in Ref. [112], where the authors provided an effective approach to the elastohydrodynamic problem for an infinitely long journal bearing in the presence of an isoviscous fluid, achieving extremely good agreement with experimental results [110]. The problem of the compliant journal bearing was also investigated by Benjamin and Castelli [113], who faced the elastic problem with different methods, while Hooke and Donoghue [114] assessed the EHL problem of soft materials, observing, for an elastomer lined journal bearing, deviations of the pressure distribution from the Hertzian solution as the eccentricity ratio is increased: the film thickness becomes negligible with respect to the deformation of the soft surface. Furthermore, relevant studies were carried out by Oh and Huebner [115], who further explored the lubrication of a finite-length flexible bearing using a finite-element technique, and by Conway et al. in Refs. [116–118]. In particular, in Ref. [116], the authors investigated the elasticity effect in an infinitely long bearing, assuming, at first, that the lubricant is isoviscous and, then, extending the investigation to the case of a pressure-dependent viscosity. In addition, as made by Higginson [111], the authors made the hypothesis that the radial deformation linearly depends on the pressure distribution. On the other hand, in Ref. [117], the lubrication of a long, porous, deformable journal bearing was also investigated: the response of the bearing, provided the bearing shell thickness to be much smaller than the peripheral length of the bearing, has been modeled

as a Winkler foundation. In Ref. [118], the same approach has been used to assess the performance of a short flexible journal bearing. Furthermore, Profito [119] proposed a Finite Volume Method based on Elements (FVMbE) scheme to assess statically loaded journal bearing, with particular attention to the case of a typical internal combustion engine connecting rod big-end bearing.

Crucially, this huge variety of theoretical and numerical efforts to fully understand the response of journal bearings has focused on linear elasticity: however, due to the encroaching role of polymers in the present and coming industrial panorama, special attention to soft lubrication involving polymer-based materials is needed. To this regard, several experimental campaigns have been carried out and particular attention has been paid to water-lubricated rubber journal bearings. Indeed, with respect to oil-lubricated metal bearings, they can reduce the consumption of lubricating oil and, nonetheless, friction, wear, and noise. Moreover, these bearings can accommodate misalignments and are easy to maintain, due to their simple structure. These advantages explain why water-lubricated bearings are now commonly used in several rotating machineries, such as in military crafts propulsion systems [120–122].

The level of theoretical understanding for polymer journal bearings and for the related frictional performances is, however, still insufficient: in particular, a clear assessment of the role played by the viscoelastic rheology associated to the soft bodies is still missing. Indeed, recent theoretical investigations [98, 99] have shown the existence of a peculiar viscoelastic-hydrodynamic lubrication (VEHL) regime, where solid viscoelasticity determines a marked difference, in terms of pressure, film thickness and ultimately friction, compared to classic EHL. This has to be properly evaluated also for journal bearings. Thus, in this thesis, particular attention is paid on the infinitely long polymer journal bearing (see Figure 3.3). In particular, our goal is to understand the role of viscoelastic rheology in the steady-state operations of the bearing. The present methodology paves over the mathematical formulation introduced Section 2.1 for conforming and non-conforming surfaces, where *ad-hoc* Green's function for the dry contact between a rigid pin, rolling about the center of an infinite viscoelastic holed space. Specifically, the Green's function takes into account the circular characteristic of the contact domain. Hence, here we develop a Boundary Element Method (BEM) to numerically assess the lubricated contact in a journal bearing. Importantly, as it will be shown later, the definition of such Green's function is crucial: in fact, the employment of the classical half-plane Green's function [22,67,73] would lead to misleading solutions in terms of film thickness and pressure distribution, thus in terms of the bearing capacity and behavior of the system. Furthermore, it should be noted that the development of such BE techniques results in significantly lower computing complexity when compared to Finite Element approaches. This exacerbates when multiple scales are considered in the analysis [123].

The following results for the polymer journal bearing enlighten the importance of viscoelasticity on the bearing performances. Three different configurations are investigated. In the hard-on-soft configuration (HS) the shaft is assumed to be rigid and the bearing is soft. In the soft-on-hard configuration (SH), the shaft is soft and the bearing is rigid, and, finally, in the soft-on-soft configuration (SS) both the interacting pair are soft. Hence, we focus on the pressure and film thickness distributions, in the case of a hard-on-soft configuration, when the journal rotating speed is increased while keeping the angular speed of the bearing constant, showing how the coupling between solid viscoelasticity and fluid viscous losses significantly affects the bearing response.

3.2.1 Problem formulation

Lubricated contacts involving deformable bodies are characterized by a strong coupling between the elastic, or viscoelastic, problem governing the deformation of the bodies and the Reynolds equations. Specifically, the deformation experienced by the bodies is governed by the pressure distribution, which is the solution of the Reynolds equations. The latter is determined by the lubricating film thickness, which intrinsically takes into account the displacement field of the interacting pair.

Thus, let us focus on the contact problem under analysis and determine the bearing response under steady-state operating conditions. We move from the mathematical formulation presented in Section 2.1. This methodology paves over the definition of the Green's function, which properly captures the nature of the circular contact domain.

Now, under the assumptions that the solids are homogeneous and the viscoelastic properties do not show any spatial dependency, recalling that the system is rotationally invariant and the elastic-viscoelastic correspondence principle, we can express, through Equation (2.10), the relationship between the radial displacement u_r and a purely radial stress σ_r in a polar reference frame, i.e.:

$$u_r(S) = \int_0^{2\pi R} dS'\, \mathcal{G}_{rr}(S - S', \omega)\, \sigma_r(S'), \tag{3.35}$$

with ω being the velocity of the contact patch, $S = s - \omega R t$ and $S' = s' - \omega R t$. Recall that $\mathcal{G}_{rr}(S)$ is the so-called viscoelastic steady-state Green's function, given by Equation (2.14).

Then, making use of Equation (3.35), we can specify the displacement field for the bearing profile as:

$$u_r^B(S) = \int_0^{2\pi R_B} dS'\, \mathcal{G}_{rr}^B(S - S', \bar{\omega}_B)\, \sigma_r(S'), \tag{3.36}$$

where $\bar{\omega}_B$ denotes the velocity of the contact patch at the bearing interface.

$\mathcal{G}_{rr}^B$ is determined by substituting $G_{rr}(S)$ in the expression of the viscoelastic Green's function with the following expression:

$$G_{rr}^B(s) = \frac{1+\nu}{2\pi}\left[-\frac{\kappa}{\kappa+1}(2\log R_B + 1)\cos\theta - \frac{\kappa+1}{2}\mathrm{B}(\theta)\cos\theta + (\kappa-1)\mathrm{A}(\theta)\sin\theta\right], \tag{3.37}$$

with $\theta = s/R_B$ being the angle subtended by the arc s. More details about the derivation of the spatial Green's function in Equation (3.37) can be found in Appendix A.2.

On the other hand, the journal displacement field is described by:

$$u_r^J(S) = \int_0^{2\pi R_J} dS'\, \mathcal{G}_{rr}^J(S - S', \bar{\omega}_J)\, \sigma_r(S'), \tag{3.38}$$

in which $\bar{\omega}_J$ is the velocity of the contact patch at the journal interface.

Now, $\mathcal{G}_{rr}^J$ is determined by setting $G_{rr}(S)$ in the expression of the viscoelastic Green's function as:

$$G_{rr}^J(s) = \frac{1+\nu}{2\pi}\left[\frac{1-(\kappa^2+1)\log R_J}{\kappa+1}\cos\phi - \cos\phi - \frac{\kappa+1}{2}(\kappa-1)\mathrm{A}'(\phi)\sin\phi - \frac{\kappa+1}{2}\mathrm{B}(\phi)\cos\phi\right], \tag{3.39}$$

in which $\phi = s/R_J$. The detailed derivation of $G^J_{rr}(s)$ can be found in Appendix A.3.

Hence, to numerically solve the contact problem, we adopt the numerical scheme proposed in Section 2.1 and in Ref. [22]: the contact domain is discretized with N elements, each covering an arc of length $2\alpha R$, and together with the assumption the discretization step is small enough to consider the stress σ_k constant and equal to $\sigma_k = \sigma_r(S_k)$, we can write the displacement of the i-th interval as $\{u_i\} = [\mathcal{L}_{ik}(\omega)]\{\sigma_k\}$. Therefore, it is possible to rephrase Equations (3.36) and (3.38) as the following linear systems:

$$\{u_i^B\} = [\mathcal{L}^B_{ik}(\bar{\omega}_B)]\{\sigma_k\} \tag{3.40a}$$

$$\{u_i^J\} = [\mathcal{L}^J_{ik}(\bar{\omega}_J)]\{\sigma_k\} \tag{3.40b}$$

Furthermore, the intercorrelation matrix elements $\mathcal{L}_{ik}$ are defined as $\mathcal{L}_{ik} = \mathcal{L}_{rr}\left(S_i - S_k, \omega\right)$, and $\mathcal{L}_{rr}(S)$ is given by Equation (2.16).

Once the system of linear equations governing the solid viscoelastic problem is set, we can focus on the equations governing the fluid dynamics of the system. To this regard, considering isoviscous fluids, and assuming no-slip boundary conditions at both solids interface, the Reynolds equations in a polar reference frame can be written as [67,94,124]:

$$\frac{\partial}{\partial s}\left(h^3\frac{\partial p}{\partial s}\right) = 12\tilde{\mathbf{v}}\eta\frac{\partial h}{\partial s}, \tag{3.41}$$

where $\tilde{\mathbf{v}}$ is the entrainment speed, computed as the average of the peripheral velocities of the surfaces, namely $\tilde{\mathbf{v}} = (\mathbf{v}_B + \mathbf{v}_J)/2$, in which $\mathbf{v}_B$ and $\mathbf{v}_J$ denote the peripheral velocity of a generic point on the bearing and on the shaft respectively, namely $\mathbf{v}_B(\theta) = \boldsymbol{\omega}_B \wedge (\mathbf{P}_B(\theta) - \mathbf{O})$ and $\mathbf{v}_J(\theta) = \boldsymbol{\omega}_J \wedge (\mathbf{P}_J(\theta) - \mathbf{O}')$. Moreover, h is the film thickness, and η is the fluid viscosity. Specifically, the normal displacement of the interacting pair profiles strongly affects the film thickness distribution. Indeed, we have that $h(\theta) = h_0 + g_0(\theta) + u_r^B(\theta) - u_r^J(\theta)$, with h_0 and $g_0(\theta)$ being respectively the central film thickness and the gap between the surfaces of the bodies in the undeformed configuration. For the system under analysis, that is the journal bearing, $g_0(\theta) = c(1 - \epsilon\cos(\theta))$ [67,78], where c is the bearing radial clearance, i.e. $c = R_B - R_J$, and ϵ is the eccentricity ratio, that is equal to $\epsilon = e/c$, with e being the eccentricity, which is equal to $e = |\mathbf{O}' - \mathbf{O}|$. As shown in Ref. [67], the previous definition of $g_0(\theta)$ holds for highly conforming profiles, i.e. for very small e/R_B ratios. When this condition is not met, a proper definition of the separation g_0 is needed. In addition, to take into account hydrodynamic cavitation in the divergent section, where the lubricant is subject to a tensile stress situation, Reynolds boundary conditions [67] are employed. Then, Equation (3.41) is attacked by implementing a finite difference scheme [67, 94], thus obtaining the following vector equation:

$$h_i = R_{ik}(\tilde{\mathbf{v}}, \eta)\sigma_k. \tag{3.42}$$

Thus, to assess the contact problem, we need to couple the solid mechanics and the fluid dynamics [26, 67, 94, 96] to determine the pressure distribution satisfying, at the same time, both Equation (3.40) and Equation (3.42). Specifically, an iterative scheme, underrelaxed with the Aitken acceleration approach [94,125] is implemented: at each iteration, moving from the film thickness estimation $\tilde{h}_n$, computed at the previous step, an estimated stress field $\tilde{\sigma}_k$ is obtained by inverting Equation (3.42), and the new displacement field can be determined from Equation (3.40); ultimately, the film thickness $\tilde{h}_{n+1}$ for the following iteration can be computed and the iterative process keeps on running until the pressure distribution numerically converges in two consecutive iterations.

Ultimately, it is possible to focus our analysis to the friction losses, which can be determined as the combination of the viscoelastic hysteretic dissipation and the fluid losses [67]. Specifically, for each body, we can determine the net force and the total torque respectively as:

$$\mathbf{F}_{tot} = \mathbf{F}_n + \mathbf{F}_\tau = R\left[\int_0^{2\pi} d\theta\, p(\theta)\mathbf{n}(\theta) + \int_0^{2\pi} d\theta\, \tau(\theta)\mathbf{t}(\theta)\right], \tag{3.43}$$

and

$$\mathbf{C}_t = R\int_0^{2\pi} d\theta\, (\mathbf{P}(\theta) - \mathbf{O}) \wedge (p(\theta)\mathbf{n}(\theta) + \tau(\theta)\mathbf{t}(\theta)), \tag{3.44}$$

where $\mathbf{P}(\theta)$ is the point of the deformed profile at angular position θ, and $\mathbf{O}$ is the center of the bearing, which is coincident with the origin of the reference frame adopted (see Figure 3.3). Moreover, $\mathbf{n}(\theta)$ and $\mathbf{t}(\theta)$ are the unit vectors, respectively normal and tangential to the deformed contour; ultimately, the viscous shear stresses τ acting on the bearing surface, i.e. $\tau = \tau_B$, and on the journal surface, i.e. $\tau = \tau_J$, are obtained as [67]:

$$\tau_B(\theta) = -\frac{h}{2R_B}\frac{\partial p}{\partial \theta} - \frac{\eta(\mathbf{v}_B(\theta) - \mathbf{v}_J(\theta))}{h}, \tag{3.45a}$$

$$\tau_J(\theta) = -\frac{h}{2R_J}\frac{\partial p}{\partial \theta} + \frac{\eta(\mathbf{v}_B(\theta) - \mathbf{v}_J(\theta))}{h}. \tag{3.45b}$$

Finally, it is of particular interest to quantify the viscoelastic contribution to friction. Specifically, it is possible to compute the power related to viscoelastic dissipation $P_{v,d}$, which is equal to:

$$P_{v,d} = \omega R\int_0^{2\pi} d\theta\, p(\theta)\frac{\partial u_r(\theta)}{\partial \theta}. \tag{3.46}$$

3.2.2 Results and discussion

In this Section, in order to point out the implications of the approach previously developed, we consider a journal bearing operating in steady-state conditions, where the bearing has a radius equal to $R_B = 0.1\,\mathrm{m}$, and the radial clearance c is equal to $c = R_B - R_J = 5 \cdot 10^{-4}\,\mathrm{m}$. In the following analysis, when we refer to soft solids, we employ a single relaxation time material with glassy modulus $E_\infty = 100\,\mathrm{MPa}$, $E_\infty/E_0 = 100$, and relaxation time $\tau = 1\,\mathrm{s}$.

As a first step, we investigate a classic Elastohydrodynamic lubrication (EHL) problem: the journal is rigid and the bearing is elastic with elastic modulus being equal to the rubbery modulus E_0, and Poisson's ratio $\nu = 0.5$, while the fluid is isoviscous with a viscosity η being equal to $\eta = 0.001\,\mathrm{Pa}\cdot\mathrm{s}$. As pointed out in Figure 3.4 for a dimensionless net force $\tilde{F}_{tot} = |\mathbf{F}_{tot}|/E_0 R_B = 2.2 \cdot 10^{-3}$, the solution in terms of dimensionless film thickness and pressure distributions (solid lines), defined respectively as $\tilde{h} = h/c$ and $\tilde{p} = p/E_0$, is completely different from what we would obtain by solving the classical non-conformal EHL problem, that is, by employing the usual half-plane Green's function to compute the elastic deformation of the solids [66,73,126] (dashed lines). Crucially, we can conclude that the half-plane approximation is not suitable for lubricated conformal contact problems and justify the necessity of developing a numerical method properly tuned. This aspect is of the utmost importance when the bearing response is analyzed, and it must be carefully taken into account in design processes.

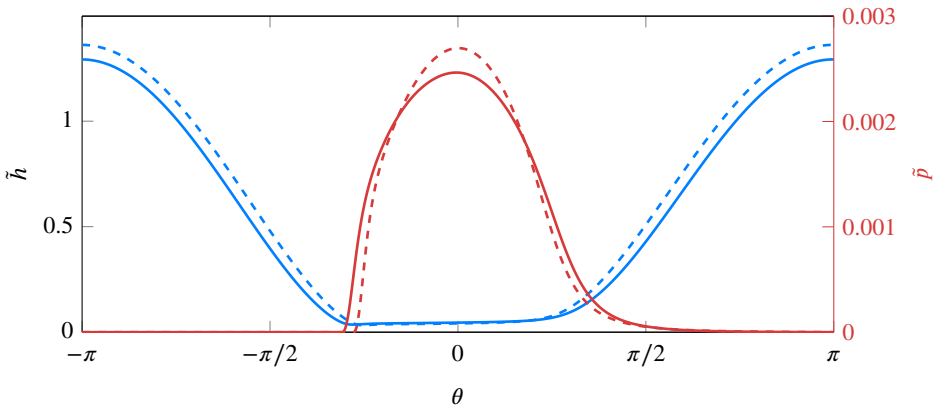

Figure 3.4: The dimensionless film thickness $\tilde{h} = h/c$ (blue) and pressure $\tilde{p} = p/E_0$ (red) distributions for a fixed value of the dimensionless resultant force $\tilde{F}_{tot} = |\mathbf{F}_{tot}|/E_0 R_B = 2.2 \cdot 10^{-3}$. The numerical predictions are carried out in EHL regime, where the journal is rigid and the bearing is elastic, with elastic modulus $E = 1\,\mathrm{MPa}$ and Poisson's ratio $\nu = 0.5$, and compared with the solution obtained using the half-plane Green's function (dashed lines).

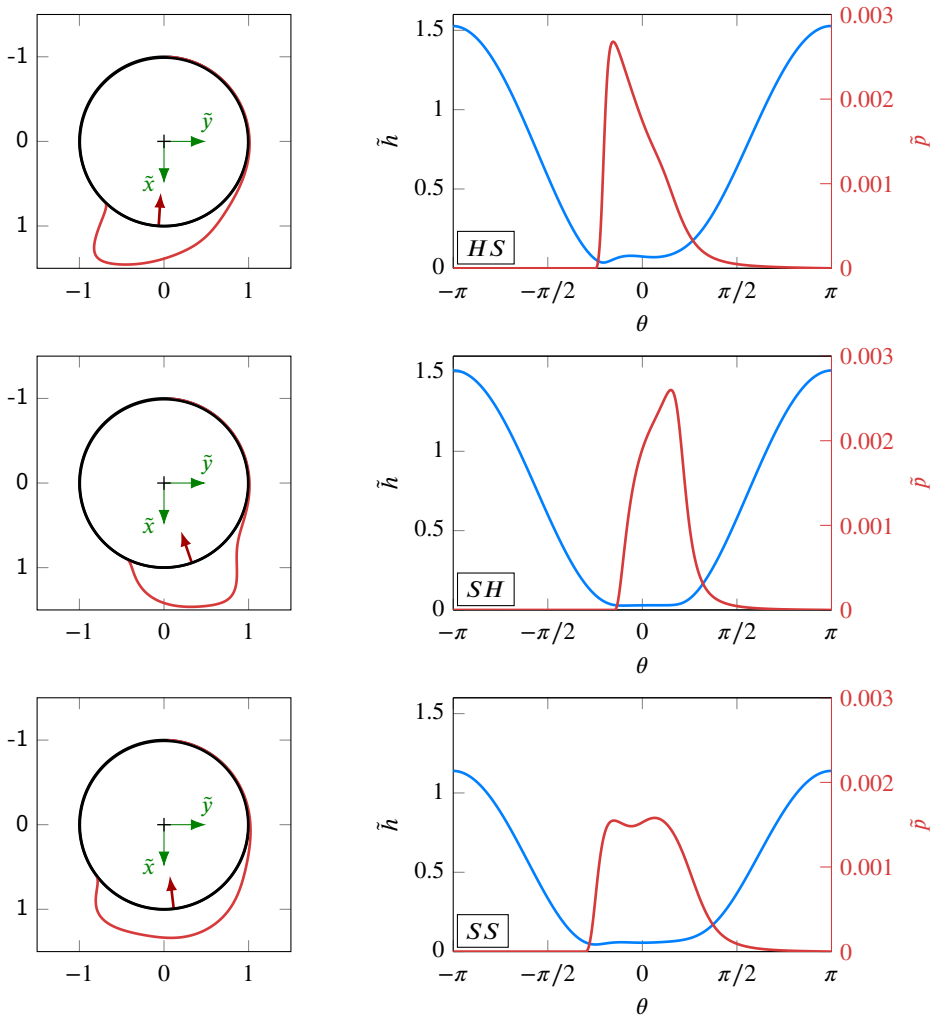

Figure 3.5: The deformed profile (solid black line), the pressure distribution (solid red line) and the resulting net force $\mathbf{F}_{net}$ (red arrow) on the left; the dimensionless film thickness $\tilde{h} = h/c$ (solid blue line) and the dimensionless pressure $\tilde{p} = p/E_0$ (solid red line) distributions on the right. The results are carried out for a fixed value of the Hersey number $H = -4.5e-9$ and three different configurations: hard-on-soft (HS), soft-on-hard (SH) and soft-on-soft (SS), with $\tilde{\omega}_B = 0.2$ and $\tilde{\omega}_J = -0.4$. The axes $\tilde{x}$ and $\tilde{y}$ refer to the normalized x- and y-coordinates, i.e., $\tilde{x} = x/R_B$ and $\tilde{y} = y/R_B$.

Now, we can focus on the analysis of the viscoelasticity effects for a polymer journal bearing. In particular, we investigate three different contact conditions: rigid journal on soft bearing liner (HS), soft journal on rigid bearing liner (SH), and soft journal on soft bearing liner (SS). As shown in Figure 3.5, the pressure and film thickness distributions are dramatically affected by the choice of material pairing: it is thus clear that viscoelasticity plays a pivotal role. Crucially, this leads to a different attitude angle of the resulting force (red arrows in Figure 3.5), i.e. the angle the net force generates with respect to the line of centers [67], and, ultimately, on the angular position of the application point. Clearly, such a variation in the resultant force has important consequences on the rotor dynamics of the entire system where the bearing is applied. Calculations are carried out for dimensionless speeds for the bodies being respectively

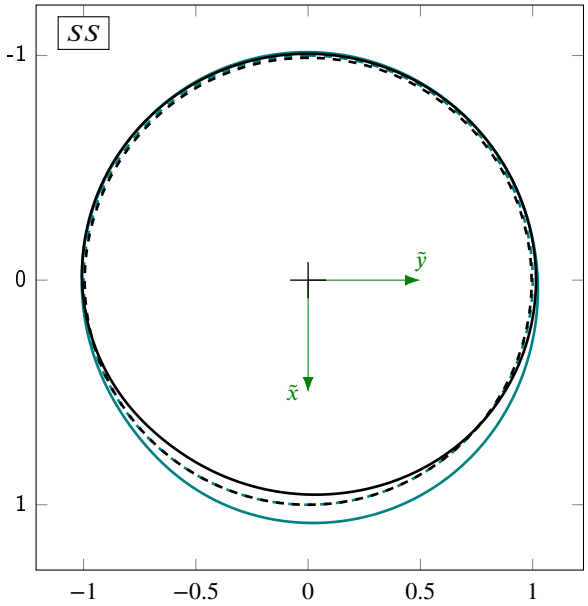

Figure 3.6: The undeformed (dashed lines) and the magnified deformed (solid lines) contours of the journal (black) and the bearing (teal), with $K = 50$ being the magnification factor. The calculations are carried out for a soft-on-soft (SS) configuration, with a fixed value of the Hersey number $H = -4.5e-9$, and $\tilde{\omega}_B = 0.2$ and $\tilde{\omega}_J = -0.4$. The axes $\tilde{x}$ and $\tilde{y}$ refer to the normalized x- and y-coordinates, i.e., $\tilde{x} = x/R_B$ and $\tilde{y} = y/R_B$.

equal to $\tilde{\omega}_B = \omega_B \tau = 0.2$ and $\tilde{\omega}_J = \omega_J \tau = -0.4$, while keeping the dimensionless resultant force $\tilde{F}_{tot}$ constant and equal to $\tilde{F}_{tot} = 2.2 \cdot 10^{-3}$: the Hersey parameter H is then equal to $H = \eta \tilde{\mathrm{v}} R_B / |\mathbf{F}_{tot}| = -4.5e-9$. Thus, starting with the HS configuration, we observe a clear peak in the pressure distribution at the leading edge due to solid viscoelasticity. Incidentally, the leading edge of the solid contact corresponds to the flow outlet, i.e. where the lubricant exits the lubricated contact. Here, we find a minimum in the film thickness, due to both flow conservation and the viscous resistance against the instantaneous change of deformation.

When we consider the SH case, we retrieve a very different outcome. Now, the bearing is rigid, while the journal is linearly viscoelastic and, coherently with the kinematics of the problem, we have that the fluid inlet, i.e. where the fluid is sucked in the contact, corresponds to the leading edge for the journal: hence, the peak in the pressure distribution. Finally, in the SS configuration, both the contacting pairs are linearly viscoelastic and, since the system is now more compliant, the contact region is now larger than that observed in the previous cases. Furthermore, looking at the pressure distribution, it is possible to notice two peaks at the inlet and at the outlet of the contact zone, corresponding to the leading edges of the journal and the bearing respectively. To this regard, the reader should observe that, for each viscoelastic body, the leading edge is the region where the contact is initiated and where a larger stiffness and, thus, a larger pressure are shown [22]. Indeed, as Figure 3.6 shows for the latter case, which refers to a soft journal on a soft bearing, the location of the leading regions can be elicited from superposing the undeformed contours (dashed lines) and the deformed contours (solid lines) of the bodies: the region where the deformed profile, magnified to improve the readability of the figure, is closer to the undeformed contour corresponds to the leading

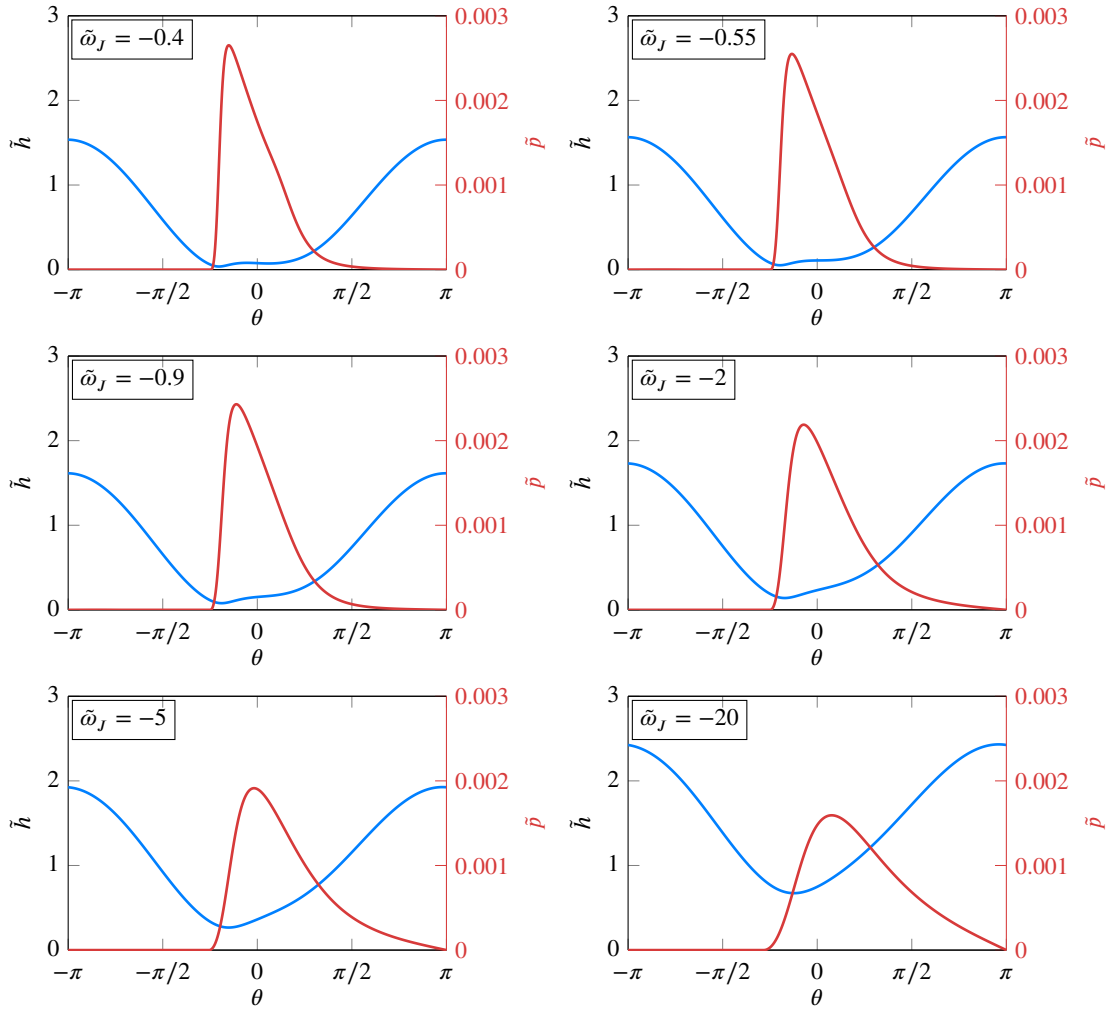

Figure 3.7: The dimensionless film thickness $\tilde{h} = h/c$ (solid blue line) and the dimensionless pressure $\tilde{p} = p/E_0$ (solid red line) distributions at different journal speed $\tilde{\omega}_J$ for a fixed value of the net force $\mathbf{F}_{tot}$. The calculations are carried out for a hard-on-soft (HS) configuration, and a fixed $\tilde{\omega}_B = 0.2$.

edge zone, while larger displacements are observed at the trailing edge, where the material is still relaxing upon the passage of the load. In fact, it is straightforward to find the leading region for the shaft (in black) at the fluid inlet, i.e. on the right, where the minimum deviation between deformed and undeformed profile occurs; on the contrary, for the bearing (in green) this condition is met at the fluid outlet, while large deviations between the actual (deformed) and the reference (undeformed) profiles are retrieved at the fluid inlet, which corresponds to the trailing edge. Hence it is clear that, in viscoelastic lubricated contacts, besides the Hersey number H, the dimensionless speeds of the interacting pair, i.e. $\tilde{\omega}_B$ and $\tilde{\omega}_J$, are fundamental in governing the response of the system, since they capture the complex rheology of such materials.

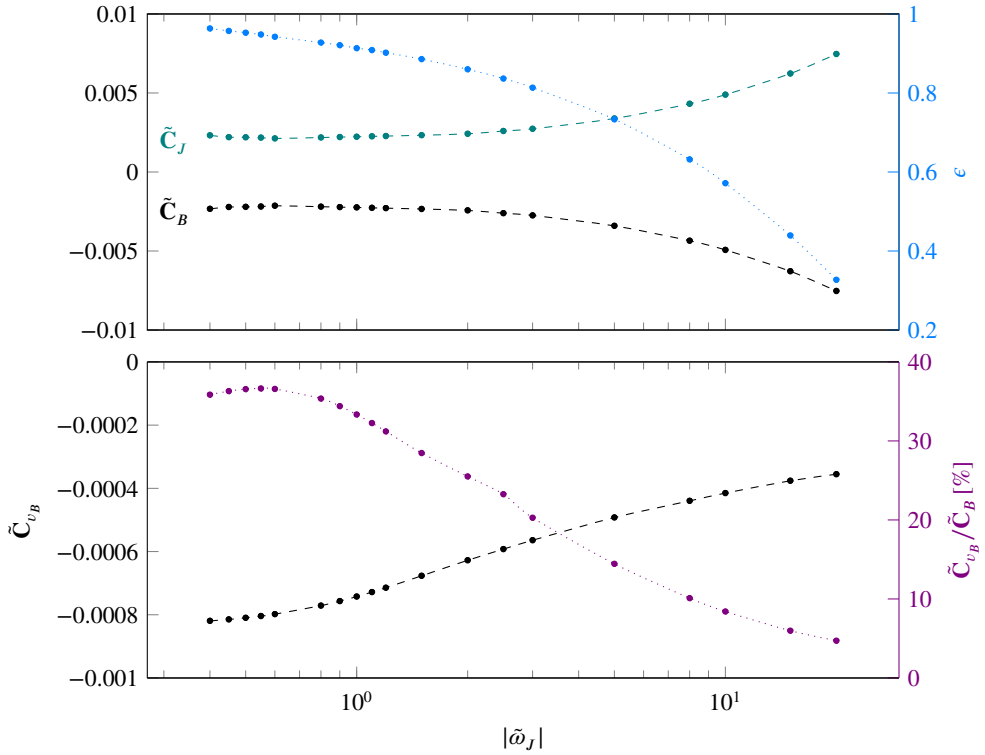

Figure 3.8: In the graph above, the dimensionless friction torque for the journal $\tilde{\mathbf{C}}_J = \mathbf{C}_J/|\mathbf{F}_{tot}|R_B$ (green curve), for the bearing $\tilde{\mathbf{C}}_B = \mathbf{C}_B/|\mathbf{F}_{tot}|R_B$ (in black) on the left y-axis; on the right y-axis, the eccentricity ratio ϵ. Below, the viscoelastic contribution to total resisting torque for the bearing $\tilde{\mathbf{C}}_{v,B} = \mathbf{C}_{v,B}/|\mathbf{F}_{tot}|R_B$ (in black) on the left y-axis; the ratio $\tilde{\mathbf{C}}_{v,B}/\mathbf{C}_B\,[\%]$ on the right y-axis. The results are carried out for a hard-on-soft (HS) configuration and fixed value of the net force $\mathbf{F}_{tot}$, at different journal dimensionless speed $\tilde{\omega}_J$, and $\tilde{\omega}_B = 0.2$.

Now, it is interesting to study the system response when the absolute value of the shaft angular speed $|\tilde{\omega}_J|$ increases, while keeping fixed the total load $\tilde{F}_{tot} = 2.2 \cdot 10^{-3}$ and the bearing angular speed $\tilde{\omega}_B = 0.2$. Specifically, we focus on a hard-on-soft (HS) configuration, where the shaft is considered rigid, while the bearing liner is linearly viscoelastic. Crucially, the impact of viscoelasticity effects on the bearing performance is quite evident, as shown in Figure 3.7. A clear asymmetry in the pressure distribution occurs due to the different relaxation between leading and trailing edges; in particular, the leading edge for the bearing is located at the fluid outlet, where a peak in the pressure distribution and, correspondingly, a minimum in the film thickness distribution are retrieved. As soon as we increase the shaft angular velocity, the fluid load-bearing capacity increases since more lubricant is *entrained* in the lubricated contact zone. Hence, the reduced values of the maximum pressure and the very peculiar film thickness distributions, the latter characterized by increasing values of the central film thickness h_0, and by a certain degree of asymmetry related to the viscoelastic response of the bearing material. Ultimately, the upper graph in Figure 3.8 presents, on the left y-axis, the dimensionless resisting torque for the bearing , i.e. $\tilde{\mathbf{C}}_B = \mathbf{C}_B/|\mathbf{F}_{tot}|R_B$, and for the journal, i.e. $\tilde{\mathbf{C}}_J = \mathbf{C}_J/|\mathbf{F}_{tot}|R_B$, computed as presented in Section 3.2.1 with respect to bearing center $\mathbf{O}$. Incidentally, it is of particular interest to highlight the viscoelastic

contribution to the resisting torque for the bearing, i.e. $\tilde{\mathbf{C}}_{v,B} = \mathbf{C}_{v,B}/|\mathbf{F}_{tot}|R_B$, directly obtained by the computation of the power related to the viscoelastic dissipation (see Equation (3.46)): it is evident how the viscoelastic contribution to the overall bearing torque is important, especially at low shaft speeds, where we retrieve $\tilde{\mathbf{C}}_{v,B}/\mathbf{C}_B \approx 35\%$. Indeed, as discussed beforehand, the higher the entrainment speed the higher the load-bearing capacity of the lubricant, hence the lower levels of deformation of the bearing liner and, consequently, the lower energy dissipation. Furthermore, on the right y-axis of the former graph, the eccentricity ratio ϵ as a function of the angular speed of the shaft $|\tilde{\omega}_J|$ is depicted. In particular, it can be noticed that it follows a monotonic trend and, coherently with an increasing lubricant entrainment in the lubricated contact zone, we have higher values of the central fluid film thickness, thus lower values of the eccentricity ratio.

Conclusions

In this thesis, an innovative Boundary Element methodology has been developed to investigate two-dimensional steady-state viscoelastic conformal and non-conformal contacts. These are of the utmost importance as found in a variety of conditions, including, for example, industrial applications, like pin-joints and rolling element bearings, or biomechanical systems, like hip joints. The formulation, which is fully general and able to deal with real viscoelastic materials, is based on a properly defined steady-state viscoelastic Green's function. At first, in order to show the peculiar features of the methodology, attention is paid on a simple yet paradigmatic conformal contact, that is, the contact of a pin in a bushing. In this case, the methodology has been validated in the elastic limit against the analytical solution in literature [34], showing a very good agreement. Then, the analysis has proceeded with the case of a linearly viscoelastic bushing. Numerical calculations have been performed for a single relaxation time material and have shown how viscoelastic effects clearly determines the response of the system at intermediate speeds, where a certain degree of asymmetry in the pressure and displacement distribution can be observed. This has dramatic consequences on the net force, which is tilted of a certain angle with respect to the load line, thus generating a resisting torque around the pin center. On the other hand, at very low and very high speeds the system behaves as elastic and symmetric solutions are retrieved, and the resisting torque is clearly null.

Hence, given the generality of the approach, it has been employed to numerically investigate the steady-state operation of a rolling element bearing, characterized by rigid rolling elements and deformable linearly viscoelastic rings. The system reduces to the solution of two contact problems: one deals with the contact of each roller with the inner ring, the other refers to the contact of the roller with the outer raceway. The closing condition to correlate the two contact aspects of the bearing mechanics is found by imposing the force balance on all the rolling elements. First, numerical calculations have been carried out on a single relaxation time material to show, in a paradigmatic form, the effect of viscoelasticity in this particular application. Specifically, when looking at the distributions of pressure and displacements, at very low speeds and very high speeds, where the material enters the rubbery and glassy region respectively, we have a symmetric Hertzian-like solution for each roller in contact, while, at intermediate speeds, we retrieve asymmetric distributions due to viscoelastic energy dissipation occurring in the material. In particular, the material needs time to recover from its deformed state at the trailing edge of each contact zone, resulting in larger displacements. For the same reason, i.e. the viscous resistance against the instantaneous change of deformation, a pressure peak occurs at the leading edge of each contact zone. Moreover, for kinematic reasons, the leading and the trailing edges are opposite in the inner and the outer rings, thus combining in a very peculiar way. As a consequence, there exists a viscoelasticity-induced radial clearance at intermediate speeds: this significantly affects the bearing

load distribution. Indeed, unlikely what happens in the elastic case, although placed for geometric reasons in the load zone, some of the rolling elements do not participate in the contact. This should be carefully accounted for when studying the dynamics of the bearing. To this extent, it should be noticed that this aspect of the bearing response depends on the global load: at higher loads, there is a larger energy dissipation, due to the hysteretic behavior of the material, and, thus, the overall distribution of the load among the rollers may change. Furthermore, this can be seen also when looking at the friction curves and, specifically, at the viscoelastic torque: when increasing the load, larger friction is obtained, while a shift toward higher frequencies of the viscoelastic friction peak is observed.

As the formulation is able to deal with real viscoelastic materials with a continuous spectrum of relaxation times, our approach has been experimentally validated by comparing the numerical predictions of the viscoelastic friction torque, with the outcomes of the tests performed on a tribometer specifically designed to account for measuring the friction torque in a bearing. The agreement observed is good, provided the complexity of the measurement and the presence of other sources of dissipation. This confirms the capability of our formulation.

Ultimately, the integral formulation has been employed to assess the lubricated contact problem of a polymer journal bearing operating in steady-state conditions. Crucially, the aim of this study has been to highlight how viscoelasticity strongly affects the quantities that characterize the bearing performances, such as pressure, film thickness, and friction. Incidentally, it is shown that a proper definition of the Green's functions is needed. In order to highlight that, the journal bearing operations in elasto-hydrodynamic lubrication (EHL) regime has been analyzed: the shaft is considered rigid, and the bearing liner is elastic. From the comparison of the distributions of the fluid film thickness and the pressure, with those obtained by employing the half-plane Green's function, considerable deviations have been observed, showing that the half-plane approximation is not suitable to study such a conforming circular contact problem. Then, it has been underlined how the contact configuration is critical in determining the system response. Three different configurations have been considered, respectively the hard-on-soft configuration (HS), in which the shaft is rigid and the bearing is linearly viscoelastic, soft-on-hard configuration (SH), in which the shaft is linearly viscoelastic and the bearing is rigid, and the soft-on-soft configuration (SS), where both the solids are linearly viscoelastic: dramatic changes are retrieved in the pressure and fluid film thickness distributions, thus on friction. In particular, the HS case has been further investigated, for a fixed value of the net force $\tilde{F}_{tot}$ and a constant angular speed of the bearing $\tilde{\omega}_B$, while increasing the absolute value of the angular speed of the shaft $|\tilde{\omega}_J|$, showing the significant impact of the complex rheology of the viscoelastic bearing on the system behavior and, crucially, on friction. The latter is the result of the combination between fluid viscous losses and the viscoelastic hysteretic term. Thus, the resisting torque for the bearing and the shaft are presented: for increasing values of the shaft angular velocity, higher values of the friction torque are obtained; conversely, we notice that the higher the shaft speed, the lower the eccentricity ratio. This is due to higher values of the central film thickness, as more fluid is entrained in the lubricated contact region.

Incidentally, the power dissipation related to the hysteretic behavior of the viscoelastic material is also quantified. This, in turn, has allowed us to quantify the contribution of the viscoelastic torque to the overall friction torque of the bearing. In particular,

it has been observed that this contribution diminishes as the speed of the journal is increased, leading to higher values of the entrainment speed. This result is due to the lower deformation experienced by the material as the capacity of the lubricant to sustain the load increases.

Ultimately, the results presented in this study underline that, in order to completely assess visco-elastohydrodynamic lubrication (VEHL) problems, the Hersey number is not the only parameter governing the system response, but the dimensionless speeds of the viscoelastic bodies, i.e. $\tilde{\omega}_B$ and $\tilde{\omega}_J$, have to be taken into account carefully, as they embody the complex rheology of the materials.

Incidentally, further investigations are ongoing to corroborate the numerical approach for the VEHL problem of a polymer journal bearing: tests are performed on a specific tribometer, that is the Precision Bearing Test Rig 2, at the Austrian Excellence Centre for Tribology (AC2T Gmbh), and the system response is analyzed, at various loads, for different lubricants and contact configurations. Hence, the comparison between the numerics and the experiments would shed light on the importance of the hysteretic behavior of soft materials in such industrial applications.

Furthermore, the Boundary Element methodology developed does not include frictional heating effects, and would be interesting to carry out the thermal analysis of the contact area. In fact, the knowledge of the temperature distribution in the contact zone would lead to understanding the impact of frictional heating at different rolling/sliding speeds, which is a key aspect to take into consideration in optimizing the components design. The simplest way to face this problem is to consider the mean temperature in the contact area. Clearly, thermal gradients, and hence, flash temperature effects are neglected, but this approach would not require important modifications of the methodology.

Appendix A

Elastic displacements in circular systems

A.1 Complex potentials theory

In this Appendix, we focus on the equations of the plane theory of elasticity when no body forces are present. In this case, the stresses can be expressed by means of one single auxiliary function, that is the so-called *Airy function*. In particular, the equilibrium equations $\boldsymbol{\nabla} \cdot \boldsymbol{\sigma} + \mathbf{f} = \mathbf{0}$, with $\mathbf{f}$ being the body-force vector, under the conditions considered, give :

$$\frac{\partial \sigma_x}{\partial x} + \frac{\partial \tau_{yx}}{\partial y} = 0, \tag{A.1a}$$

$$\frac{\partial \tau_{yx}}{\partial x} + \frac{\partial \sigma_y}{\partial y} = 0. \tag{A.1b}$$

Looking at the former, it is the necessary and sufficient condition for the existence of a function $A(x, y)$ such that $\partial A/\partial x = -\tau_{yx}$ and $\partial A/\partial y = \sigma_x$. The same reasoning holds for the second equation: there exists a function $B(x, y)$ such that $\partial B/\partial x = \sigma_y$ and $\partial B/\partial y = -\tau_{yx}$. Then, it follows that $\partial A/\partial x = \partial B/\partial y$, whence there exists a function $U(x, y)$, such that $A = \partial U/\partial y$ and $B = \partial U/\partial x$. Specifically, the function U is the aforementioned *Airy function*, also known as *stress function*, and allows to express the stresses as:

$$\sigma_x = \frac{\partial^2 U}{\partial x^2}, \qquad \sigma_y = \frac{\partial^2 U}{\partial y^2}, \qquad \tau_{yx} = -\frac{\partial^2 U}{\partial x \partial y}. \tag{A.2}$$

Furthermore, since the stress components are continuous and single-valued, with derivatives being continuous up to the second order, the function U must have continuous derivatives up to the fourth order and these derivatives, from the second order onwards, must be single-valued. Then, in absence of body force, it is known that the stress function has to satisfy the biharmonic equation, i.e. $\Delta^2 U = 0$, which solutions are the *biharmonic functions* [43]. In the following, the displacement components, u and v, are supposed to be single-valued, continuous, and related to the stress components by the subsequent relations:

$$\sigma_x = \lambda\delta + 2\mu\frac{\partial u}{\partial x}, \qquad \sigma_y = \lambda\delta + 2\mu\frac{\partial v}{\partial y}, \qquad \tau_{yx} = \mu\left(\frac{\partial v}{\partial x} + \frac{\partial u}{\partial y}\right), \tag{A.3}$$

where λ and μ are the first and second Lamé's constant respectively, and $\delta = \partial u/\partial x + \partial v/\partial y$.

Now, let us consider the region S, occupied by the body, to be simply connected, i.e. any cut joining any two points of its boundary divides it into individual regions; conversely, if cuts joining points of the boundary may be introduced without dividing it into separate parts, the region is said to be multiply connected. Combining Equations (A.2) and (A.3), and introducing the notation $P = \Delta U$, we find:

$$2\mu\frac{\partial u}{\partial x} = -\frac{\partial^2 U}{\partial x^2} + \frac{\lambda+2\mu}{2(\lambda+\mu)}P, \tag{A.4a}$$

$$2\mu\frac{\partial v}{\partial y} = -\frac{\partial^2 U}{\partial y^2} + \frac{\lambda+2\mu}{2(\lambda+\mu)}P, \tag{A.4b}$$

where it is clear that the function P is harmonic. As known from complex function theory, for any harmonic function it is possible to determine a function, conjugate to it. Let Q be the harmonic function, conjugate to P, hence satisfying the Cauchy-Riemann conditions, $\partial P/\partial x = \partial Q/\partial y$ and $\partial P/\partial y = -\partial Q/\partial x$. In particular, the function Q is equal to $Q(x,y) = \int_\gamma dQ + C$, with C being an arbitrary constant, γ an arbitrary path that does not leave the region S, and $dQ = -(\partial P/\partial y)dx + (\partial P/\partial x)dy$. Thus, we can introduce the function $f(z) = P(x,y) + iQ(x,y)$, where z is a complex variable defined as $z = x + iy$. Specifically, since the real functions P and Q have first derivatives related by the Cauchy Riemann conditions, $f(z)$ is holomorphic in the region S. Moreover, we can define the function $\varphi(z) = p + iq = (1/4)\int dz\, f(z) = \Omega(z)/4$ [43]. Hence, noting that $\varphi'(z) = \partial p/\partial x + i\partial q/\partial y = (1/4)(P+iQ)$, where the first derivatives of the functions p and q are related by the Cauchy Riemann conditions, we find that $P = 4\,\partial p/\partial x = 4\,\partial q/\partial y$, and $Q = 4\,\partial p/\partial y = -4\,\partial q/\partial x$. Finally, entering P into Equation (A.4) and integrating we obtain:

$$2\mu u = -\frac{\partial U}{\partial x} + \frac{2(\lambda+2\mu)}{\lambda+\mu}p + c_1(y), \tag{A.5a}$$

$$2\mu v = -\frac{\partial U}{\partial y} + \frac{2(\lambda+2\mu)}{\lambda+\mu}q + c_2(x), \tag{A.5b}$$

where $c_1(y)$ and $c_2(x)$ are the integration constants, and, specifically, represent rigid-body displacements. Thus, without any loss of generality, we can neglect these terms, and retrieve the same expressions found by Love [127]:

$$2\mu u = -\frac{\partial U}{\partial x} + \frac{2(\lambda+2\mu)}{\lambda+\mu}p, \tag{A.6a}$$

$$2\mu v = -\frac{\partial U}{\partial y} + \frac{2(\lambda+2\mu)}{\lambda+\mu}q. \tag{A.6b}$$

Then, it is straightforward to show that the function $U - px - qy$ is harmonic, that is $\Delta(U - px - qy) = 0$: hence we get $U = px + qy + p_1$, with p_1 being a harmonic function in the region occupied by the body. Introducing the function $\chi(z)$, the real part of which is p_1, we can then write the function U as:

$$U = \mathrm{Re}(\bar{z}\varphi(z) + \chi(z)), \tag{A.7}$$

with $\bar{z} = x - iy$ representing the complex conjugate value of z. Equation (A.7) can be also rephrased as:

$$2U = \overline{z}\varphi(z) + z\overline{\varphi(z)} + \chi(z) + \overline{\chi(z)}, \tag{A.8}$$

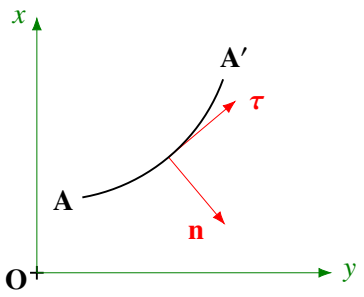

Figure A.1: Schematic of the unit vectors $\mathbf{n}$ and $\boldsymbol{\tau}$, respectively normal and tangential to the general element AA' (inspired by [43]).

and, consequently, the partial derivatives of U have direct physical meaning, we look for a function $f(x,y)$, defined as $f(x,y) = \partial U/\partial x + i\partial U/\partial y$. To come full circle, we have

$$2\frac{\partial U}{\partial x} = \varphi(z) + \overline{z}\varphi'(z) + \overline{\varphi(z)} + z\overline{\varphi'(z)} + \chi'(z) + \overline{\chi'(z)}, \tag{A.9a}$$

$$2\frac{\partial U}{\partial y} = i(-\varphi(z) + \overline{z}\varphi'(z) + \overline{\varphi(z)} - z\overline{\varphi'(z)} + \chi'(z) - \overline{\chi'(z)}), \tag{A.9b}$$

so that, making use of the identity $\psi(z) = \chi'(z)$, $f(x,y)$ is equal to:

$$f(x,y) = \frac{\partial U}{\partial x} + i\frac{\partial U}{\partial y} = \varphi(z) + z\overline{\varphi'(z)} + \overline{\psi(z)}. \tag{A.10}$$

Most importantly, notice that if the functions $\varphi(z)$ and $\chi(z)$ are holomorphic functions of z, Equation (A.8) is representative of a biharmonic function. Indeed, by adding the differentiation of (A.9a) with respect to the coordinate x, with that of (A.9b) with respect to the coordinate y, it can be shown that $\Delta U = P = 2(\varphi'(z)+\overline{\varphi'(z)}) = 4\mathrm{Re}(\varphi'(z))$, whence $\Delta\Delta U = 0$, since ΔU is a harmonic function, the latter being completely determined by the real part of the function $\varphi'(z)$.

Now, we can derive the complex representation of displacements and stresses. For this purpose, let us add Equation (A.5a) to Equation (A.5b), the latter multiplied by i, so that the complex displacement $\tilde{u} = u + iv$ can be computed as:

$$2\mu(u + iv) = \kappa\varphi(z) - z\overline{\varphi'(z)} - \overline{\psi(z)}, \tag{A.11}$$

where κ is the Kolosov's constant, which is equal to $\kappa = 3-4\nu$ in plane strain conditions, and $\kappa = (3-\nu)/(1+\nu)$ in generalized plane stress conditions. Recall that the first Lamé's constant λ has to be replaced by $\lambda^* = 2\lambda\mu/(\lambda+2\mu)$ for plane stress problems.

Next, let us obtain the expression of the stress components by means of the functions $\varphi(z)$ and $\psi(z)$. To this aim, with reference to Figure A.1, let us consider a general element ds AA', and a right-handed triplet $(\mathbf{n}, \boldsymbol{\tau}, \mathbf{k})$, with $\mathbf{n}$ and $\boldsymbol{\tau}$ being the unit vectors, respectively normal and tangential to the element under analysis. In particular, we can determine the projection of the resultant stress, acting on the normal unit vector $\mathbf{n}$, onto the Cartesian coordinates:

$$\sigma_{nx} = \boldsymbol{\sigma}\mathbf{n}\cdot\mathbf{i}, \tag{A.12a}$$

$$\sigma_{ny} = \boldsymbol{\sigma}\mathbf{n}\cdot\mathbf{j}, \tag{A.12b}$$

with **i** and **j** being the unit vectors of the $x-$ and $y-$axis respectively. Recalling the expressions of σ_x, σ_y, $\tau_{x,y}$ from Equation (A.2), and observing that $\mathbf{n}\cdot\mathbf{i} = dy/ds$, $\mathbf{n}\cdot\mathbf{y} = -dx/ds$, we obtain:

$$\sigma_{nx} = \frac{d}{ds}\left(\frac{\partial U}{\partial y}\right), \qquad \sigma_{ny} = -\frac{d}{ds}\left(\frac{\partial U}{\partial x}\right), \tag{A.13}$$

and, in complex form, together with the definition in Equation (A.10),

$$\sigma_{nx} + i\,\sigma_{ny} = -i\frac{d}{ds}\left(\varphi(z) + z\overline{\varphi'(z)} + \overline{\psi(z)}\right). \tag{A.14}$$

At first, consider the element $ds = dy$, that is the element is oriented along the $y-$axis. In this case, since $dz = i\,dy$, $\sigma_{nx} = \sigma_x$, $\sigma_{ny} = \tau_{yx}$, from Equation (A.14) we retrieve:

$$\sigma_x + i\,\tau_{yx} = \varphi'(z) + \overline{\varphi'(z)} - z\overline{\varphi''(z)} - \overline{\psi'(z)}. \tag{A.15}$$

Analogously, when the element is oriented along the $x-$axis, we obtain:

$$\sigma_y - i\,\tau_{yx} = \varphi'(z) + \overline{\varphi'(z)} + z\overline{\varphi''(z)} + \overline{\psi'(z)}. \tag{A.16}$$

Hence, adding and subtracting Equations (A.15) and (A.16), while replacing in the latter i by $-i$, the following stress representations are obtained [42, 43]:

$$\sigma_x + \sigma_y = 2(\varphi'(z) + \overline{\varphi'(z)}) = 4\,\mathrm{Re}(\varphi'(z)), \tag{A.17a}$$

$$\sigma_y - \sigma_x + 2i\tau_{yx} = 2(\overline{z}\varphi''(z) + \psi'(z)). \tag{A.17b}$$

Interestingly, the function $f(x, y)$ has a simple mechanical interpretation. Let $F = F_x + i\,F_y$ be the resultant force acting on an element AA' (see Figure A.1) ; making use of Equation (A.14), we can relate the net force F to the functions $\varphi(z)$ and $\psi(z)$:

$$F_x + i\,F_y = \int_A^{A'} ds\,(\sigma_{nx} + i\,\sigma_{ny}) = -i[\varphi(z) + z\overline{\varphi'(z)} + \overline{\psi(z)}]_A^{A'}, \tag{A.18}$$

where $[\ ]_A^{A'}$ denotes the increase undergone by the expression in the brackets as the point moves from A to A', with A being fixed at all times, and A' allowed to move. Indicating with $z = x + i\,y$ the coordinates of the point A', we get:

$$f(x, y) = i(F_x + i\,F_y) + C_1 = i\int_A^{A'} ds\,(\sigma_{nx} + i\,\sigma_{ny}) + C_1, \tag{A.19}$$

with C_1 being a real constant. Furthermore, the resultant moment about the origin of the coordinate system can be determined as:

$$M = \int_A^{A'} ds\,(x\sigma_{ny} - y\sigma_{nx}). \tag{A.20}$$

Hence, recalling Equation (A.13) and integrating by parts, it is shown that the resultant moment M is equal to:

$$M = -\left[x\frac{\partial U}{\partial x} + y\frac{\partial U}{\partial y}\right]_A^{A'} + [U]_A^{A'}. \tag{A.21}$$

Recognizing that the term in the square brackets $x\partial U/\partial x + y\partial U/\partial y = \mathrm{Re}(z(\partial U/\partial x - i\partial U/\partial y)) = \mathrm{Re}(\overline{f(z)})$, and making use of Equations (A.7) and (A.10), we finally obtain the following expression:

$$M = [\mathrm{Re}(\chi(z) - z\psi(z) + z\overline{z}\varphi'(z))]_A^{A'}. \tag{A.22}$$

Incidentally, for the time being, since we consider a simply connected region S, the functions $\varphi(z)$, $\psi(z)$ and $\chi(z)$ are single-valued in this region. Thus, if the curve under investigation is a contour, i.e. if A coincides with A', the resultant force and moment will be null.

Now, the question is how far the functions $\varphi(z)$ and $\psi(z)$ define the state or stress or the displacements of the points of the body. Let us start analyzing the case in which the state of stress is given, namely let σ_x, σ_y, τ_{yx} the components of the stress for a given state of elastic equilibrium of the body. Then, let us assume that the functions $\varphi_1(z)$ and $\psi_1(z)$ are related to the stress components, so as the functions $\varphi(z)$ and $\psi(z)$ (see Equations (A.17a) and (A.17b)). Specifically, from Equation (A.17a) it is clear that the real part of the functions $\varphi(z)$ and $\varphi_1(z)$ is identical, and nothing can be said about the imaginary part, so that we can write $\varphi_1(z) = \varphi(z) + iAz + \gamma$, with A being a real constant, and $\gamma = \alpha + i\beta$ an arbitrary complex constant. Moreover, from Equation (A.17b) we find that $\psi_1(z) = \psi(z) + \gamma_1$, where $\gamma_1 = \alpha_1 + i\beta_1$ is an arbitrary complex constant. Therefore, the state of stress is not altered if the following substitutions are made:

$$\varphi(z) \quad \rightarrow \quad \varphi(z) + iAz + \gamma, \tag{A.23a}$$

$$\psi(z) \quad \rightarrow \quad \psi(z) + \gamma_1. \tag{A.23b}$$

Let us then investigate the arbitrariness of these functions if the components of the displacement, namely u and v, are given. In particular, they completely determine the state of stress, hence one may not make substitutions different from those in (A.23). In fact, making use of Equation (A.11), we have:

$$2\mu(u_1 + iv_1) = 2\mu(u + iv) + i\,(\kappa + 1)Az + \kappa\gamma - \gamma_1. \tag{A.24}$$

Thus, exploiting γ and γ_1, we recognize that:

$$2\mu(u_1 + iv_1) = 2\mu(u + iv) + i\,(\kappa + 1)Az + \kappa(\alpha + i\beta) - \alpha_1 - i\beta_1, \tag{A.25}$$

so that, considering the real and imaginary parts respectively, we obtain the expression for the components u_1 and v_1, i.e.

$$u_1 = u + u_m, \qquad v_1 = v + v_m, \tag{A.26}$$

where u_m and v_m are rigid-body displacements and are equal to $u_m = (-(\kappa + 1)Ay + \kappa\alpha - \alpha_1)/2\mu$ and $v_m = ((\kappa + 1)Ax + \kappa\beta + \beta_1)/2\mu$. This has to be expected, since the displacements, corresponding to a given state of stress, are uniquely determined apart from a rigid-body motion. Hence, the substitutions in (A.23) affect the displacements, unless $A = 0$, $\kappa\gamma - \gamma_1 = 0$.

In addition, it is important to investigate how these functions, relating to a given state of stress, change under transformation from one set of orthogonal coordinates to another. First, let us consider the effect of the translation of the origin to a new point

(x_0, y_0). Denote the coordinates of a point in the old system with $z = x + i\,y$, while those of the same point in the new frame as $z = x_1 + i\,y_1$, where $z = z_0 + z_1$. Indicating with $\varphi^*(z)$ and $\psi^*(z)$ the corresponding functions in the new reference frame, Equation (A.17a) shows that, since the stress components are not affected by a translation, the following relationship holds:

$$\varphi(z) = \varphi^*(z_1) = \varphi^*(z - z_0). \tag{A.27}$$

On the other hand, making use of Equation (A.17b), we can write:

$$\overline{z}\varphi''(z)+\psi'(z) = \overline{z_1}\varphi^{*''}(z_1)+\psi^{*\prime}(z_1) = \overline{z}\varphi^{*''}(z-z_0)+\psi^{*\prime}(z-z_0)-\overline{z_0}\varphi^{*''}(z-z_0), \tag{A.28}$$

whence, by Equation (A.27), we obtain

$$\psi(z) = \psi^*(z - z_0) - \overline{z_0}\varphi^{*\prime}(z - z_0). \tag{A.29}$$

Therefore, Equations (A.27) and (A.29) highlight that the function $\varphi(z)$ is invariant under the translation of the origin; conversely, the same cannot be said for the function $\psi(z)$.

Now, let us consider how a rotation of the axes of the reference frame, while keeping the origin fixed, affects the functions under analysis. In particular, we have $z = z_1 e^{i\alpha}$, with α being the angle between the axes x and x_1. As before, Equation (A.17a) shows that:

$$\mathrm{Re}(\varphi'(z)) = \mathrm{Re}(\varphi^{*\prime}(z_1)) = \mathrm{Re}(\varphi^{*\prime}(ze^{-i\alpha})), \tag{A.30}$$

so that, by reckoning that the functions $\varphi'(z)$ and $\varphi^{*\prime}(z)$ may differ by an imaginary constant $i\,A$, the integration of Equation (A.30) leads to $\varphi(z) = e^{i\alpha}\varphi^*(ze^{-i\alpha}) + i\,Az + a + i\,b$, with a and b being arbitrary real constants. As shown beforehand, the constants A, a, and b do not affect the stress distribution. Thus, they can be omitted, and we have:

$$\varphi(z) = e^{i\alpha}\varphi^*(ze^{-i\alpha}). \tag{A.31}$$

Hence, referring to Equation (A.17b), the property of invariance of the quadratic form $\Lambda(\xi, \eta) = \sigma_x\xi^2 + 2\tau_{yx}\xi\eta + \sigma_y\eta^2$ [43] heeds us to write the following identity

$$\overline{z_1}\varphi^{*''}(z_1) + \psi^{*\prime}(z_1) = (\overline{z}\varphi^{''}(z) + \psi'(z))e^{2i\alpha}, \tag{A.32}$$

and, since $\varphi(z) = e^{i\alpha}\varphi^*(ze^{-i\alpha})$ (see Equation (A.31)), we obtain
$\psi(z) = e^{-i\alpha}\psi^*(ze^{-i\alpha}) + a_1 + i\,b_1$, with a_1, b_1 arbitrary real constants. The latter can be omitted since they do not affect the stress distribution, so that:

$$\psi(z) = e^{-i\alpha}\psi^*(ze^{-i\alpha}). \tag{A.33}$$

With the aim of investigating circular contact problems, it is of particular interest to particularize the relationships just derived for a polar reference frame, where $z = x + i\,y = re^{i\theta}$, with r being the radius vector and θ the angular position of the generic point. The complex representation of the displacement (see Equation (A.11)) can be rephrased as:

$$2\mu(u_r + i\,u_\theta) = e^{-i\theta}(\kappa\varphi(z) - z\overline{\varphi'(z)} - \overline{\psi(z)}), \tag{A.34}$$

with u_r and u_θ being the radial and tangential components of the displacement respectively. At the same time, we can specify the complex representation of the stress

components in a polar reference frame: with reference to Equations (A.17a) and (A.17b), together with the previous analysis, it is possible to write

$$\sigma_{rr} + \sigma_{\theta\theta} = 2(\varphi'(z) + \overline{\varphi'(z)}) = 4\,\mathrm{Re}(\varphi'(z)), \tag{A.35a}$$

$$\sigma_{\theta\theta} - \sigma_{rr} + 2i\tau_{r\theta} = 2(\overline{z}\varphi''(z) + \psi'(z))e^{2i\theta}. \tag{A.35b}$$

A more convenient form of Equations (A.34) and (A.35) has been employed by Stevenson [42] and Rothman [128, 129]. Specifically, recalling the identities $\varphi(z) = \Omega(z)/4$ and $\chi(z) = \omega(z)/4$ for the displacement components we have:

$$8\mu(u_r + i\,u_\theta) = e^{-i\theta}(\kappa\Omega(z) - z\overline{\Omega'(z)} - \overline{\omega'(z)}), \tag{A.36}$$

while, for the stress components we find

$$\sigma_{rr} + \sigma_{\theta\theta} = \frac{1}{2}(\Omega'(z) + \overline{\Omega'(z)}), \tag{A.37a}$$

$$\sigma_{rr} - \sigma_{\theta\theta} + 2i\tau_{r\theta} = -\frac{1}{2}\left(\overline{z}\Omega''(z) + \frac{\overline{z}}{z}\overline{\omega''(z)}\right). \tag{A.37b}$$

Now, we are ready to determine the Green's spatial functions for the circular contact problems analyzed throughout this thesis. Although the main interest of this work relates to purely radial terms, here the expressions for both radial and tangential displacements, when the system is subject to radial and tangential load, will be furnished.

A.2 Cylindrical hole in an infinite space under isolated forces on the boundary

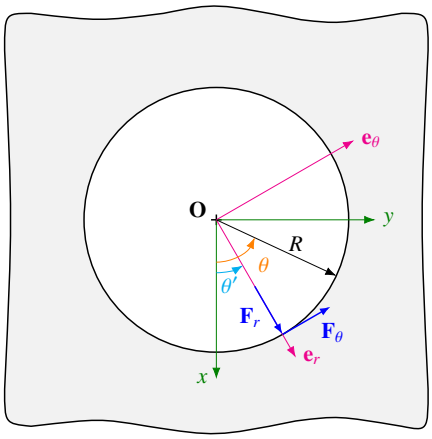

Figure A.2: Schematic of a cylindrical hole on an infinite space under isolated tangential and radial forces applied to the boundary.

As reported in Figure A.2, the first step deals with the assessment of the elastic problem for a cylindrical hole loaded with a normal and a tangential force, being respectively F_r and F_θ. In this case, moving from what has been proposed by Rothman in Ref. [128], we can make use of Equation (A.36).

$\Omega(z)$ and $\omega(z)$ are the two complex potentials, which are functions of a single complex variable $z = R\exp(i\theta)$ and are equal to:

$$\begin{cases} \Omega(z) = -\dfrac{2F}{\pi}\log(z-a_1) + \dfrac{2F\kappa}{\pi(\kappa+1)}\log z \\ \omega(z) = \dfrac{2\bar{F}}{\pi}z\log(z-a_1) + \dfrac{2}{\pi}(F\bar{a}_1 - \bar{F}a_1)\log(z-a_1) - \dfrac{2\bar{F}z\log z}{\pi(\kappa+1)} - \dfrac{2}{\pi}F\bar{a}_1\log z + \dfrac{2F\kappa R^2}{\pi(\kappa+1)z} \end{cases} \tag{A.38}$$

with F_r and F_θ are the radial and tangential contributions to the total force F applied at the point $a_1 = R\exp(i\theta')$, being $z\bar{z} = R^2 = a_1\bar{a}_1$. Furthermore, μ is the second Lamé's constant, $\mu = E/2(1+\nu)$.

Now, for $\theta' = 0$, developing the aforementioned relations based on the complex potentials, the radial and tangential displacements due to the radial force component F_r, respectively defined as u_{rr} and $u_{r\theta}$, are:

$$u_{rr}(s,F_r) = \frac{F_r}{4\mu\pi}\left[-\frac{\kappa}{\kappa+1}(2\log R+1)\cos\theta - \frac{\kappa+1}{2}\mathrm{B}(\theta)\cos\theta + (\kappa-1)\mathrm{A}(\theta)\sin\theta\right] \tag{A.39}$$

$$u_{r\theta}(s,F_r) = \frac{F_r}{4\mu\pi}\left[\frac{\kappa}{\kappa+1}(2\log R+1)\sin\theta + \frac{\kappa+1}{2}\mathrm{B}(\theta)\sin\theta + (\kappa-1)\mathrm{A}(\theta)\cos\theta\right] \tag{A.40}$$

where $\theta = s/R$ is the angle subtended by the arc s. Furthermore, the terms $\mathrm{A}(\theta)$ and $\mathrm{B}(\theta)$ are equal to $\mathrm{A}(\theta) = \arg(1/2 - i/2\cot(\theta/2))$ and $\mathrm{B}(\theta) = \log(2-2\cos\theta) = 2\log(2|\sin(\theta/2)|)$.

Incidentally, if we define the total displacement as $\mathbf{u} = u_{rr}\mathbf{e}_r + u_{r\theta}\mathbf{e}_\theta$, we observe that we have a mean term being equal to $\bar{u} = -\kappa F_r(2\log R+1)/4\mu\pi\,(\kappa+1)$ and an additional one that varies with the angle $\tilde{u} = ((\kappa-1)\mathrm{A}(\theta) - (\kappa+1)\,\mathrm{B}(\theta)/2)\,F_r/4\mu\pi$. Please notice that, for a Poisson's ratio $\nu = 0.5$, the additional term $\tilde{u}$ is identical to the elastic Green's function obtained by Carbone and Mangialardi in Ref. [73, 74].

Furthermore, for a tangential force F_θ, the radial and tangential displacements, defined as $u_{\theta r}$ and $u_{\theta\theta}$ are:

$$u_{\theta r}(s,F_\theta) = \frac{F_\theta}{4\mu\pi}\left[-\frac{\kappa}{\kappa+1}(2\log R+1)\sin\theta - \frac{\kappa+1}{2}\mathrm{B}(\theta)\sin\theta - (\kappa-1)\mathrm{A}(\theta)\cos\theta\right] \tag{A.41}$$

$$u_{\theta\theta}(s,F_\theta) = \frac{F_\theta}{4\mu\pi}\left[-\frac{\kappa}{\kappa+1}(2\log R+1)\cos\theta - \frac{\kappa+1}{2}\mathrm{B}(\theta)\cos\theta + (\kappa-1)\mathrm{A}(\theta)\sin\theta\right] \tag{A.42}$$

Now, we can employ the aforementioned solutions to define the following tensor $\mathbf{L}$, necessary to the numerical solution of the contact problem:

$$\mathbf{L}(s) = \int_0^{2\pi R} ds'\,\mathbf{G}(s-s')\boldsymbol{\chi}(s'), \tag{A.43}$$

where the distributed load $\boldsymbol{\chi}$ is $\boldsymbol{\chi} = \chi_r\mathbf{e}_r + \chi_\theta\mathbf{e}_\theta$, with χ_r and χ_θ being unitary in an arc of length $2\alpha R$ and vanishing outside, and $\mathbf{G}$ is the Green's tensor associated to a concentrated unit force and equal to:

$$\mathbf{G}(s) = 2\mu(1+\nu)\begin{bmatrix} u_{rr}(s,1) & u_{r\theta}(s,1) \\ u_{\theta r}(s,1) & u_{\theta\theta}(s,1) \end{bmatrix} \tag{A.44}$$

with $u_{rr}, u_{r\theta}, u_{\theta r}, u_{\theta\theta}$ previously given in this Section. Notice that we have multiplied by a factor $2\mu(1+\nu)$, i.e., the Young's modulus, to correctly introduce the spatial Green's

tensor in Equation (2.27). Equation (A.43) can be solved analytically by extracting the Cauchy principal value as:

$$L_{rr}(s) = \frac{1+\nu}{2\pi}\left[-\frac{\kappa}{\kappa+1}(2\log R+1)\mathrm{C}_1(\theta) + (\kappa-1)\,\mathrm{A}_1(\theta) - \frac{\kappa+1}{2}\mathrm{B}_1(\theta)\right] \tag{A.45}$$

$$L_{r\theta}(s) = \frac{1+\nu}{2\pi}\left[\frac{\kappa}{\kappa+1}(2\log R+1)\mathrm{S}_1(\theta) + (\kappa-1)\mathrm{A}_2(\theta) + \frac{\kappa+1}{2}\mathrm{B}_2(\theta)\right] \tag{A.46}$$

$$L_{\theta r}(s) = -\frac{1+\nu}{2\pi}\left[\frac{\kappa}{\kappa+1}(2\log R+1)\mathrm{S}_1(\theta) + (\kappa-1)\mathrm{A}_2(\theta) + \frac{\kappa+1}{2}\mathrm{B}_2(\theta)\right] \tag{A.47}$$

$$L_{\theta\theta}(s) = \frac{1+\nu}{2\pi}\left[-\frac{\kappa}{\kappa+1}(2\log R+1)\mathrm{C}_1(\theta) + (\kappa-1)\mathrm{A}_1(\theta) - \frac{\kappa+1}{2}\mathrm{B}_1(\theta)\right] \tag{A.48}$$

where,

$$\begin{aligned}\mathrm{A}_1(\theta) =& \cos(\theta-\alpha)\left[\frac{\theta-\alpha}{2} + \frac{\pi}{2}\Big(1-2\mathcal{H}(\theta-\alpha)\Big)\right] - \frac{1}{2}(\sin(\theta-\alpha)-\sin(\theta+\alpha)) + \\ &- \cos(\theta+\alpha)\left[\frac{\theta+\alpha}{2} + \frac{\pi}{2}\Big(1-2\mathcal{H}(\theta+\alpha)\Big)\right] - \pi(\mathcal{H}(\theta+\alpha)-\mathcal{H}(\theta-\alpha))\end{aligned} \tag{A.49}$$

$$\begin{aligned}\mathrm{A}_2(\theta) =& \sin(\theta+\alpha)\left[\frac{\theta+\alpha}{2} + \frac{\pi}{2}\Big(1-2\mathcal{H}(\theta+\alpha)\Big)\right] - \frac{1}{2}(\cos(\theta-\alpha)-\cos(\theta+\alpha)) + \\ &- \sin(\theta-\alpha)\left[\frac{\theta-\alpha}{2} + \frac{\pi}{2}\Big(1-2\mathcal{H}(\theta-\alpha)\Big)\right]\end{aligned} \tag{A.50}$$

$$\mathrm{B}_1(\theta) = -2\alpha - \sin(\theta+\alpha)(1-\log(2-2\cos(\theta+\alpha))) + \sin(\theta-\alpha)(1-\log(2-2\cos(\theta-\alpha))) \tag{A.51}$$

$$\begin{aligned}\mathrm{B}_2(\theta) =& \cos(\theta+\alpha)(1-\log(2-2\cos(\theta+\alpha))) + \log(1-\cos(\theta+\alpha)) + \\ &- \cos(\theta-\alpha)(1-\log(2-2\cos(\theta-\alpha))) - \log(1-\cos(\theta-\alpha))\end{aligned} \tag{A.52}$$

$$\mathrm{C}_1(\theta) = \sin(\theta+\alpha) - \sin(\theta-\alpha) \tag{A.53}$$

$$\mathrm{S}_1(\theta) = \cos(\theta-\alpha) - \cos(\theta+\alpha). \tag{A.54}$$

A.3 Isolated forces on the boundary of a cylinder with central fixing

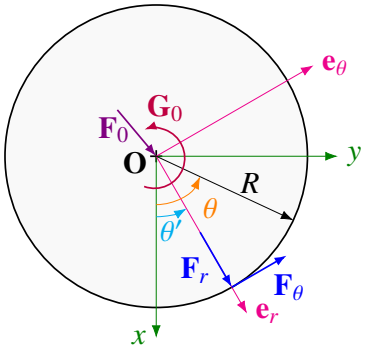

Figure A.3: Schematic of an infinite cylinder, fixed at the center, and subject to isolated tangential and radial forces applied to the boundary.

Hence, we focus on the elastic problem for an infinite cylinder loaded with normal and tangential forces, respectively F_r and F_θ. In this scenario, sketched in Figure A.3, we can employ the complex representation for the displacement of Equation (A.36), where the complex potentials $\Omega(z)$ and $\omega(z)$ in the complex variable $z = R\exp(i\theta)$ are given by [129]:

$$\begin{cases} \Omega(z) = -\dfrac{2}{\pi}F\log z_r - \dfrac{2F_0\log z}{\pi(\kappa+1)} - \dfrac{1}{2\pi a_1^2}(\bar{F}a_1 + F\bar{a}_1)z + \dfrac{2\bar{F}_0 z^2}{\pi a_1^2(\kappa+1)} \\ \omega(z) = \dfrac{2z}{\pi}\bar{F}\log z_r + \dfrac{2}{\pi}(F\bar{a}_1 - \bar{F}a_1)\log z_r + \dfrac{2\kappa\bar{F}_0 z\log z}{\pi(\kappa+1)} + \dfrac{2iG_0}{\pi}\log z \end{cases} \tag{A.55}$$

where F_r and F_θ are the radial and tangential contributions to the total force F applied at the point $a_1 = R\exp(i\theta')$, being $z\bar{z} = R^2 = a_1\bar{a}_1$.

Following the same reasoning of the previous Section, for $\theta' = 0$, developing the aforementioned relations based on the complex potentials, the radial and tangential displacements due to the radial force component F_r, respectively defined as u_{rr} and $u_{r\theta}$, are:

$$u_{rr}(s,F_r) = \frac{F_r}{4\mu\pi}\left[\frac{1-(\kappa^2+1)\log R}{\kappa+1}\cos\theta - \cos\theta - \frac{\kappa+1}{2} + (\kappa-1)\mathrm{A}'(\theta)\sin\theta - \frac{\kappa+1}{2}\mathrm{B}(\theta)\cos\theta\right] \tag{A.56}$$

$$u_{r\theta}(s,F_r) = \frac{F_r}{4\mu\pi}\left[-\frac{1-(\kappa^2+1)\log R}{\kappa+1}\sin\theta + (\kappa-1)\mathrm{A}'(\theta)\cos\theta + \frac{\kappa+1}{2}\mathrm{B}(\theta)\sin\theta - \sin\theta\right] \tag{A.57}$$

where $\theta = s/R$ is the angle subtended by the arc s. Furthermore $\mathrm{A}'(\theta) = \arg(-1/2 - i/2\,\cot(\theta/2))$ and $\mathrm{B}(\theta) = \log(2-2\cos\theta) = 2\log(2|\sin(\theta/2)|)$.

Incidentally, if we express the total displacement $\mathbf{u}$ as $\mathbf{u} = u_{rr}\mathbf{e}_r + u_{r\theta}\mathbf{e}_\theta$, we reckon a mean term being equal to $\bar{u} = (1-(\kappa^2+1)\log R)/4\mu\pi\,(\kappa+1)$, and an additional one varying with the angle
$\tilde{u} = ((\kappa-1)\mathrm{A}'(\theta)\sin\theta - ((\kappa+1)/2)\mathrm{B}(\theta)\cos\theta - \cos\theta - ((\kappa+1)/2))\,F_r/4\mu\pi$.

Furthermore, for a tangential force F_θ, the radial and tangential displacements, defined as $u_{\theta r}$ and $u_{\theta\theta}$ are:

$$u_{\theta r}(s,F_\theta)=\frac{F_\theta}{4\mu\pi}\left[\frac{1-(\kappa^2+1)\log R}{\kappa+1}\sin\theta-(\kappa-1)\mathrm{A}'(\theta)\cos\theta-\frac{\kappa+1}{2}\mathrm{B}(\theta)\sin\theta-\sin\theta\right] \tag{A.58}$$

$$u_{\theta\theta}(s,F_\theta)=\frac{F_\theta}{4\mu\pi}\left[\frac{1-(\kappa^2+1)\log R}{\kappa+1}\cos\theta+(\kappa-1)\mathrm{A}'(\theta)\sin\theta-\frac{\kappa+1}{2}\mathrm{B}(\theta)\cos\theta+\cos\theta\right] \tag{A.59}$$

Then, the Cauchy principal values are given by:

$$L_{rr}(s)=\frac{1+\nu}{2\pi}\left[\frac{1-(\kappa^2+1)\log R}{\kappa+1}\mathrm{C}_1(\theta)+(\kappa-1)\mathrm{A}_3(\theta)-\frac{\kappa+1}{2}\mathrm{B}_1(\theta)-\mathrm{C}_1(\theta)-(\kappa+1)\alpha\right] \tag{A.60}$$

$$L_{r\theta}(s)=\frac{1+\nu}{2\pi}\left[-\frac{1-(\kappa^2+1)\log R}{\kappa+1}\mathrm{S}_1(\theta)+(\kappa-1)\mathrm{A}_4(\theta)+\frac{\kappa+1}{2}\mathrm{B}_2(\theta)-\mathrm{S}_1(\theta)\right] \tag{A.61}$$

$$L_{\theta r}(s)=\frac{1+\nu}{2\pi}\left[\frac{1-(\kappa^2+1)\log R}{\kappa+1}\mathrm{S}_1(\theta)-(\kappa-1)\mathrm{A}_4(\theta)-\frac{\kappa+1}{2}\mathrm{B}_2(\theta)-\mathrm{S}_1(\theta)\right] \tag{A.62}$$

$$L_{\theta\theta}(s)=\frac{1+\nu}{2\pi}\left[\frac{1-(\kappa^2+1)\log R}{\kappa+1}\mathrm{C}_1(\theta)+(\kappa-1)\mathrm{A}_3(\theta)-\frac{\kappa+1}{2}\mathrm{B}_1(\theta)+\mathrm{C}_1(\theta)\right] \tag{A.63}$$

where,

$$\begin{aligned}\mathrm{A}_3(\theta)=&\cos(\theta+\alpha)\left[\frac{\theta+\alpha}{2}-\frac{\pi}{2}\Big(1-2\mathcal{H}(\theta+\alpha)\Big)\right]-\frac{1}{2}(\sin(\theta+\alpha)-\sin(\theta-\alpha))+\\&-\cos(\theta-\alpha)\left[\frac{\theta-\alpha}{2}-\frac{\pi}{2}\Big(1-2\mathcal{H}(\theta-\alpha)\Big)\right]-\pi(\mathcal{H}(\theta+\alpha)-\mathcal{H}(\theta-\alpha))\end{aligned} \tag{A.64}$$

$$\begin{aligned}\mathrm{A}_4(\theta)=&\sin(\theta-\alpha)\left[\frac{\theta-\alpha}{2}-\frac{\pi}{2}\Big(1-2\mathcal{H}(\theta-\alpha)\Big)\right]+\frac{1}{2}(\cos(\theta-\alpha)-\cos(\theta+\alpha))+\\&-\sin(\theta+\alpha)\left[\frac{\theta+\alpha}{2}-\frac{\pi}{2}\Big(1-2\mathcal{H}(\theta+\alpha)\Big)\right]\end{aligned} \tag{A.65}$$

while the other functions have been introduced in the previous Section.

Figure A.4 represents, in the polar reference system, the function $\mathcal{L}_{rr}(S)$, defined in Equation (2.16), for a linearly viscoelastic material with a single relaxation time at increasing values of the dimensionless speed $\tilde{\omega}=\omega\tau$. The deformed contour, properly magnified to better appreciate the asymmetric nature of the displacement field when viscoelasticity arises, is superposed to the undeformed contour (dashed lines). Indeed, at very low-speed and very high-speed values, where the material enters respectively the rubbery and the glassy elastic regions, we observe a symmetrical deformation field; conversely, a non-symmetric trend in the pressure and displacement distributions is evident for intermediate velocities as proper viscoelasticity effects occur. Indeed, since the material is still relaxing upon the load passage, larger deformations are observed at the trailing edge.

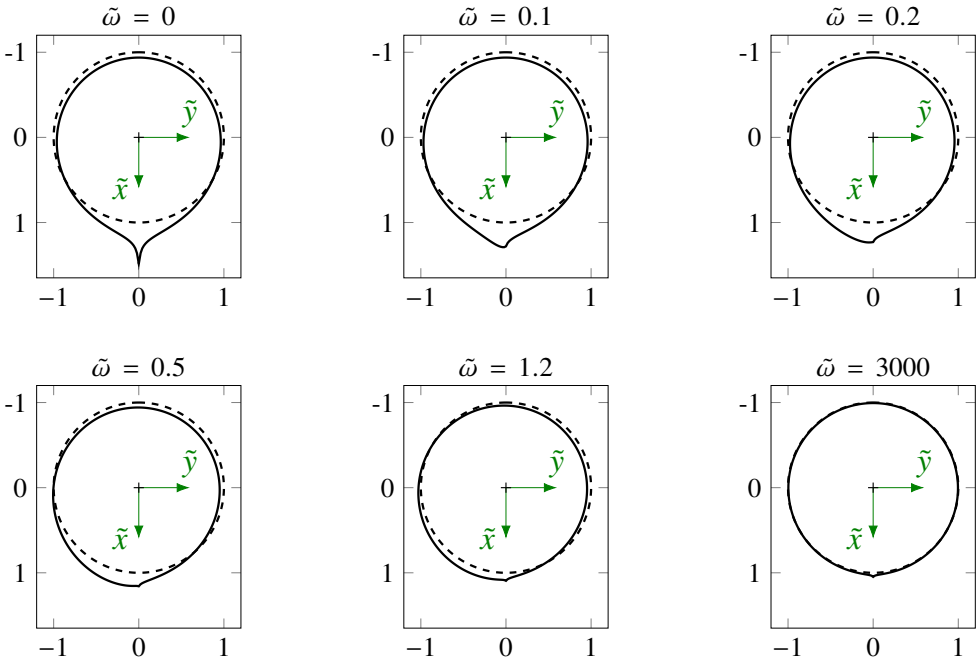

Figure A.4: Deformed surfaces as a result of the application of a radial unit force for different values of the dimensionless speed $\tilde{\omega} = \omega\tau$. The numerical results are carried out for a viscoelastic material, characterized by a single relaxation time $\tau = 0.01$ s, glassy and soft moduli respectively equal to $E_\infty = 10^7$ Pa and $E_0 = 10^6$ Pa, and Poisson's ratio $\nu = 0.5$.

A.4 Cylinder under diametrically opposite forces on the boundary

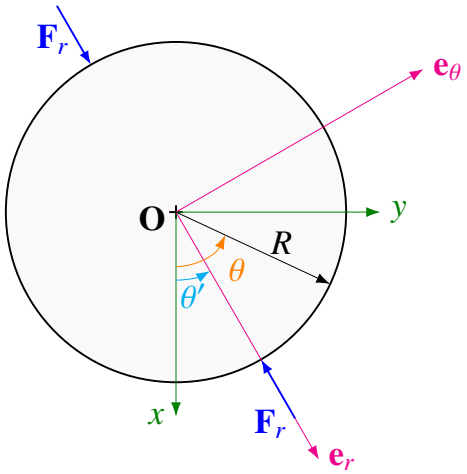

Figure A.5: Schematic of a cylinder under diametrically opposite forces on the boundary.

Now, let us consider two isolated, diametrically opposite, equal forces, $|\mathbf{F}_1| = |\mathbf{F}_2| = |\mathbf{F}_r|$, are applied at the boundary of a cylinder. This case study has been extensively tackled in literature [43, 52, 130–133] and might be of particular interest in analyzing the

contact problem in a rolling element bearing, where the rolling elements are deformable, and the raceways are rigid. Specifically, we extend the reasoning done in the previous Section, with F_0 and G_0 being null:

$$\begin{cases} \Omega(z) = -\dfrac{2}{\pi}\displaystyle\sum_{k=1}^{2} F_k \log z_k - \dfrac{z}{2\pi a^2}\sum_{k=1}^{2} \bar{F}_k a_k + F_k \bar{a}_k \\ \omega(z) = \dfrac{2z}{\pi}\displaystyle\sum_{k=1}^{2} \bar{F}_k \log z_k + \dfrac{2}{\pi}\sum_{k=1}^{2} (F_k \bar{a}_k - \bar{F}_k a_k) \log z_k \end{cases} \tag{A.66}$$

where $z = R\exp(i\theta)$, $z_k = z - a_k$ and $z\bar{z} = R^2 = a_k\bar{a}_k$, $k = 1, 2$, with $a_k = R\exp(i\theta'_k)$, being $\theta_1 = \theta'$ and $\theta_2 = \pi + \theta'$. For the sake of simplicity let us assume $\theta' = 0$. Recalling the equilibrium condition $\sum_k \mathbf{F}_k = \mathbf{0}$ and making use of Equation (A.36), we get the following radial and tangential displacements:

$$u_{rr}(s, F_r) = \frac{F_r}{4\mu\pi}\left[\kappa + 1 + (\kappa - 1)A''(\theta)\sin\theta + \frac{\kappa+1}{2}(\mathrm{B}(\theta) - \mathrm{B}'(\theta))\cos\theta\right] \tag{A.67}$$

$$u_{r\theta}(s, F_r) = \frac{F_r}{4\mu\pi}\left[- (\kappa - 1)A''(\theta)\cos\theta - \frac{\kappa+1}{2}(\mathrm{B}(\theta) - \mathrm{B}'(\theta))\sin\theta\right] \tag{A.68}$$

where $\mathrm{A}''(\theta) = \theta/2 - \mathrm{A}(\theta)$, $\mathrm{B}'(\theta) = \log(2 + 2\cos(\theta))$. Moreover, as presented in Section A.2, the terms $\mathrm{A}(\theta)$ and $\mathrm{B}(\theta)$ are equal to $\mathrm{A}(\theta) = \arg(1/2 - i/2\cot(\theta/2))$ and $\mathrm{B}(\theta) = \log(2 - 2\cos\theta) = 2\log(2|\sin(\theta/2)|)$.

Incidentally, we can define the spatial functions $L_{rr}(s)$ and $L_{r\theta}(s)$ as:

$$L_{rr}(s) = \frac{1+\nu}{2\pi}\left[(\kappa+1)2\alpha + (\kappa-1)\mathrm{A}_5(\theta) + \frac{\kappa+1}{2}\mathrm{B}_3(\theta)\right] \tag{A.69}$$

$$L_{r\theta}(s) = \frac{1+\nu}{2\pi}\left[(\kappa-1)\mathrm{A}_6(\theta) - \frac{\kappa+1}{2}\mathrm{B}_4(\theta)\right] \tag{A.70}$$

where:

$$\begin{aligned} \mathrm{B}_3(\theta) = &- 4\alpha + \sin(\theta+\alpha)[\log(2 - 2\cos(\theta+\alpha)) - \log(2 + 2\cos(\theta+\alpha))] + \\ &+ \sin(\theta-\alpha)[\log(2 + 2\cos(\theta-\alpha)) - \log(2 - 2\cos(\theta-\alpha))] \end{aligned} \tag{A.71}$$

$$\begin{aligned} \mathrm{A}_5(\theta) = &\pi\left[\frac{1}{2}\cos(\theta-\alpha)(1 - 2\mathcal{H}(\theta-\alpha)) + \mathcal{H}(\theta-\alpha) - \mathcal{H}(\theta+\alpha) + \right. \\ &\left. - \frac{1}{2}\cos(\theta+\alpha)(1 - 2\mathcal{H}(\theta+\alpha))\right] \end{aligned} \tag{A.72}$$

$$\begin{aligned} \mathrm{B}_4(\theta) = &\cos(\theta-\alpha)[\log(2 - 2\cos(\theta-\alpha)) - \log(2 + 2\cos(\theta-\alpha))] + \\ &+ \cos(\theta+\alpha)[\log(2 + 2\cos(\theta+\alpha)) - \log(2 - 2\cos(\theta+\alpha))] + \\ &+ \log(1 - \cos(\theta+\alpha)) + \log(1 + \cos(\theta+\alpha)) + \\ &- \log(1 - \cos(\theta-\alpha)) - \log(1 + \cos(\theta-\alpha)) \end{aligned} \tag{A.73}$$

$$\mathrm{A}_6(\theta) = \frac{\pi}{2}[\sin(\theta+\alpha)(1 - 2\mathcal{H}(\theta+\alpha)) - \sin(\theta-\alpha)(1 - 2\mathcal{H}(\theta-\alpha))] \tag{A.74}$$

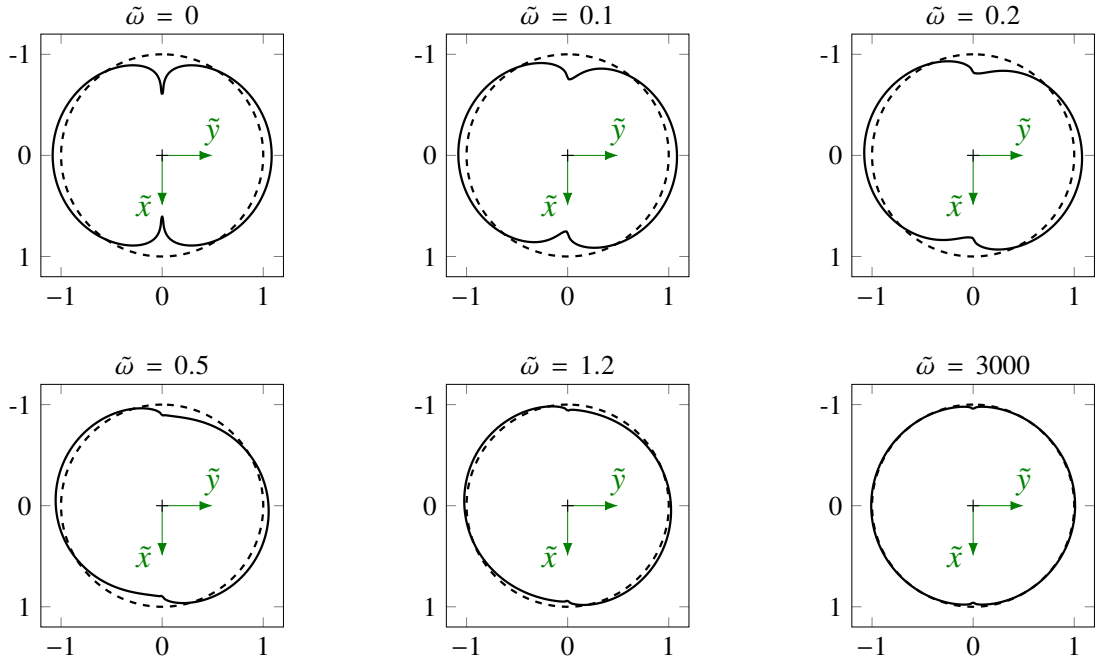

Figure A.6: Deformed surfaces as a result of the application of a radial unit force for different values of the dimensionless speed $\tilde{\omega} = \omega\tau$. The numerical results are carried out for a viscoelastic material, characterized by a single relaxation time $\tau = 0.01$ s, glassy and soft moduli respectively equal to $E_\infty = 10^7$ Pa and $E_0 = 10^6$ Pa, and Poisson's ratio $\nu = 0.5$.

Ultimately, Figure A.6 represents, in the polar reference system, $\mathcal{L}_{rr}(\Theta)$ for a single relaxation time material at increasing values of the dimensionless speed $\tilde{\omega} = \omega\tau$. The deformation is magnified to better appreciate the viscoelastic effects. Indeed, at intermediate speeds we retrieve strong asymmetric pressure and displacement distributions, due to the different relaxation processes occurring at the leading and trailing edge of the contact. On the contrary, at very low speeds and very high speeds, the material behaves like a solid elastic body, and symmetric pressure and displacement fields are obtained.

References

[1] G. Bao, S. Suresh, Cell and molecular mechanics of biological materials, Nature Materials 2 (11) (2003) 715–725. doi:https://doi.org/10.1038/nmat1001.

[2] A. J. Licup, S. Münster, A. Sharma, M. Sheinman, L. M. Jawerth, B. Fabry, D. A. Weitz, F. C. MacKintosh, Stress controls the mechanics of collagen networks, Proceedings of the National Academy of Sciences 112 (31) (2015) 9573–9578. doi:https://doi.org/10.1073/pnas.1504258112.

[3] T. André, V. Lévesque, V. Hayward, P. Lefèvre, J.-L. Thonnard, Effect of skin hydration on the dynamics of fingertip gripping contact, Journal of The Royal Society Interface 8 (64) (2011) 1574–1583. doi:10.1098/rsif.2011.0086.

[4] M. L. Crichton, B. C. Donose, X. Chen, A. P. Raphael, H. Huang, M. A. Kendall, The viscoelastic, hyperelastic and scale dependent behaviour of freshly excised individual skin layers, Biomaterials 32 (20) (2011) 4670–4681. doi:https://doi.org/10.1016/j.biomaterials.2011.03.012.

[5] G. Han, C. Hess, M. Eriten, C. R. Henak, Uncoupled poroelastic and intrinsic viscoelastic dissipation in cartilage, Journal of the Mechanical Behavior of Biomedical Materials 84 (2018) 28–34. doi:https://doi.org/10.1016/j.jmbbm.2018.04.024.

[6] Z. Murčinková, J. Živčák, J. Zajac, P. Adamčík, Passive multi-layer composite damper of flat belt tensioner idler, Applied Sciences 11 (7) (2021). doi:10.3390/app11073267.

[7] B. S. Ünlü, E. Atik, S. Köksal, Tribological properties of polymer-based journal bearings, Materials & Design 30 (7) (2009) 2618–2622. doi:https://doi.org/10.1016/j.matdes.2008.11.018.

[8] S. C. Hunter, The Rolling Contact of a Rigid Cylinder With a Viscoelastic Half Space, Journal of Applied Mechanics 28 (4) (1961) 611–617. doi:10.1115/1.3641792.

[9] K. A. Grosch, The relation between the friction and visco-elastic properties of rubber, Proceedings of the Royal Society of London. Series A. Mathematical and Physical Sciences 274 (1356) (1963) 21–39. doi:https://doi.org/10.1098/rspa.1963.0112.

[10] B. N. J. Persson, Theory of rubber friction and contact mechanics, The Journal of Chemical Physics 115 (8) (2001) 3840–3861. doi:10.1063/1.1388626.

[11] P. L. Tallec, C. Rahler, Numerical models of steady rolling for non-linear viscoelastic structures in finite deformations, International Journal for Numerical Methods in Engineering 37 (7) (1994) 1159–1186. doi:https://doi.org/10.1002/nme.1620370705.

[12] J. Padovan, Finite element analysis of steady and transiently moving/rolling nonlinear viscoelastic structure—i. theory, Computers & Structures 27 (2) (1987) 249–257. doi:https://doi.org/10.1016/0045-7949(87)90093-9.

[13] J. Padovan, A. Kazempour, F. Tabaddor, B. Brockman, Alternative formulations of rolling contact problems, Finite Elements in Analysis and Design 11 (4) (1992) 275–284. doi:https://doi.org/10.1016/0168-874X(92)90010-A.

[14] B. N. J. Persson, Rolling friction for hard cylinder and sphere on viscoelastic solid, The European Physical Journal E 33 (4) (2010) 327–333. doi:https://doi.org/10.1140/epje/i2010-10678-y.

[15] S. Kusche, Frictional force between a rotationally symmetric indenter and a viscoelastic half-space, ZAMM - Journal of Applied Mathematics and Mechanics / Zeitschrift für Angewandte Mathematik und Mechanik 97 (2) (2016) 226–239. doi:https://doi.org/10.1002/zamm.201500169.

[16] X. Zhang, Q. J. Wang, T. He, Transient and steady-state viscoelastic contact responses of layer-substrate systems with interfacial imperfections, Journal of the Mechanics and Physics of Solids 145 (2020) 104170. doi:https://doi.org/10.1016/j.jmps.2020.104170.

[17] J. J. Kalker, Viscoelastic multilayered cylinders rolling with dry friction, Journal of Applied Mechanics 58 (3) (1991) 666–679. doi:https://doi.org/10.1115/1.2897247.

[18] I. Goryacheva, A. Goryachev, F. Sadegi, Contact of elastic bodies with thin viscoelastic coatings under conditions of rolling or sliding friction, Journal of Applied Mathematics and Mechanics 59 (4) (1995) 607–614. doi:https://doi.org/10.1016/0021-8928(95)00071-2.

[19] K. E. Koumi, T. Chaise, D. Nelias, Rolling contact of a rigid sphere/sliding of a spherical indenter upon a viscoelastic half-space containing an ellipsoidal inhomogeneity, Journal of the Mechanics and Physics of Solids 80 (2015) 1–25. doi:https://doi.org/10.1016/j.jmps.2015.04.001.

[20] I. Goryacheva, A. Miftakhova, Modelling of the viscoelastic layer effect in rolling contact, Wear 430-431 (2019) 256–262. doi:https://doi.org/10.1016/j.wear.2019.05.021.

[21] Q. J. Wang, L. Sun, X. Zhang, S. Liu, D. Zhu, Fft-based methods for computational contact mechanics, Frontiers in Mechanical Engineering 6 (2020). doi:10.3389/fmech.2020.00061.

[22] G. Carbone, C. Putignano, A novel methodology to predict sliding and rolling friction of viscoelastic materials: Theory and experiments, Journal of the Mechanics and Physics of Solids 61 (8) (2013) 1822–1834. doi:10.1016/j.jmps.2013.03.005.

[23] C. Putignano, G. Carbone, D. Dini, Theory of reciprocating contact for viscoelastic solids, Phys. Rev. E 93 (2016) 043003. doi:10.1103/PhysRevE.93.043003.

[24] N. Menga, C. Putignano, G. Carbone, G. P. Demelio, The sliding contact of a rigid wavy surface with a viscoelastic half-space, Proceedings of the Royal Society A: Mathematical, Physical and Engineering Sciences 470 (2169) (2014) 20140392. doi:https://doi.org/10.1098/rspa.2014.0392.

[25] C. Putignano, G. Carbone, Viscoelastic reciprocating contacts in presence of finite rough interfaces: A numerical investigation, Journal of the Mechanics and Physics of Solids 114 (2018) 185–193. doi:https://doi.org/10.1016/j.jmps.2018.02.005.

[26] C. Putignano, N. Menga, L. Afferrante, G. Carbone, Viscoelasticity induces anisotropy in contacts of rough solids, Journal of Mechanics Physics of Solids 129 (2019) 147–159. doi:10.1016/j.jmps.2019.03.024.

[27] N. Menga, G. Carbone, D. Dini, Exploring the effect of geometric coupling on friction and energy dissipation in rough contacts of elastic and viscoelastic coatings, Journal of the Mechanics and Physics of Solids 148 (2021) 104273. doi:10.1016/j.jmps.2020.104273.

[28] M. Scaraggi, B. Persson, Theory of viscoelastic lubrication, Tribology International 72 (2014) 118–130. doi:https://doi.org/10.1016/j.triboint.2013.12.011.

[29] C. Putignano, Soft lubrication: A generalized numerical methodology, Journal of the Mechanics and Physics of Solids 134 (2020) 103748. doi:https://doi.org/10.1016/j.jmps.2019.103748.

[30] M. Heß, F. Forsbach, An analytical model for almost conformal spherical contact problems: Application to total hip arthroplasty with uhmwpe liner, Applied Sciences 11 (23) (2021). doi:10.3390/app112311170.

[31] E. Askari, M. S. Andersen, A closed-form formulation for the conformal articulation of metal-on-polyethylene hip prostheses: Contact mechanics and sliding distance, Proceedings of the Institution of Mechanical Engineers, Part H: Journal of Engineering in Medicine 232 (12) (2018) 1196–1208, pMID: 30445886. doi:10.1177/0954411918810044.

[32] S. Ilincic, N. Tungkunagorn, A. Vernes, G. Vorlaufer, P. A. Fotiu, F. Franek, Finite and boundary element method contact mechanics on rough, artificial hip joints, Proceedings of the Institution of Mechanical Engineers, Part J: Journal of Engineering Tribology 225 (11) (2011) 1081–1091. doi:10.1177/1350650111406776.

[33] S. Ilincic, A. Vernes, G. Vorlaufer, H. Hunger, N. Dörr, F. Franek, Numerical estimation of wear in reciprocating tribological experiments, Proceedings of the Institution of Mechanical Engineers, Part J: Journal of Engineering Tribology 227 (5) (2013) 510–519. doi:10.1177/1350650113476606.

[34] A. Persson, On the Stress Distribution of cylindrical elastic bodies in contact, Doktorsavhandlingar vid Chalmers tekniska Högskola, Fototryck, 1964.

[35] M. Ciavarella, P. Decuzzi, The state of stress induced by the plane frictionless cylindrical contact. i. the case of elastic similarity, International Journal of Solids and Structures 38 (2001) 4507–4523. doi:10.1016/S0020-7683(00)00289-4.

[36] M. Ciavarella, P. Decuzzi, The state of stress induced by the plane frictionless cylindrical contact. ii. the general case (elastic dissimilarity), International Journal of Solids and Structures 38 (26) (2001) 4525–4533. doi:https://doi.org/10.1016/S0020-7683(00)00290-0.

[37] M. Ciavarella, A. Baldini, J. Barber, A. Strozzi, Reduced dependence on loading parameters in almost conforming contacts, International Journal of Mechanical Sciences 48 (9) (2006) 917–925. doi:https://doi.org/10.1016/j.ijmecsci.2006.03.016.

[38] J. Blanco-Lorenzo, J. Santamaria, E. G. Vadillo, N. Correa, A contact mechanics study of 3d frictional conformal contact, Tribology International 119 (2018) 143–156. doi:https://doi.org/10.1016/j.triboint.2017.10.022.

[39] S. Liu, W. Wayne Chen, Two-dimensional numerical analyses of double conforming contacts with effect of curvature, International Journal of Solids and Structures 49 (11) (2012) 1365–1374. doi:https://doi.org/10.1016/j.ijsolstr.2012.02.019.

[40] S. Liu, Numerical simulation of double conformal contacts involving both interference and clearance, Tribology Transactions 56 (5) (2013) 867–878. doi:10.1080/10402004.2013.806686.

[41] S. Ilincic, G. Vorlaufer, P. A. Fotiu, A. Vernes, F. Franek, Combined finite element-boundary element method modelling of elastic multi-asperity contacts, Proceedings of the Institution of Mechanical Engineers, Part J: Journal of Engineering Tribology 223 (5) (2009) 767–776. doi:10.1243/13506501JET542.

[42] A. C. Stevenson, Complex potentials in two-dimensional elasticity, Proceedings of the Royal Society of London. Series A. Mathematical and Physical Sciences 184 (997) (1945) 129–179. doi:https://doi.org/10.1098/rspa.1945.0015.

[43] N. I. Muskhelishvili, et al., Some basic problems of the mathematical theory of elasticity, Vol. 15, Noordhoff Groningen, 1953.

[44] S. Yousef, 16 - polymer nanocomposite components: A case study on gears, in: J. Njuguna (Ed.), Lightweight Composite Structures in Transport, Woodhead Publishing, 2016, pp. 385–420. doi:https://doi.org/10.1016/B978-1-78242-325-6.00016-5.

[45] H. Koike, K. Kida, E. Santos, J. Rozwadowska, Y. Kashima, K. Kanemasu, Self-lubrication of peek polymer bearings in rolling contact fatigue under radial loads, Tribology International 49 (2012) 30–38. doi:https://doi.org/10.1016/j.triboint.2011.12.005.

[46] F. Farroni, M. Russo, R. Russo, F. Timpone, A physical-analytical model for a real-time local grip estimation of tyre rubber in sliding contact with road asperities, Proceedings of the Institution of Mechanical Engineers, Part D: Journal of Automobile Engineering 228 (8) (2014) 955–969. doi:10.1177/0954407014521402.

[47] K. Friedrich, Polymer composites for tribological applications, Advanced Industrial and Engineering Polymer Research 1 (1) (2018) 3–39. doi:https://doi.org/10.1016/j.aiepr.2018.05.001.

[48] R. Fusaro, Self-lubricating polymer composites and polymer transfer film lubrication for space applications, Tribology International 23 (2) (1990) 105–122, special Issue: Space Tribology. doi:https://doi.org/10.1016/0301-679X(90)90043-O.

[49] D. E. Brewe, H. W. Scibbe, W. J. Anderson, Film-transfer studies of seven ball-bearing retainer materials in 60 R (33 K) hydrogen gas at 0.8 million DN value, Vol. 3730, National Aeronautics and Space Administration [for sale by the Clearinghouse . . . , 1966.

[50] R. M. Christensen, P. M. Naghdi, Linear non-isothermal viscoelastic solids, Acta Mechanica 3 (1) (1967) 1–12.

[51] R. Christensen, Theory of viscoelasticity: an introduction, Elsevier, 2012.

[52] S. Timoshenko, J. Goodier, Theory of Elasticity, 2nd Edition, McGraw-Hill Book Company, 1951.

[53] L. D. Landau, E. M. Lifshitz, A. M. Kosevich, L. P. Pitaevskii, Theory of elasticity: volume 7, Vol. 7, Elsevier, 1986.

[54] F. Riesz, B. Nagy, Functional Analysis, Dover Books on Mathematics, Dover Publications, 2012.

[55] R. Lakes, Viscoelastic Materials, Cambridge University Press, 2009. doi:10.1017/CBO9780511626722.

[56] V. Volterra, E. T. Whittaker, Theory of functionals and of integral and integro-differential equations, Dover publications, 1959.

[57] B. D. Coleman, V. J. Mizel, A general theory of dissipation in materials with memory, Archive for Rational Mechanics and Analysis 27 (1967) 255–274.

[58] B. D. Coleman, Thermodynamics of materials with memory, Tech. rep., MELLON INST PITTSBURGH PA (1964).

[59] M. E. Gurtin, I. Herrera, On dissipation inequalities and linear viscoelasticity, Quarterly of applied mathematics 23 (3) (1965) 235–245.

[60] J. Heijboer, Secondary loss peaks in glassy amorphous polymers, International Journal of Polymeric Materials and Polymeric Biomaterials 6 (1-2) (1977) 11–37. doi:10.1080/00914037708075218.

[61] A. J. Kovacs, La contraction isotherme du volume des polymères amorphes, Journal of polymer science 30 (121) (1958) 131–147.

[62] L. H. Sperling, Sound and vibration damping with polymers: Basic viscoelastic definitions and concepts, ACS Publications, 1990.

[63] H. Leaderman, Elastic and creep properties of filamentous materials, Ph.D. thesis, MassaChusetts Institute of Technology (1941).

[64] J. D. Ferry, Mechanical properties of substances of high molecular weight. vi. dispersion in concentrated polymer solutions and its dependence on temperature and concentration, Journal of the American Chemical Society 72 (8) (1950) 3746–3752.

[65] F. Schwarzl, A. Staverman, Time-temperature dependence of linear viscoelastic behavior, Journal of Applied Physics 23 (8) (1952) 838–843.

[66] J. Barber, Elasticity, Online access with purchase: Springer, Springer Netherlands, 2002.

[67] B. J. Hamrock, B. Jacobson, S. R. Schmid, Fundamentals of Fluid Film Lubrication, Taylor & Francis Inc, 2004.

[68] E. Lee, Stress analysis in visco-elastic bodies, Quarterly of applied mathematics 13 (2) (1955) 183–190.

[69] C. Putignano, Oscillating viscoelastic periodic contacts: A numerical approach, International Journal of Mechanical Sciences 208 (2021) 106663. doi:https://doi.org/10.1016/j.ijmecsci.2021.106663.

[70] W. W. Chen, Q. J. Wang, Z. Huan, X. Luo, Semi-analytical viscoelastic contact modeling of polymer-based materials, Journal of Tribology 133 (4) (oct 2011). doi:10.1115/1.4004928.

[71] R. Bentall, K. Johnson, An elastic strip in plane rolling contact, International Journal of Mechanical Sciences 10 (8) (1968) 637–663.

[72] N. Menga, G. Carbone, D. Dini, Exploring the effect of geometric coupling on friction and energy dissipation in rough contacts of elastic and viscoelastic coatings, Journal of the Mechanics and Physics of Solids 148 (2021) 104273.

[73] G. Carbone, L. Mangialardi, Adhesion and friction of an elastic half-space in contact with a slightly wavy rigid surface, Journal of the Mechanics and Physics of Solids 52 (6) (2004) 1267–1287. doi:https://doi.org/10.1016/j.jmps.2003.12.001.

[74] G. Carbone, L. Mangialardi, Analysis of the adhesive contact of confined layers by using a green's function approach, Journal of the Mechanics and Physics of Solids 56 (2) (2008) 684–706. doi:https://doi.org/10.1016/j.jmps.2007.05.009.

[75] G. Carbone, M. Scaraggi, U. Tartaglino, Adhesive contact of rough surfaces: Comparison between numerical calculations and analytical theories, The European Physical Journal E 30 (1) (sep 2009). doi:https://doi.org/10.1140/epje/i2009-10508-5.

[76] C. Putignano, L. Afferrante, G. Carbone, G. Demelio, A new efficient numerical method for contact mechanics of rough surfaces, International Journal of Solids and Structures 49 (2) (2012) 338–343. doi:https://doi.org/10.1016/j.ijsolstr.2011.10.009.

[77] R. Stribeck, et al., Ball bearings for various loads, Trans. ASME 29 (4) (1907) 420–463.

[78] T. A. Harris, Rolling bearing analysis (2007).

[79] H. Sjovall, The load distribution within ball and roller bearings under given external radial and axial load, Tekniks Tidskrift Mek. (9) (1933).

[80] T. Lazović, M. Ristivojević, R. Mitrović, Mathematical model of load distribution in rolling bearing, FMe Transactions 36 (4) (2008) 189–196.

[81] R. Tomović, Calculation of the boundary values of rolling bearing deflection in relation to the number of active rolling elements, Mechanism and Machine Theory 47 (2012) 74–88. doi:https://doi.org/10.1016/j.mechmachtheory.2011.08.006.

[82] R. Tomović, Calculation of the necessary level of external radial load for inner ring support on q rolling elements in a radial bearing with internal radial clearance, International Journal of Mechanical Sciences 60 (1) (2012) 23–33. doi:https://doi.org/10.1016/j.ijmecsci.2012.04.002.

[83] C. Putignano, L. Afferrante, G. Carbone, G. Demelio, A new efficient numerical method for contact mechanics of rough surfaces, International Journal of Solids and Structures 49 (2) (2012) 338 – 343. doi:https://doi.org/10.1016/j.ijsolstr.2011.10.009.

[84] C. Putignano, G. Carbone, A review of boundary elements methodologies for elastic and viscoelastic rough contact mechanics, Physical Mesomechanics 17 (2014) 321–333.

[85] S. Eder, D. Bianchi, I. Neacşu, G. Vorlaufer, An experimental and signal analysis workflow for detecting cold-induced noise emissions (cold squealing) from porous journal bearings, Mechanical Systems and Signal Processing 115 (2019) 60–69. doi:https://doi.org/10.1016/j.ymssp.2018.05.047.

[86] I. A. Neacşu, B. Scheichl, G. Vorlaufer, S. J. Eder, F. Franek, L. Ramonat, Experimental Validation of the Simulated Steady-State Behavior of Porous Journal Bearings1, Journal of Tribology 138 (3), 031703 (04 2016). doi:10.1115/1.4032659.

[87] L. Heepe, S. N. Gorb, Biologically inspired mushroom-shaped adhesive microstructures, Annual Review of Materials Research 44 (2014) 173–203.

[88] W. B. Dapp, A. Lücke, B. N. J. Persson, M. H. Müser, Self-affine elastic contacts: Percolation and leakage, Phys. Rev. Lett. 108 (2012) 244301. doi:10.1103/PhysRevLett.108.244301.

[89] S.-C. Vlădescu, C. Putignano, N. Marx, T. Keppens, T. Reddyhoff, D. Dini, The percolation of liquid through a compliant seal—an experimental and theoretical study, Journal of Fluids Engineering 141 (3) (2019).

[90] A. Shukla, T. Datta, Optimal use of viscoelastic dampers in building frames for seismic force, Journal of Structural Engineering 125 (4) (1999) 401–409.

[91] G. Carbone, B. Lorenz, B. N. J. Persson, A. Wohlers, Contact mechanics and rubber friction for randomly rough surfaces with anisotropic statistical properties, The European Physical Journal E 29 (3) (2009) 275–284. doi:https://doi.org/10.1140/epje/i2009-10484-8.

[92] C. Putignano, A. Campanale, Squeeze lubrication between soft solids: A numerical study, Tribology International 176 (2022) 107824. doi:https://doi.org/10.1016/j.triboint.2022.107824.

[93] A. Pandey, S. Karpitschka, C. H. Venner, J. H. Snoeijer, Lubrication of soft viscoelastic solids, Journal of fluid mechanics 799 (2016) 433–447.

[94] C. H. Venner, A. A. Lubrecht, Multi-level methods in lubrication, Elsevier, 2000.

[95] S. Rohde, D. Whicker, J. Booker, Elastohydrodynamic squeeze films: effects of viscoelasticity and fluctuating load (1979).

[96] A. A. Elsharkawy, Visco-elastohydrodynamic lubrication of line contacts, Wear 199 (1) (1996) 45–53. doi:https://doi.org/10.1016/0043-1648(96)07212-2.

[97] C. Hooke, Elastohydrodynamic lubrication of soft solids, in: D. Dowson, C. Taylor, T. Childs, G. Dalmaz, Y. Berthier, L. Flamand, J.-M. Georges, A. Lubrecht (Eds.), Elastohydrodynamics - '96 Fundamentals and Applications in Lubrication and Traction, Vol. 32 of Tribology Series, Elsevier, 1997, pp. 185–197. doi:https://doi.org/10.1016/S0167-8922(08)70448-6.

[98] C. Putignano, D. Dini, Soft matter lubrication: does solid viscoelasticity matter?, ACS applied materials & interfaces 9 (48) (2017) 42287–42295.

[99] C. Putignano, Soft lubrication: A generalized numerical methodology, Journal of the Mechanics and Physics of Solids 134 (2020) 103748.

[100] C. Putignano, A. Campanale, Squeeze lubrication between soft solids: A numerical study, Tribology International 176 (2022) 107824. doi:https://doi.org/10.1016/j.triboint.2022.107824.

[101] S. Stupkiewicz, J. Lengiewicz, P. Sadowski, S. Kucharski, Finite deformation effects in soft elastohydrodynamic lubrication problems, Tribology International 93 (2016) 511–522, 41st Leeds-Lyon Symposium on Tribology - Integrated Tribology. doi:https://doi.org/10.1016/j.triboint.2015.03.016.

[102] O. Reynolds, Iv. on the theory of lubrication and its application to mr. beauchamp tower's experiments, including an experimental determination of the viscosity of olive oil, Philosophical transactions of the Royal Society of London (177) (1886) 157–234.

[103] D. A. Crolla, Automotive engineering, 2009.

[104] H. Rahnejat, Tribology and dynamics of engine and powertrain: fundamentals, applications and future trends, Elsevier, 2010.

[105] A. Chasalevris, F. Dohnal, Improving stability and operation of turbine rotors using adjustable journal bearings, Tribology International 104 (2016) 369–382.

[106] A. Linjamaa, A. Lehtovaara, R. Larsson, M. Kallio, S. Söchting, Modelling and analysis of elastic and thermal deformations of a hybrid journal bearing, Tribology International 118 (2018) 451–457.

[107] S. Eder, C. Ielchici, S. Krenn, D. Brandtner, An experimental framework for determining wear in porous journal bearings operated in the mixed lubrication regime, Tribology International 123 (2018) 1–9. doi:https://doi.org/10.1016/j.triboint.2018.02.026.

[108] G. Boidi, S. Krenn, S. J. Eder, Identification of a material–lubricant pairing and operating conditions that lead to the failure of porous journal bearing systems, Tribology Letters 68 (2020) 1–14.

[109] C. D. Ielchici, S. Krenn, S. J. Eder, A tribometer and methodology for wear and friction testing of porous journal bearings at elevated temperatures, Industrial Lubrication and Tribology 72 (8) (2020) 1027–1031.

[110] T. E. Carl, An experimental investigation of a cylindrical journal bearing under constant and sinusoidal loading, Proc. Inst. Mech. Engrs. 178 (3) (1964) 100–119.

[111] G. Higginson, Paper 1: The theoretical effects of elastic deformation of the bearing liner on journal bearing performance, in: Proceedings of the Institution of Mechanical Engineers, Conference Proceedings, Vol. 180, SAGE Publications Sage UK: London, England, 1965, pp. 31–38.

[112] J. O'Donoghue, D. Brighton, C. Hooke, The effect of elastic distortions on journal bearing performance (1967).

[113] M. K. Benjamin, V. Castelli, A theoretical investigation of compliant surface journal bearings (1971).

[114] C. Hooke, J. O'donoghue, Elastohydrodynamic lubrication of soft, highly deformed contacts, Journal of Mechanical Engineering Science 14 (1) (1972) 34–48.

[115] K. Oh, K. Huebner, Solution of the elastohydrodynamic finite journal bearing problem (1973).

[116] H. Conway, H. Lee, The analysis of the lubrication of a flexible journal bearing (1975).

[117] W. Mak, H. Conway, The lubrication of a long, porous, flexible journal bearing (1977).

[118] H. Conway, H. Lee, The lubrication of short, flexible journal bearings (1977).

[119] F. J. Profito, D. C. Zachariadis, Partitioned fluid-structure methods applied to the solution of elastohydrodynamic conformal contacts, Tribology International 81 (2015) 321–332.

[120] R. L. Orndorff Jr, Water-lubricated rubber bearings, history and new developments, Naval engineers journal 97 (7) (1985) 39–52.

[121] D. Cabrera, N. Woolley, D. Allanson, Y. Tridimas, Film pressure distribution in water-lubricated rubber journal bearings, Proceedings of the Institution of Mechanical Engineers, Part J: Journal of Engineering Tribology 219 (2) (2005) 125–132.

[122] G. Liu, M. Li, Experimental study on the lubrication characteristics of water-lubricated rubber bearings at high rotating speeds, Tribology International 157 (2021) 106868.

[123] A. Vakis, V. Yastrebov, J. Scheibert, L. Nicola, D. Dini, C. Minfray, A. Almqvist, M. Paggi, S. Lee, G. Limbert, J. Molinari, G. Anciaux, R. Aghababaei, S. Echeverri Restrepo, A. Papangelo, A. Cammarata, P. Nicolini, C. Putignano, G. Carbone, S. Stupkiewicz, J. Lengiewicz, G. Costagliola, F. Bosia, R. Guarino, N. Pugno, M. Müser, M. Ciavarella, Modeling and simulation in tribology across scales: An overview, Tribology International 125 (2018) 169–199. doi:https://doi.org/10.1016/j.triboint.2018.02.005.

[124] A. Almqvist, F. P. Ràfols, Scientific computing with applications in tribology: A course compendium (2022).

[125] B. M. Irons, R. C. Tuck, A version of the aitken accelerator for computer iteration, International Journal for Numerical Methods in Engineering 1 (3) (1969) 275–277.

[126] K. L. Johnson, K. L. Johnson, Contact mechanics, Cambridge university press, 1987.

[127] A. E. H. Love, A treatise on the mathematical theory of elasticity, University press, 1927.

[128] M. Rothman, ISOLATED FORCE PROBLEMS IN TWO-DIMENSIONAL ELASTICITY (I)†, The Quarterly Journal of Mechanics and Applied Mathematics 3 (3) (1950) 279–296. doi:10.1093/qjmam/3.3.279.

[129] M. Rothman, ISOLATED FORCE PROBLEMS IN TWO-DIMENSIONAL ELASTICITY (II), The Quarterly Journal of Mechanics and Applied Mathematics 3 (4) (1950) 469–480. doi:https://doi.org/10.1093/qjmam/3.4.469.

[130] G. Hondros, The evaluation of poisson's ratio and the modulus of materials of a low tensile resistance by the brazilian (indirect tensile) test with particular reference to concrete, Aust. J. Appl. Sci. 10 (1959) 243–264.

[131] S. Lekhnitskii, Radial distribution of stresses in a wedge and in a half-plane with variable modulus of elasticity, Journal of Applied Mathematics and Mechanics 26 (1) (1962) 199–206. doi:https://doi.org/10.1016/0021-8928(62)90112-0.

[132] M. Batista, J. Usenik, Stresses in a circular ring under two forces acting along a diameter, The Journal of Strain Analysis for Engineering Design 31 (1) (1996) 75–78. doi:10.1243/03093247V311075.

[133] M. Serati, H. Alehossein, D. J. Williams, Elastic stress analysis of partially loaded hollow discs, International Journal of Engineering Science 53 (2012) 19–37. doi:https://doi.org/10.1016/j.ijengsci.2011.12.010.

Publications

- M. Santeramo, C. Putignano, G. Vorlaufer, S. Krenn, G. Carbone, *Viscoelastic steady-state rolling contacts: A generalized boundary element formulation for conformal and non-conformal geometries*, Journal of the Mechanics and Physics of Solids 171 (2023) 105129
- M. Santeramo, C. Putignano, G. Vorlaufer, S. Krenn, G. Carbone,*On the role of viscoelasticity in polymer rolling element bearings: Load distribution and hysteretic losses*, Mechanism and Machine Theory 189 (2023) 105421.
- M. Santeramo, G. Carbone , G. Vorlaufer, S. Krenn, C. Putignano, *Viscohydrodynamic lubrication in conformal contacts: A numerical approach.*, Submitted

Acknowledgments

This work was funded by the Austrian COMET program (Project InTribology, No. 872176) via the Austrian Research Promotion Agency (FFG) and the Provinces of Niederösterreich and Vorarlberg and has been carried out in collaboration with the Austrian Excellence Centre of Tribology (AC2T research GmbH).

I want to express my sincere gratitude to my supervisors Prof. Giuseppe Carbone, Prof. Carmine Putignano, and Prof. Leonardo Soria for their continuous support in my Ph.D. research, their motivation, and encouragement.

Special thanks to the AC2T group, in particular to Stefan Krenn, Georg Vorlaufer, Shreyas Jalikop, Martin Jech, André Rudnytskyj, Harald Voglmayr, Manuel Zellhofer, and Ulrich Stoiber, for hosting me and the inspiring conversations.

Finally, I would like to thank the Open Spaces for the enthusiasm, the strong friendship, and the insightful talks, and, most importantly, Maria and my family for being in for the long haul.